2015-12-01

Numerical Analysis of Passive Force on Skewed Bridge Abutments

Zifan Guo
Brigham Young University

Numerical Analysis of Passive Force on Skewed Bridge Abutments

Zifan Guo

A thesis submitted to the faculty of
Brigham Young University
in partial fulfillment of the requirements for the degree of

Master of Science

Kyle M. Rollins, Chair
Kevin W. Franke
Richard J. Balling

Department of Civil and Environmental Engineering

Brigham Young University

December 2015

ABSTRACT

Numerical Analysis of Passive Force on Skewed Bridge Abutments

Zifan Guo
Department of Civil and Environmental Engineering, BYU
Master of Science

Accounting for seismic forces and thermal expansion in bridge design requires an accurate passive force-deflection relationship for the abutment wall. Current design codes make no allowance for skew effects on passive force; however, large scale field tests indicate that there is a substantial reduction in peak passive force as skew angle increases. A reduction in passive force also reduces the transverse shear resistance on the abutment. The purpose of this study is to validate three-dimensional model using PLAXIS 3D, against large scale test results performed at Brigham Young University and to develop a set of calibrated finite element models. The model set could be used to evaluate the variation in passive resistance with skew angle for various abutment geometries and backfill types.

Initially, the finite element model was calibrated using the results from a suite of field tests where the backfill material consisted of dense compacted sand. Results were available for skew angles of 0, 15, 30 and 45°. Numerical model results were compared with measured passive force-deflection curves, ground surface heave and displacement contours, longitudinal displacements, and failure plane geometry. Soil properties were defined by laboratory testing and in-situ direct shear tests on the compacted fill. Soil properties and mesh geometries were primarily calibrated based on the zero skew test results.

The results were particularly sensitive to the soil friction angle, wall friction angle, angle of dilatancy, soil stiffness and lateral restraint of the abutment backwall movement.

Reasonable agreement between measured and computed response was obtained in all cases confirming numerically that passive force decreases as skew angle increases Additional analyses were then performed for abutments with different soil boundaries.

Keywords: finite element analysis, passive force, bridge abutment, skew, pile caps, lateral resistance, PYCAP, earthquake, seismic

ACKNOWLEDGEMENTS

I would like to express my sincere appreciation to Dr. Kyle M. Rollins, my graduate advisor, for allowing me to be involved in this research and offering guidance, support and encouragement throughout the research. It was an honor to learn from and work with him. I also want to express my appreciation to other members of my committee, Dr. Kevin W. Franke and Dr. Richard J. Balling for all their time and support. Thank you Dr. Kevin W. Franke for your patience and clear direction. Thank you Dr. Richard J. Balling for bringing me to the world of finite element analysis.

I treasure the experience in the Salt Lake City airport with Kyle Smith, Amy Fredrickson, Cole Washburn, Quinton Taylor, John Cazier, Sam Mineer, Ian Oxborrow, Dave Anderson, Rodney Mayo, and other field technicians.

. Most importantly, I want to say thank you to my mom, Xin Li, grandmother, Jingquan Li and friends Xiaoou Chen and Jun Song. Thank you for putting your trust in me. With your love and support, I was able to continue my education.

Finally, funding for this study was provided by FHWA pooled fund study TPF-5(264), supported by Departments of Transportation from the states of California, Minnesota, Montana, New York, Oregon and Utah. Utah served as the lead agency. David Stevens worked as the project manager. This support is widely acknowledged; however, the opinions and recommendations in this paper do not necessarily represent those of the sponsoring organizations. I also express appreciation to the Salt Lake City Airport Department providing the test site in this study.

TABLE OF CONTENTS

LIST OF TABLES

LIST OF FIGURES

1 INTRODUCTION

1.1 Background

Pile foundations and abutment structures are widely used as load transferring system in bridge abutment design. In the past, researches have been performed to investigate passive force versus deflection relationships for non-skewed bridge abutments, and backfill with dense compacted material (Mokwa and Duncan 2001; Rollins and Sparks 2002; Rollins and Cole 2006; Rollins et al. 2010; Rollins and Marsh 2013). These investigations indicate that passive forces can be effectively predicted by the log-spiral method and is mobilized at a displacement of approximately three to five percent of the abutment backwall height (Lemnitzer et al. 2009; Rollins and Cole 2006). Methods approximating the complete passive force-deflection curve with a hyperbola have been developed by Shamsabadi et al. (2007) and Mokwa and Duncan (2001). However, to simplify the procedure, design specifications typically recommand a longitudinal deflection versus passive force relationship with a bi-linear pattern. (Caltrans 2010; AASHTO 2001).

In Current bridge design practice, peak passive force is calculated using the same methods for non-skewed and skewed bridges (AASHTO 2011). However, field performance observations evidently indicated that, when subjected to seismic forces (Shamsabadi et al. 2006; Elnashai et

al.2010), or thermal expansion (Steinberg and Sargand 2010), skewed bridges performed worse than non-skewed bridges.

Until recently, no large scale experiments had been conducted for skewed bridge structures. Small-scale by Rollins and Jessee 2013, and finite element models (Shamsabadi et al. 2006) found that there is a significant reduction in passive force in skewed bridge abutment structures. To account for this effect, Rollins and Jessee 2013 proposed the correction factor, R_{skew}, given by Equation (1-1).

$$R_{skew} = \frac{P_{P-skew}}{P_{P-no\ skew}} = 8.0 * 10^{-5}\theta - 0.018\theta + 1.0 \qquad (1\text{-}1)$$

Where

θ= Skew angle

$P_{P\text{-}skew}$= Peak passive force for a skewed abutment

$P_{P\text{-}no\ skew}$= Peak passive force for a non-skewed abutment

Although field testing is necessary and critical in the development of design equations, it is not economically feasible to test every conceivable backfill type and geometry. However, calibrated finite element models can be used to investigate these effects for far less time and effort. A team of students were involved in the large scale field test near the Salt Lake City airport. The primary focus of this research is finite element analysis using Plaxis 3D.

1.2 Research Objectives

The objectives of this research are:

1. Quantitatively show reduction in peak passive force in numerical models.
2. Evaluate changes in the passive force-deflection curve for different skew angle sets.

3. Identify the governing failure mechanism associated with different skew angles by comparing field tests to numerical models.
4. Calibrate geometric settings and material parameters to obtain a generic set of numerical models, for future research investigations.

1.3 Order of Presentation

This thesis contains six chapters. The second chapter provides a review of existing literature which will be applied as research tools. The third chapter describes the test layout, procedures and results from the physical testing. The fourth chapter elaborately introduces the procedure of using Plaxis 3D. The fifth chapter discusses numerical results and parametric studies. Chapter six summarizes conclusions and recommendations.

2 LITERATURE REVIEW

In the past, finite element methods have been used successfully to model passive force-deflection behavior for non-skewed bridge abutments. However, very few studies utilizing three-dimensional finite element models analyzed the effect that skew angle has on the relationship between passive force and backwall deflection.

This chapter will first describe the analytical methods pertaining to the passive force versus deflection relationships and the effect of skew angle on performance from physical testing. Numerical methods will be presented thereafter.

The numerical modeling section will consider the results obtained by some of the two-dimensional finite element studies that analyzed the passive force-deflection behavior for non-skewed bridges. Following this discussion, the various soil constitutive models that were used for this thesis will be described, along with each model's strengths and weaknesses.

2.1 Passive Earth Pressure Theories

Several earth pressure theories have been developed in the past. This section will discuss the Coulomb (1776), Rankine (1857), and Log-Spiral theories (Terzaghi 1943). Those three widely used theories have been developed to estimate the ultimate lateral strength of soil. All three theories can be reduced to the general form shown in Equation (2-1).

$$\sigma'_p = \frac{1}{2} K_P \gamma H^2 + 2\sqrt{K_P} c' H \quad (2\text{-}1)$$

where

σ'_p = Ultimate passive force per unit width

$K_P = \frac{\sigma`_p}{\sigma`_0}$ = passive earth pressure coefficient

γ = moist unit weight of the soil

H = backfill height

c' = soil cohesion

The method of finding K_P depends on which theory is employed.

2.1.1 Coulomb (1776)

Coulomb theory was developed in 1776 as an analytical method of estimating passive earth pressure. As shown in Figure 2-1, it mathematically defined the friction angle of the soil(ϕ), the friction angle at interface between the wall and the soil (δ), the backfill inclination(β).

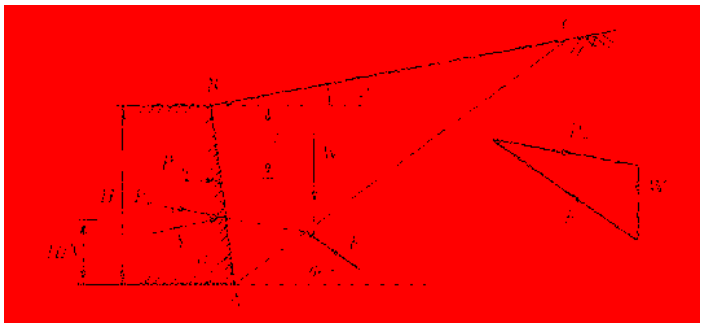

Figure 2-1: Coulomb Failure Surface

The passive earth coefficient, K_P, for the Coulomb theory is defined by the following equation:

$$K_p = \frac{(cos\phi)^2}{cos\delta\left[1-\sqrt{\frac{\sin(\phi+\delta)\sin(\phi+\beta_s)}{cos\delta cos\beta_s}}\right]^2} \quad (2\text{-}2)$$

Where

ϕ = the soil friction angle

δ = the wall friction angle or interface friction angle between soil and abutment

β = backfill inclination

From experiments and field observations, Equation (2-2) tends to over-predict the K_p value when $\delta/\phi > 0.4$, which typically happens in the field for most soil-structure interfaces, as shown in Table 2-1. Therefore, this method is likely to yield unrealistically high passive force values when real wall friction values are used.

Table 2-1: Typical Values for δmax/φ, Adapted from Potyondy (1961)

Soil type	δ_{max}/ϕ		
	Steel	*Concrete*	*Wood*
Sand	0.54	0.76	0.76
Silt and clay	0.54	0.5	0.55

2.1.2 Rankine (1857)

Rankine's mathematical theory assumes that the wall friction angle is zero (Rankine 1857). Rankine's coefficient, K_P, is given by the following Equation (2-2):

$$K_P = \frac{cos\beta + \sqrt{cos^2\beta - cos^2\phi}}{cos\beta - \sqrt{cos^2\beta - cos^2\phi}} \qquad (2\text{-}3)$$

where

ϕ = the soil friction angle

β = embankment inclinatio

Experience has shown that the Rankine method typically predicts passive force values which are only 25% to 33% of the measured values. (Rollins et al. 2005). While a conservative estimate of K_p may be appropriate for some cases a more accurate value is usually preferred.

2.1.3 Log Spiral Theory

The log spiral method was described by Terzaghi (1943) and Terzaghi et al. (1996). It is considered to be the most theoretically correct method to determine the passive earth pressure coefficient (K_p) when large wall friction angles are present (Mokwa and Duncan 2001; Rollins and Cole 2006). The shear plane is represented by a logarithmic spiral section, followed by the linear Rankine section which intersects the ground surface as shown in Figure 2-2.

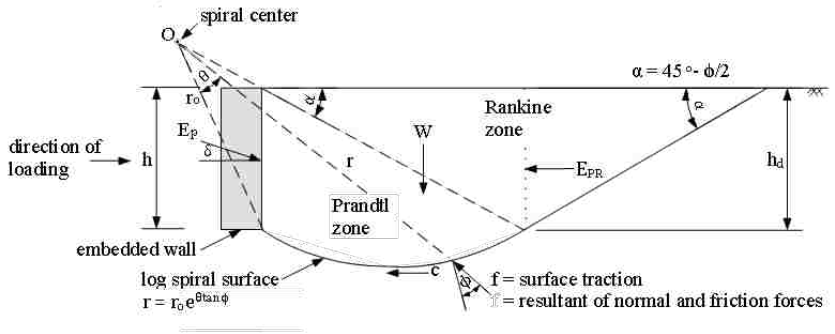

Figure 2-2: Log Spiral Failure Surface

When the δ/ ϕ (ratio between the wall friction angle, δ, and the soil friction angle, ϕ) is less than 0.4, the Log Spiral method gives values for K_p similar to those predicted by the Coulomb method. When δ/ ϕ is greater or equals to 0.4, the Log Spiral method is more appropriate for predicting passive forces on steel, concrete, and wooden walls (Mokwa and Duncan 2001).

Table 2-2 shows a comparison of K_p values predicted by the Coulomb, Rankine and Log Spiral theories for different δ/ ϕ values. When δ/ϕ is equal to 0, all methods yield the same K_p value; however, as δ/ϕ increases significant discrepancies become apparent.

Table 2-2: Kp Values as Calculated by Rankine, Coulomb, and Log Spiral Theories

	δ/ϕ=0	*δ/ϕ=0.2*	*δ/ϕ=0.4*	*δ/ϕ=0.9*
Rankine	4.60	N/A	N/A	N/A
Coulomb	4.60	6.35	9.36	30.36
Log Spiral	4.60	6.21	8.35	14.63

2.2 Passive Force – Displacement Relationship Studies

This section will discuss passive force-deflection relationships for pile caps and abutments as summarized by Mokwa and Duncan (2001).

2.2.1 Hyperbolic Passive Force-Displacements [Mokwa and Duncan (2001)]

Mokwa and Duncan (2001) provided an Excel program, referred to as PYCAP, to compute the passive force-deflection relationship. The program was based on the hyperbolic stress-strain relationship by Duncan and Chang (1970)to provide a hyperbolic passive force-deflection curve as shown in Figure 2-3.

The hyperbolic relationship is defined by Equation (2-4).

$$P = \frac{y}{\left[\frac{1}{K_{max}} + R_f \frac{y}{P_{ult}}\right]} \tag{2-4}$$

where,

y = given pile cap deflection

K_{max} initial slope of the load vs displacement curve

R_f = Failure ratio = 0.75 to 0.95

P_{ult} = Maximum passive soil resistance

P_{ult} is defined by the following Equation (2-5).

$$P_{ult} = E_P . R_{3D} . B \tag{2-5}$$

where,

E_p = Passive resistance per unit width from the log − spiral method
R_{3D} = Brinch Hansen 3D correction factor
B = embedded wall height

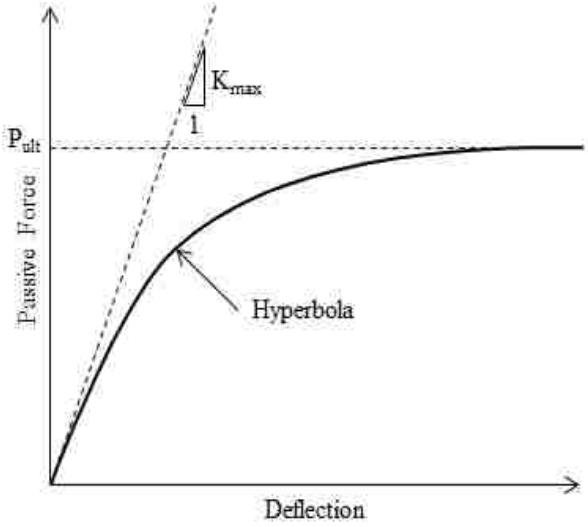

Figure 2-3: Mokwa and Duncan (2001) Hyperbolic Curve

The inputs in the program include the following: cap width (b), cap height (H), embedment depth (z), surcharge on ground surface (q_z), soil cohesion (c), soil friction angle (φ), wall friction angle (δ), initial soil modulus (E_i), Poisson's ratio (ν), in-situ unit weight (γ_m), adhesion factor (α, and the deflection-to-wall height ratio (Δ_{max}/H). Δ_{max} is defined as the displacement associated with failure.

The model generated passive force versus deflection curves that matched two passive pressure load tests, one with stiff sandy silt, the other with well-graded gravel (Mokwa and Duncan 2001). Rollins et al. (2005) and Shamsabadi et al. (2007) also found the hyperbolic method to produce the best agreement with measured response.

2.2.2 Rollins and Jessee (2013)

As briefly mentioned in the background section 1.1, Rollins and Jesse (2013) conducted several small-scale laboratory tests to find out the passive force versus pile cap displacement curves for 0°, 15°, 30°, and 45° skew sets.

As shown in Figure 2-4, a 4 feet wide by 2 feet high concrete wall was pushed longitudinally into a densely compacted sand backfill. The backfill extended 10 to 13 feet behind the backwall and 1 foot below the bottom of the wall to allow the formation of log-spiral failure planes.

Figure 2-5 shows the passive force versus pile cap deflection for 0°, 15°, 30°, and 45° skew sets in this lab test. The curves show that a significant reduction of peak passive force occurred with respect to increasing skew angle. And also, peak passive force was obtained at pile cap longitudinal deflections with values from 2% to 3% of the backwall height.

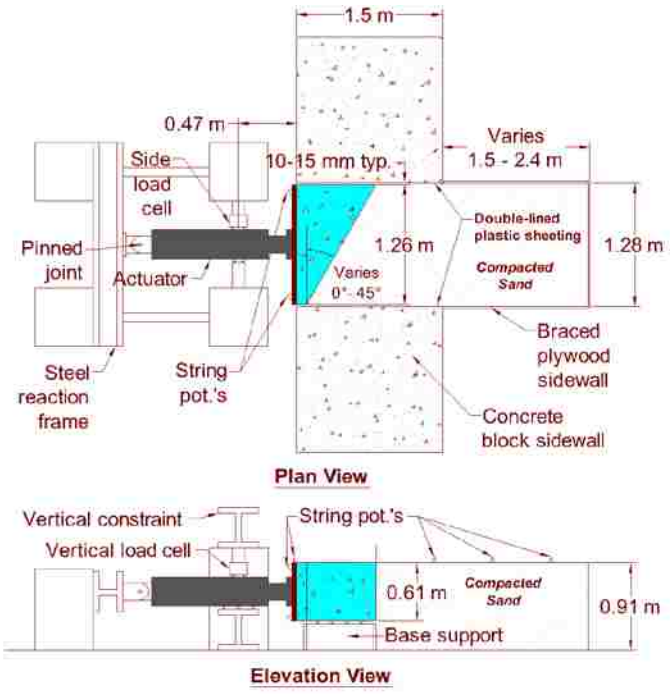

Figure 2-4: Small-scale Lab Test Configuration (Rollins and Jesse 2013).

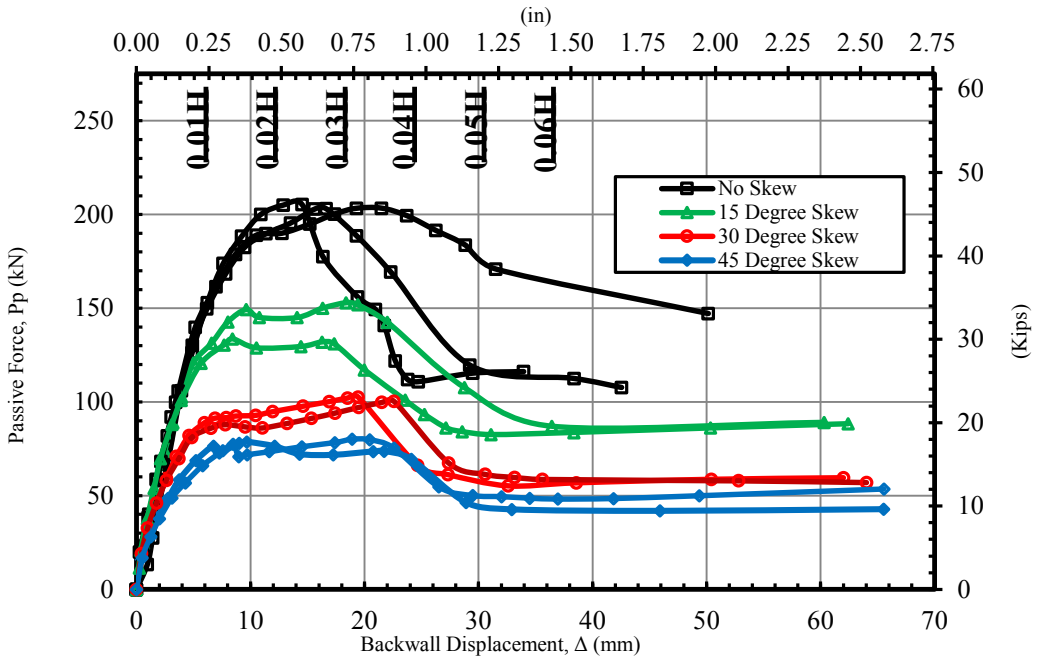

Figure 2-5: Reduction in Passive Resistance with Increasing Skew Angle (Rollins and Jessee 2013).

As mentioned in the background section, using results from the small scale tests mentioned above, Rollins and Jessee (2013) proposed a reduction factor R_{skew}, given by Equation (2-6) as a function of skew angle, θ.

$$R_{skew} = \frac{P_{p-skew}}{P_{P-no\ skew}} = 8.0 * 10^{-5}\theta^2 - 0.018\theta + 1.0 \qquad (2\text{-}6)$$

Where

θ= Skew angle

$P_{P\text{-}skew}$= Peak passive force for a skewed abutment

$P_{P\text{-}no\ skew}$= Peak passive force for a non-skewed abutment

Figure 2-6 shows a plot of reduction factor versus skew angles. Finite element results from Shamsabadi et al. (2006) followed the reduction curve within a remarkably small range of difference.

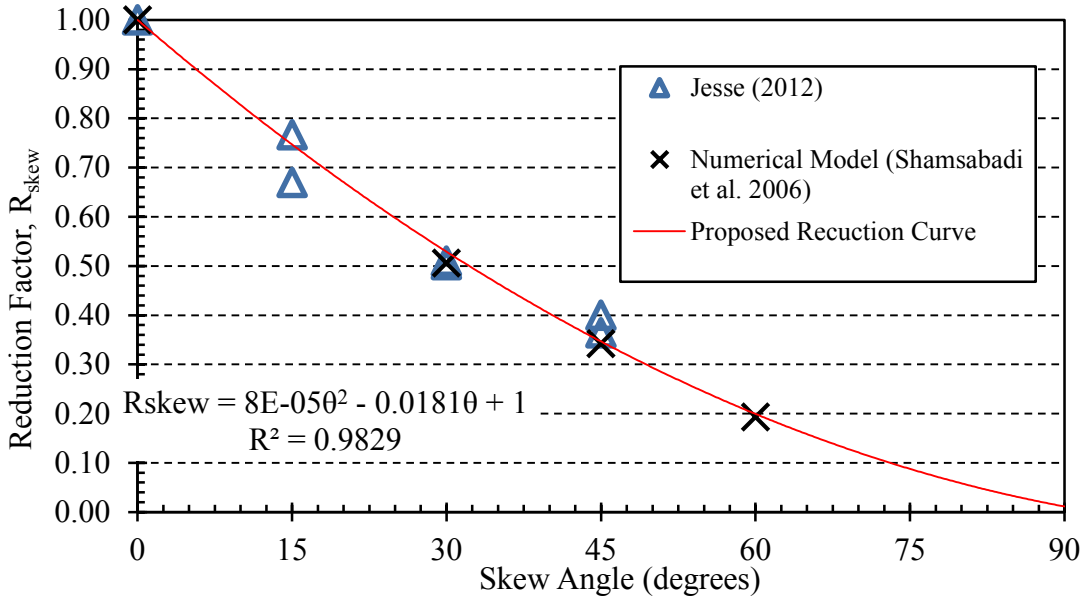

Figure 2-6: Proposed Reduction Curve by Rollins and Jesse (2013).

2.3 Finite Element Studies for Skewed and Non-Skewed Bridge Abutments

Wilson and Elgamal (2010) and Rollins and Nasr (2010) conducted two-dimensional finite element studies with the intent of determining the passive force versus backwall deflection relationship for non-skewed bridge abutments. For both of these studies the authors compared physical test results with the numerical results. In addition, Shamsabadi et al. (2006) has generated a three dimensional model using Plaxis 3D Tunnel which was used to predict the effect of skew angle on passive force-displacement curves. The results from these studies are summarized below.

2.3.1 Calibration of Numerical Model with Field Test Results

Wilson and Elgamal (2010) performed two large-scale lateral load tests with plane-strain boundary conditions. However, as only one test was modeled using the finite element software and only that test will be described in this section.

Backfill materials consisted of fill designed to meet Caltrans (2006) structural backfill requirements and consisted of sand with approximately 7% non-plastic silt, and less than 7% of fine angular gravel. The modified Proctor dry density was 20.26 kN/m^3 (129.0 lbf/ft^3) and the optimum moisture content was 8.5%. Direct shear tests indicated that the peak friction angle was 48° with a cohesion intercept of 14 kPa (292.4 lbf/ft^2). Triaxial tests found that the peak friction angle was 44° with the same cohesion intercept. The secant modulus at 50% of the peak stress (E_{50}) was estimated to be 16,400 kN/m^2, 18.700 kN/m^2, and 48,200 kN/m^2 (342,500 lbf/ft^2, 390,600 lbf/ft^2, and 1,006,700 lbf/ft^2) at confining pressures of 37 kPa, 72 kPa, and 144 kPa (773 psi, 1500 psi, and 3008 psi), respectively. Backfill materials were placed in 0.2 m (0.66 ft) thick lifts and compacted to an approximate dry density of 19.41 kN/m^3 (123.6 lbf/ft^3) at a moisture content of 8.7%.

The test setup was constructed so as to allow vertical movement of the abutment backwall; however, an actuator with a feedback loop was used to keep the vertical displacement close to zero. This configuration produced a fairly linear shear plane as would be expected with a low interface friction value and a Rankine approach. A peak passive force of 936 kN (210.4 kips) was obtained at 51 mm (2.0 in) of wall displacement, or 3.0% of the backwall height.

A Plaxis 2D finite element model was created so as to model the test conditions described above. Model input parameters are shown in Table 2-3 and model results are shown in Figure 2-4 (NOTE: SM and SC refer to additional model tests with silty sand and clayey sand that will not be discussed herein). As can be seen from the figure, model results and physical test results agreed quite well for loads up to 95% of the peak resistance.

Table 2-3: Finite Element Model Backfill Parameters [Adapted from Wilson and Elgamal 2010]

	FE Model Parameter	*Value*	*Basis for Selection*
ϕ	Effective angle of internal friction (degrees)	46	Triaxial and direct shear test data
c	Effective cohesion [kN/m^2 (lbf/ft^2)]	14 (292.4)	Triaxial and direct shear test data
ψ	Angle of dilatancy (degrees)	16	$\psi = \phi - 30$ (PLAXIS 2004)
p_{ref}	Reference stress (confinement) for stiffness [kN/m^2 (lbf/ft^2)]	100 (2,089)	Default value (PLAXIS 2004)
m	Power for stress-level dependency of stiffness	0.5	Plaxis 2004
E_{50}^{ref}	Secant stiffness in standard drained triaxial test [kN/m^2 (lbf/ft^2)]	40,000 (835,417)	Triaxial test data
E_{oed}^{ref}	Tangent stiffness for primary oedometer loading [kN/m^2 (lbf/ft^2)]	40,000 (835,417)	Default value (PLAXIS 2004)
K_0^{nc}	Coefficient of at-rest earth pressure	0.4	Default value (PLAXIS 2004)
γ	Total unit weight [kN/m^3 (lbf/ft^3)]	20.6 (131.1)	Measured
R_f	Failure ratio for hyperbolic relation	0.75	Within recommended range (Duncan and Mokwa 2001)

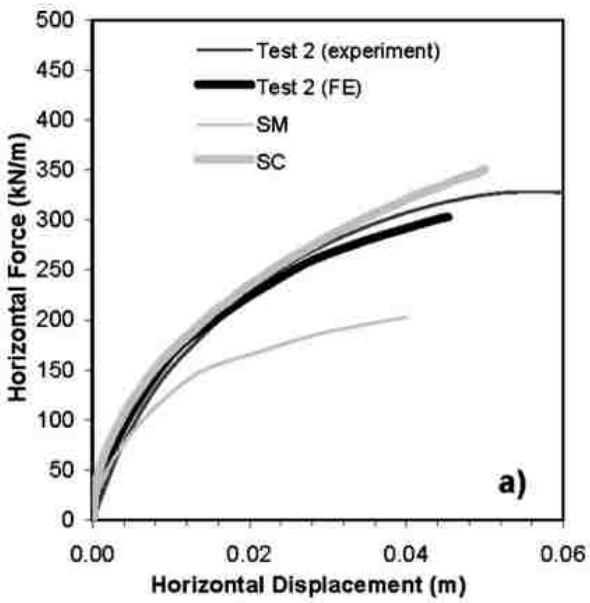

Figure 2-7: Load-Displacement Results from FE Passive Pressure Simulation (Wilson and Elgamal 2010)

2.3.2 Rollins and Nasr (2010)

Using Plaxis 2D Version-8 (2004), Rollins and Nasr (2010) created a 2D finite element model to simulate plane-strain passive force-deflection behavior of limited width dense gravel backfills. PYCAP (Mokwa and Duncan 2001) and ABUTMENT (Shamsabadi et al. 2007) were used to set up the initial model with approximated soil properties. Large-scale test data obtained by Rollins and Nasr (2010) and Gerber et al. (2010) was then compared to calibrate the computer model. The finite element model utilized the Hardening Soil constitutive model with model input parameters shown in Table 2-4.

Table 2-4: Input Parameters for Hardening Soil Model as Used by Rollins and Nasr (2010)

Parameter	*Loose Sand*	*Dense Gravel*	*Unit*
Friction Angle, ϕ	27.7	42.0	Degrees
Cohesion, c_{ref}	0.5 (10.44)	1.9 (39.68)	kPa (lb/ft^2)
Dilation Angle, ψ	0	12	Degrees
Soil Unit Weight	17.3 (110.1)	22.1 (140.7)	kN/m^3 (lb/ft^3)]
Secant Stiffness Modulus E_{50}^{ref}	15.8 (330)	81.4 (1,700)	MPa (kip/ft^2)]
Reference Stress, P_{ref}	100 (2089)	100 (2089)	kPa (lb/ft^2)
Poisson's Ratio, ν_{ur}	0.2	0.2	—
Interface Friction Angle, δ	0.75ϕ	0.75ϕ	Degrees
Interface Strength Reduction Factor, R_{inter}	0.7	0.7	—

Using the aforementioned parameters, agreement between the field tests, analytical results, and numerical models was within 10% at the peak passive force. In geotechnical area of study, result within 10% could be considered good.

Numerical results indicated that significant changes in passive resistance could be expected with respect to variations in the friction angle, cohesion, dilation angle, and the interface strength reduction factor.

The failure surfaces as shown in Figure 2-8 are consistent with a log spiral shear surface with the anticipated by Prandtl (log-spiral) zone and the wedge shaped Rankine zone.

In addition to the log spiral shaped failure surface, an inclined linear failure surface developed from the top of the wall downward to the log spiral surface. This linear surface appears to be the upper boundary between the Prandtl and Rankine shear zones.

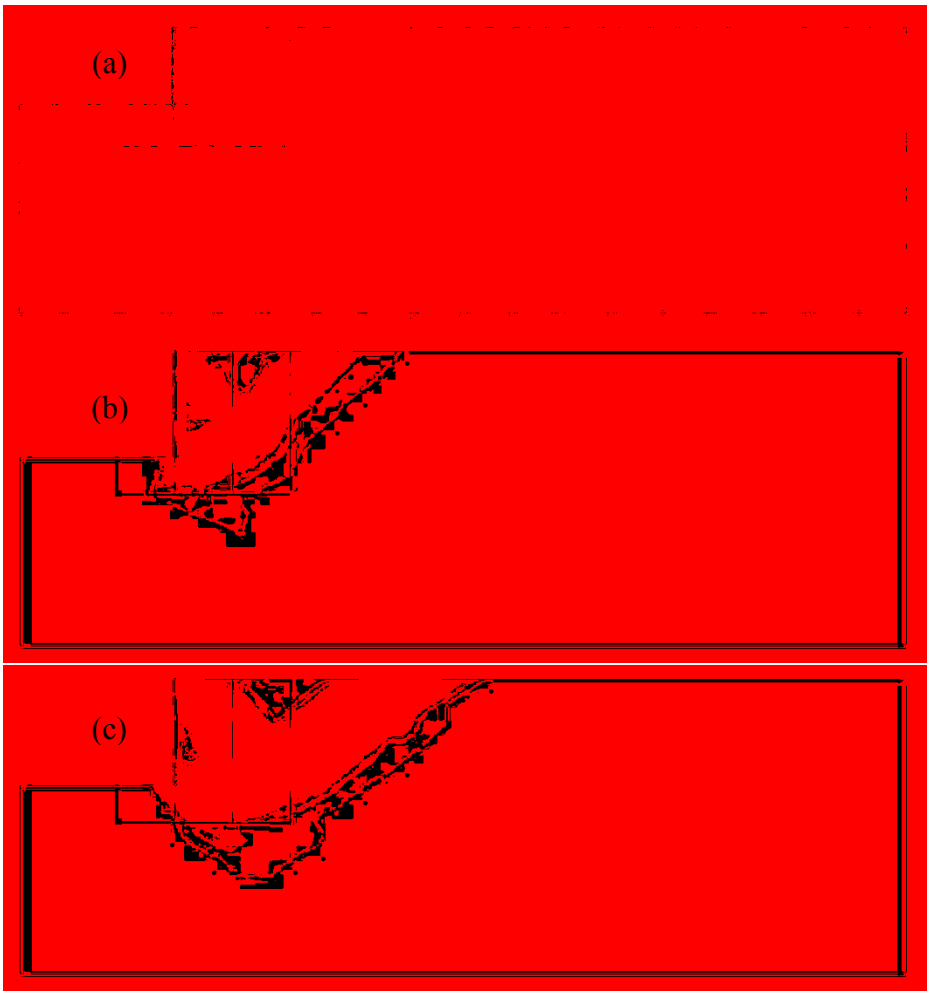

Figure 2-8: Observed Shear Planes Obtained from (a) Plaxis 2D Finite Element Models for (b) Homogeneous Sand Backfill, and (c) Homogeneous Gravel Backfill (Rollins and Nasr 2010)

2.3.3 Shamsabadi et al. 2006

Shamsabadi et al. (2006) generated a number of 3D finite element models using Plaxis 3D Tunnel (Brinkgreve 2006). Passive force deflection curves for bridge abutments at skew angles of 0°, 30°, 45°, and 60° were compared as shown in Figure 2-9. The test result indicates the passive resistance of backfill against the abutment wall decreases significantly as the abutment skewness increases.

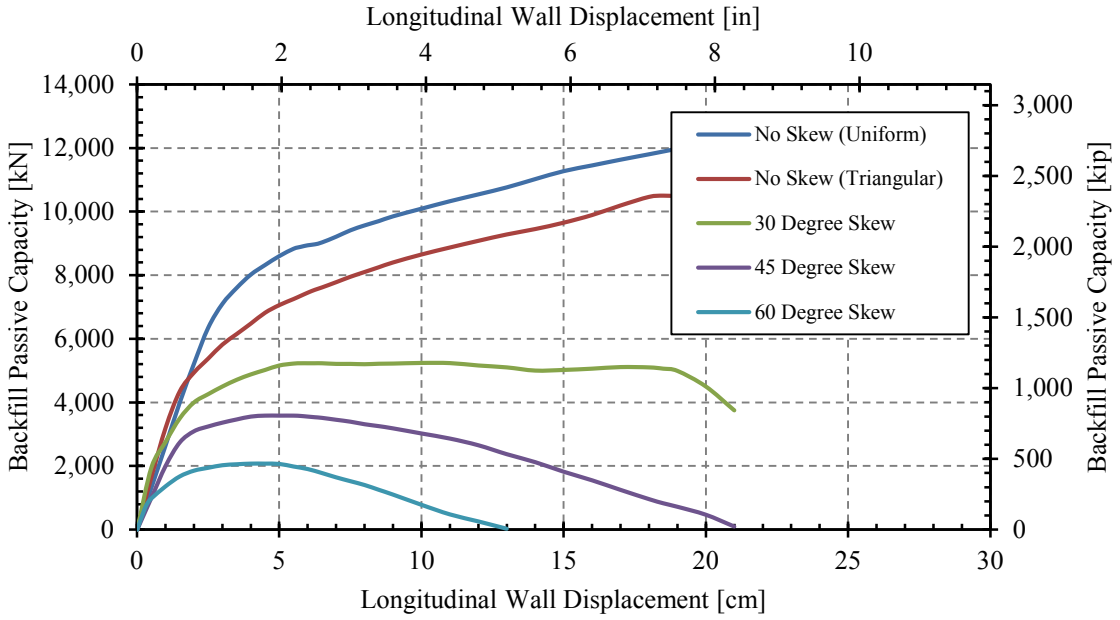

Figure 2-9: Passive Force-Deflection Curves with Different Skewness (Shamsabadi et al. 2006)

A 75 feet wide by 5.5 feet tall abutment backwall was modeled to push the soil back fill with soil parameters listed in the Table 2-5.

Table 2-5: Shamsabadi Soil Finite Element Parameters

Soil Type	γ *kN/m³ (lbf/ft³)*	ϕ	χ *kN/m² (lbf/ft²)*	δ	E_{50}^{ref} *MN/m² (kip/ft²)*	E_{ur}^{ref} *MN/m² (kip/ft²)*	ν
Silty Sand	18.8 (119.7)	34°	24 (52.2)	23°	100 (2,089)	200 (4,177)	0.35

However, as shown in Figure 2-10, when the author was modeling the pressure distribution on the face of backwall, a triangular load distribution shape was assumed on a 0° skew abutment than actually skewing the geometry of the abutment. The pressure distribution decreased linearly from a maximum at the obtuse corner of the abutment to zero at the acute corner of the abutment.

This is an approximation of the reality. Therefore, although this approach indicates the potential for a reduction in passive force with increasing skew angle, it is unclear how much of this reduction is due to the load distribution that was assumed.

Figure 2-10: Pressure Distribution Used to Simulate the Effect of a 30° Skew Angle

2.4 Constitutive Models

This section will briefly describe the soil constitutive models used in this study to model the passive force versus backwall deflection behavior of the skewed bridge abutments; namely, the Hardening Soil model. Unless otherwise noted, all information presented herein will be derived from the Plaxis Material Models Manual (PLAXIS 3D-2015).

2.4.1 Hardening Soil Model

The Hardening Soil model is an advanced model for simulating the behavior of both stiff and soft soils (Schanz 1999). It employs what is known as an expanding yield surface. The yield surface of a hardening plasticity model is not fixed in principal stress space. It can expand due to plastic straining. The yield stress is dependent on both the current stress and strain levels. In practice, this models the soil stress-strain relationship as a hyperbola similar to that shown in Figure 2-11.

The deviatoric stress, q_a, is an asymptotic value of the shear strength while q_f is the ultimate deviatoric stress. E_i is the initial stiffness of the stress-strain curve. E_{50} is the confining stress dependent stiffness modulus for primary loading and E_{ur} is the Young's Modulus for unloading and reloading. The stress strain curve exhibits a parabolic shape with a reducing rate of change in stress values. The stress-strain curve finally increases towards the asymptote, but is limited to the ultimate value of q_f

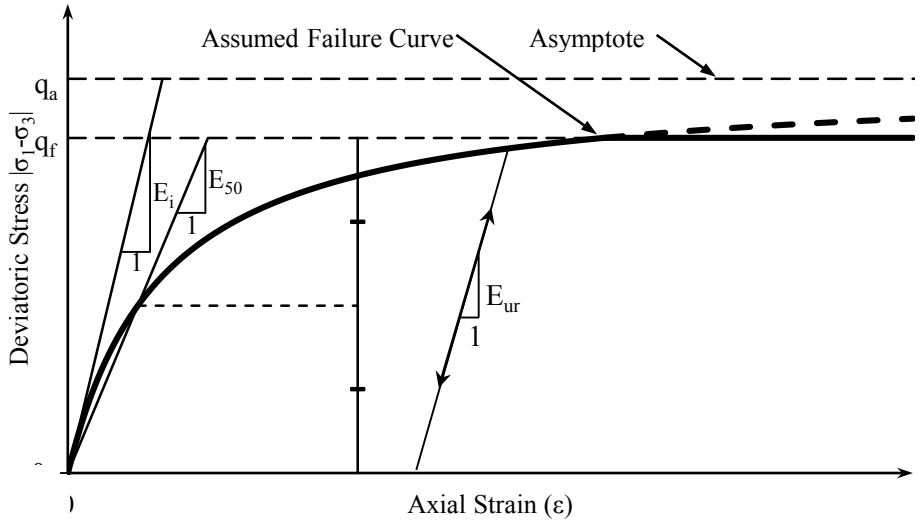

Figure 2-11: Typical Hyperbolic Soil Stress-Strain Relationship for Standard Triaxial Test used by Hardening Soil Model (PLAXIS 3D-2015)

Input parameters for the Hardening Soil model are summarized in Table 2-6. Calibration of parameters will be discussed in Section 4.3

Table 2-6: Plaxis Model Parameters for Hardening Soil Model

Symbol	*Parameter*	*Default Units*
	Failure parameters	
c	(Effective) cohesion	[lb/ft^2]
ϕ	(Effective) angle of internal friction	[°]
ψ	Angle of dilatancy	[°]
R_{inter}	Interface Friction Ratio	
	Basic soil stiffness parameters	
γ_{unsat}	Unsaturated Unit Weight	[lb/ft^3]
γ_{sat}	Saturated Unit Weight	[lb/ft^3]
E_{50}^{ref}	Secant stiffness in standard drained triaxial test	[lb/ft^2]
E_{oed}^{ref}	Tangent stiffness for primary oedometer loading	[lb/ft^2]
E_{ur}^{ref}	Unloading/reloading stiffness (default $E_{ur}^{ref} = 3E_{50}^{ref}$)	[lb/ft^2]
m	Power for stress-level dependency of stiffness	[-]
	Advanced parameters	
ν_{ur}	Poisson's ratio for unloading-reloading (default $\nu_{ur} = 0.2$)	[-]
p^{ref}	Reference stress for stiffness (default $p^{ref} = 100$ kN/m^2)	[lb/ft^2]
K_0^{nc}	K_0-value for normal consolidation (default $K_0^{nc} = 1 - sin\phi$)	[-]
R_f	Failure ratio q_f/q_a (default $R_f = 0.9$)	[-]
$\sigma_{tension}$	Tensile strength (default $\sigma_{tension} = 0$ stress units)	[lb/ft^2]
c_{inc}	Incremental increase in cohesion with depth (default $c_{inc} = 0$)	[lb/ft^2]
	Alternative soil stiffness parameters	
C_c	Compression index	[-]
C_s	Swelling index or reloading index	[-]
e_{init}	Initial void ratio	[-]

3 FIELD TESTS

This chapter will discuss the site location, geotechnical properties of the site and backfill material, and test setup for the physical tests that will ultimately be modeled using the Plaxis 3D finite element model. Towards the end of this chapter, final field test results will be presented as preparation to compare with finite element results. The series of tests were conducted by several groups of students in Brigham Young University. (Rollins and Marsh 2013, Rollins and Smith 2014)

3.1 Site Description

The field tests were conducted at a site approximately 1000 feet (305m) north of the Salt Lake City Airport Control Tower as shown in Figure 3-1.

Several tests have been performed at this site, including those which were conducted by Rollins and Sparks (2002), Johnson (2003), Rollins et al. (2005), Christensen (2006), Taylor (2006), and Rollins et al. (2010). Conditions at the site suited the purpose of performing large-scale field tests, based on many advantages such as available soil stratigraphic information, site security, lack of overhead obstructers, and ease of operating heavy equipment.

Figure 3-1: Site Location near the Control Tower in Salt Lake City (Retrieved from Google Map, 2015)

3.2 Geotechnical Site Characterization

Since 1995, many subsurface investigations, including cone penetration tests (CPT), dynamic cone penetration tests (DCPT), and shear wave velocity profiling, have been conducted around or at this site. No new investigations were performed for this series of test.

The subsurface conditions were derived from tests by Christensen (2006), Rollins et al. (2010) and Strassburg (2010). The soil profile as shown below was retrieved from Rollins et al. (2010).

The soil stratification profile shows that a dense compacted sandy gravel layer forms from the ground surface to depth of 6.5 feet. The alternating sand and silty clay layers started from 6.5 feet to approximately 100 feet. In order to test the behavior of pile groups in sandy clay in 2002, the upper 5 feet of compacted soil was removed. In 2004, 3 feet of clay layer was replaced with washed concrete sand. The final soil profile used herein is shown in Figure 3-2 and Figure 3-3 below.

Figure 3-2 shows the cone tip resistance, sleeve friction, pore water pressure and friction ratio for the soil below the test site. Figure 3-3 summarizes the results of laboratory tests to define the shear strength and pre-consolidations pressures along with measured profiles of shear wave velocity. The cohesive soils in the profile have an average undrained strength of about 1000 psf near the surface which increases gradually with depth.

The consolidation tests indicate that the upper portion of the profile is over-consolidated likely due to desiccation. The shear wave velocity slowly increases from about 400 ft/sec near the surface to about 700 ft/sec at a depth of 50 ft.

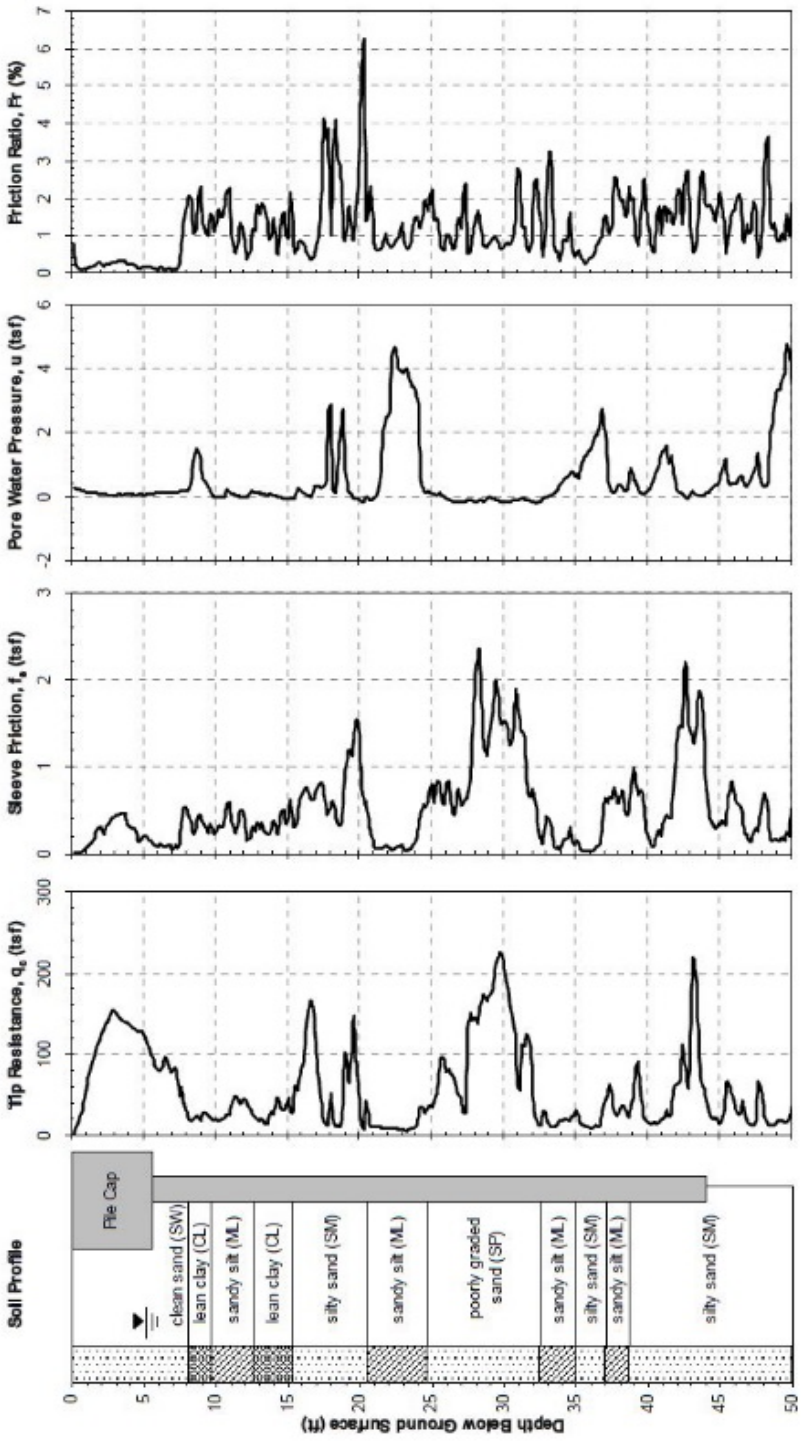

Figure 3-2: Soil Profile from CPT Test-Part 1 (Rollins et al., 2010)

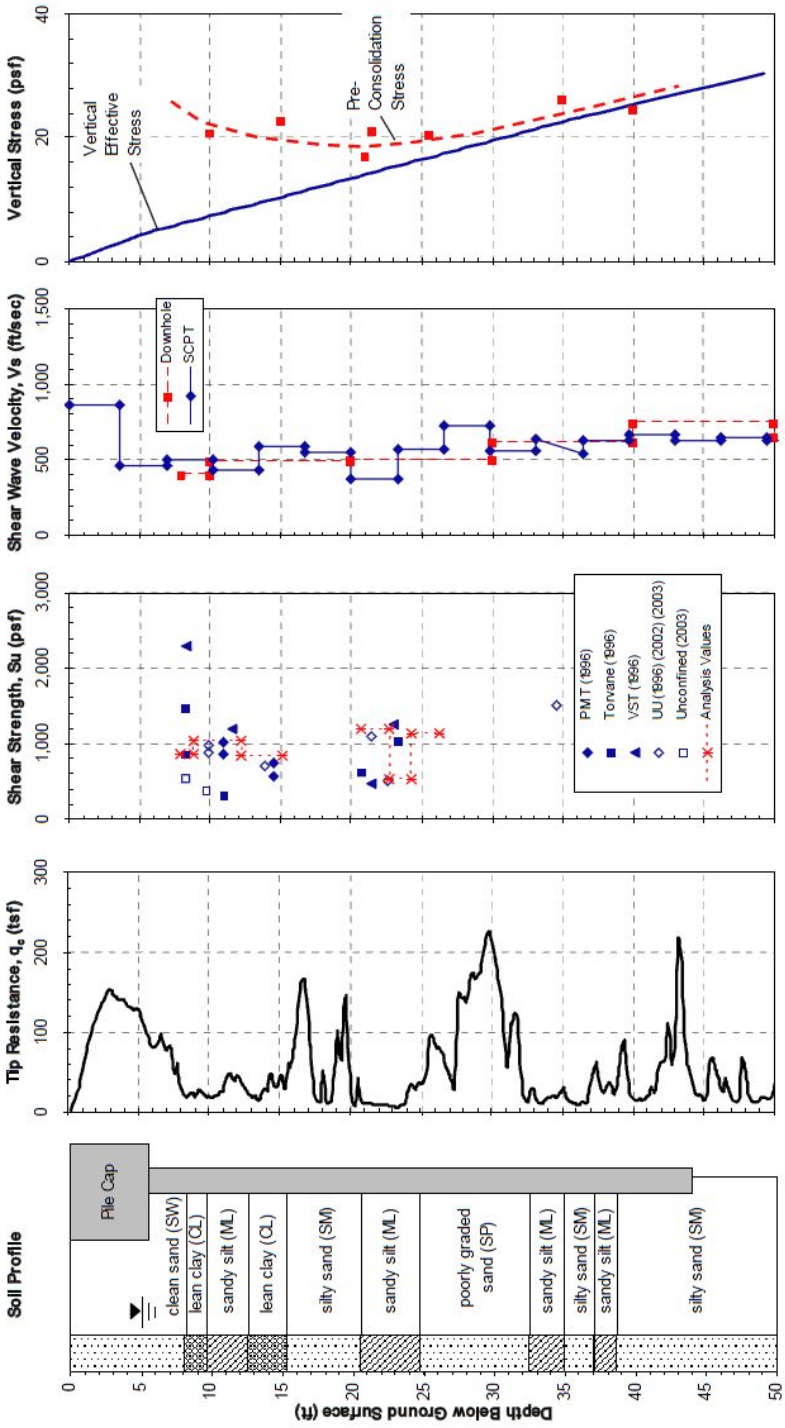

Figure 3-3: Soil Profile from CPT Test-Part2 (Rollins et al., 2010)

3.3 Test Layout

A series of lateral load tests were performed on 0°, 15°, 30° and 45° skewed abutments. These tests have been used to calibrate the finite element model analyses performed in this study. As shown in Figure 3-4, two 600 kip hydraulic actuators push against a drilled shaft and sheet pile foundation, transferring load into the skewed concrete wedges which in turn deflect into the backfill. Load and deflection measurements were made to define the passive force-deflection relationships for each wedge. This section will describe individual component of the test setup.

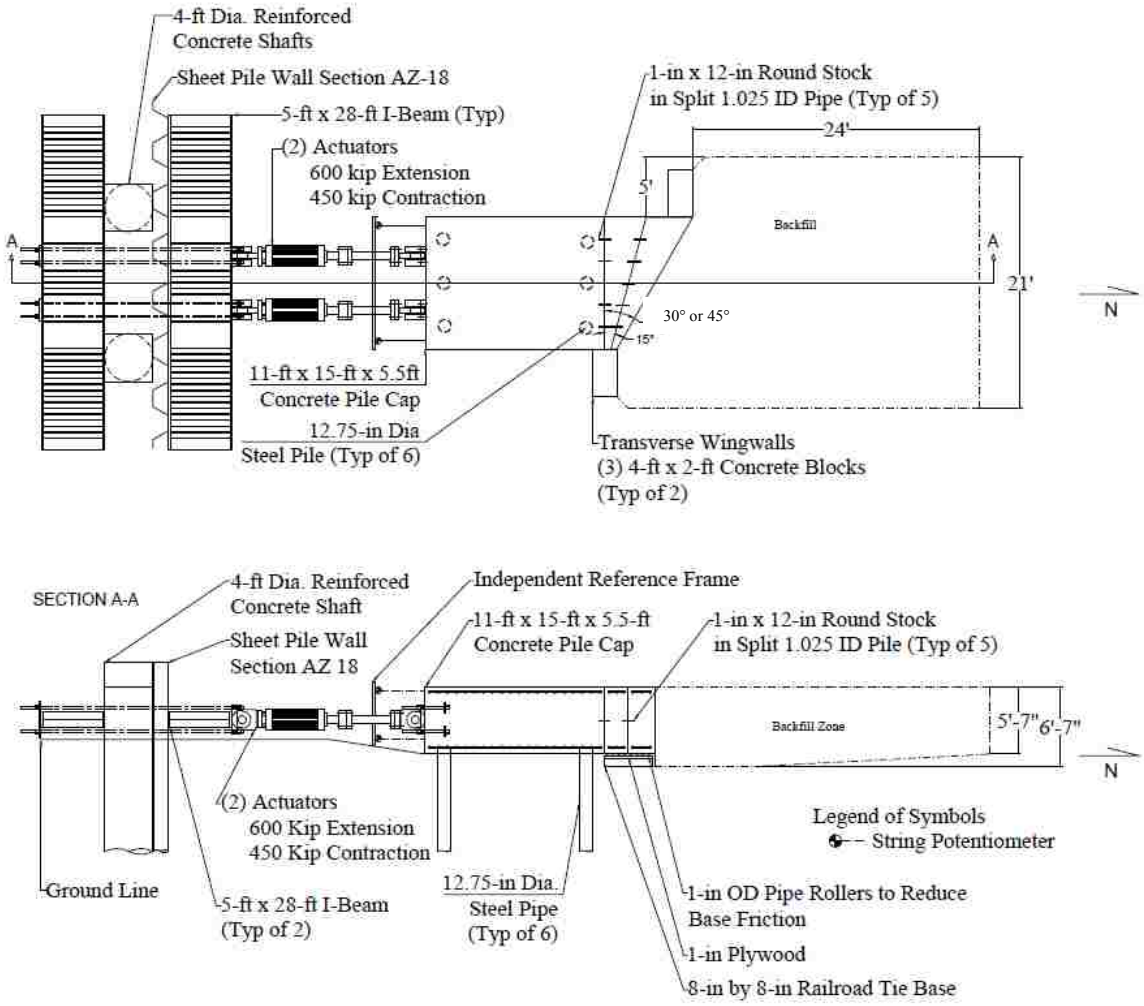

Figure 3-4: Schematic Drawing of Test Layout for Abutment with Reinforced Concrete Wingwalls.

3.3.1 Reaction Foundation

Two 4-foot diameter drilled shafts were spaced 12 feet center to center in the east-west direction along with a sheet pile wall to serve as a reaction against the actuator load. Two 5 feet by 28 feet I-beams spanned both the north and south sides of the shafts-sheet pile wall and were placed with the strong axis perpendicular to the direction of loading. The east and west drilled shafts have four-foot square by two-foot thick caps installed at tops, and the east and west drilled shafts have depths of 70.0 feet and 55.2 feet, respectively. On the north side of the drilled shafts, an AZ-18 sheet pile wall, consisting of ASTM A-572 Grade 50 steel, was installed to depths ranging from 33.6 feet to 35.6 feet by a vibratory hammer.The wide flange-beams were 28 feet long, 64 inches deep, and 16 inches wide with robust number of web stiffeners installed to prevent flange buckling during loading. Eight 1.75 inch DYWIDAGs with minimal post-tensioning were used to tie drilled shafts, sheet pile wall and I-beams together as shown in Figure 3-5.

Figure 3-5: Reaction Foundation

3.3.2 Pile Caps and Piles

The 16.4 feet long pile cap was constructed on a six-pile group. Each steel pipe pile had an outside diameter of 12.75 inches with wall thickness of 0.75 inches and was composed of ASTM A252 Grade 2 steel pipe. All closed-end pipes extended to a depth of approximately 43 feet below the ground surface. The tops of the piles extended up into the base of the pile cap by a minimum of 6 inches.

3.3.3 Concrete Wedges

All concrete wedges were constructed of 6,000 psi compressive strength to integrate with the face of pile cap, in order to form 15°, 30°, and 45° skew angles. Concrete wedges were placed on steel rollers, which reduced friction force underneath the concrete wedges, as shown in Figure 3-6.

Figure 3-6: Photo of Concrete Wedge Roller System Under Wedges

Reinforcement inside the concrete wedges was calculated by worst-case load assumptions. Maximum force was assumed to appear at the bottom acute corner of the wedge with vertical and horizontal triangular pressure distribution.

In Figure 3-7, interface connectors were designed to provide shear resistance between the pile cap and the concrete wedge, providing transverse and vertical rigidity. Top and bottom plates were also used to further insure that the pile cap and concrete wedges behaved as one rigid body.

Figure 3-7: Photo of 45 Degree Concrete Wedge with Plates to Ensure Rigid Movement

3.3.4 Loading Apparatus

Two MTS actuators were placed between the pile cap and the reaction foundation in a north-south direction as shown in Figure 3-8. The North and South actuators have compression and tension capacity of 600 kips and 450 kips, respectively. The centers of the two actuators were both placed in a horizontal plane at a distance of 2.75 feet above the ground level.

Figure 3-8: MTS Hydraulic Actuators Layout

3.4 Geotechnical Backfill Properties

This section will describe backfill properties such as soil gradation, relative compaction, unit weight, strength parameters.

3.4.1 Backfill Zone

The backfill zone, located at the north of the abutment backwall, was 24 feet long in longitudinal direction and 21 feet wide in the transverse direction. To allow the potential log-spiral failure surface to develop the backfill extended approximately 1 foot below the base of the pile cap. However, the depth of the backfill tapered upward beyond a distance of about 10 ft as shown in Figure 3-4.

3.4.2 Backfill Soil Characterization

Approximately 250 tons of poorly graded sand with 7% moisture content were used as backfill material. The sand was classified as SP type soil according to the Unified Soil Classification System or an A-1-b type soil according to the AASHTO Classification System. Figure 3-9 shows the pre-testing and post-testing gradation plots (Rollins and Smith 2014). The measured grain-size distribution curves generally fell within the gradation limits of washed concrete sand (ASTM C33). Pre-and post-particle size distribution varied slightly due to possible reasons such as variation between soil samples and contamination from sides and bottom of the backfill. Table 3-1 shows selected parameters from the particle size analysis before and after the skewed abutment tests.

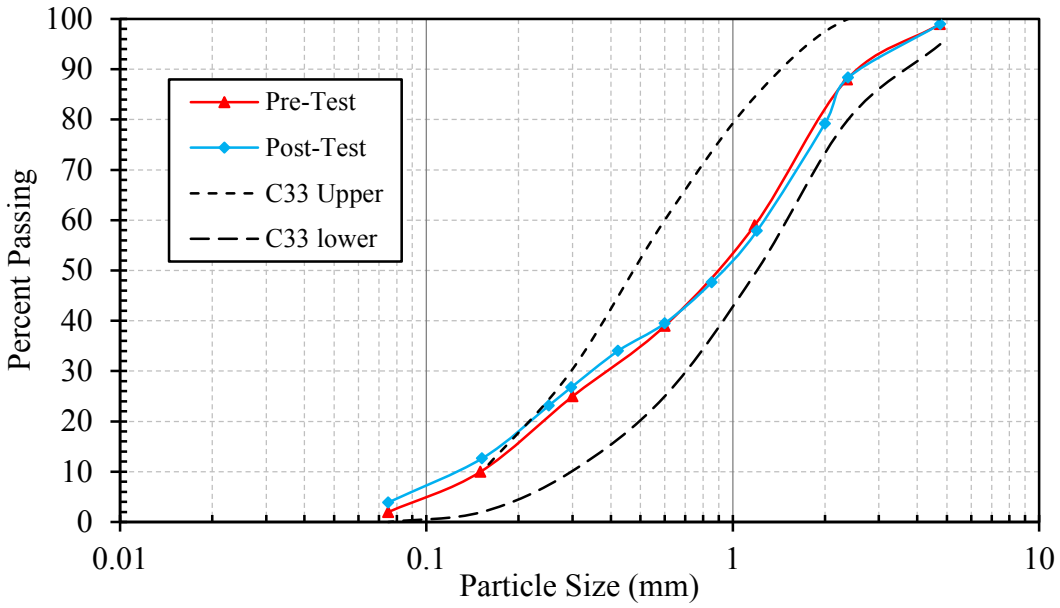

Figure 3-9: Pre-testing and Post-testing Gradation Plots (Rollins and Smith 2014)

Table 3-1: Soil Gradation Characteristics, Pre- and Post-Testing, Adapted from Rollins and Marsh (2013)

	Sand	*Fines*	D_{60}		D_{50}		D_{30}		D_{10}		C_u	C_c
	[%]	[%]	[in]	[mm]	[in]	[mm]	[in]	[mm]	[in]	[mm]		
Pre-Test	98.0	2.0	1.22	(31.0)	0.9	(22.9)	0.4	(10.2)	0.16	(4.1)	7.6	0.8
Post-Test	96.1	3.9	1.26	(32.0)	0.92	(23.4)	0.34	(8.6)	0.13	(3.3)	9.7	0.7

3.4.3 Backfill Soil Shear Strength

Backfill soil cohesion (c) and friction angle (ϕ) were determined from direct shear tests (ASTM D 3080) in the Brigham Young University soils laboratory (Rollins and Marsh 2013) and direct shear tests in the field.

Normal stresses for the direct shear tests were selected with values of 4.1, 8.2, 16.3, and 24.5 psi. Tests were conducted at both the compaction moisture content, and saturated conditions. Horizontal load-deflection plots are shown in Figure 3-10 and Figure 3-11 for moist and saturated tests, respectively. Normal stress versus shear stress plots are shown in Figure 3-12 and Figure 3-13, respectively. Backfill properties are listed in Table 3-2.

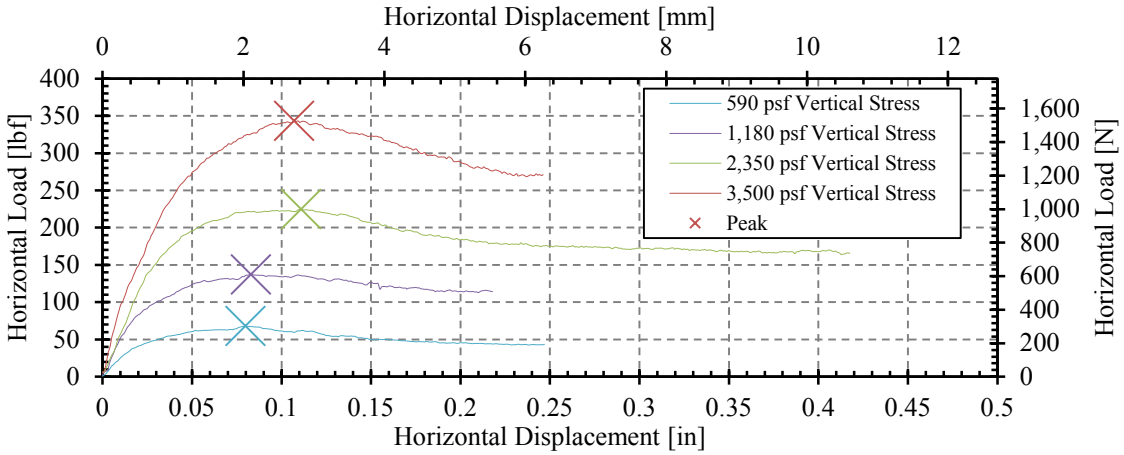

Figure 3-10: Horizontal Load-Deflection Plots for Direct Shear Tests with Moist Samples (Rollins and Marsh 2013)

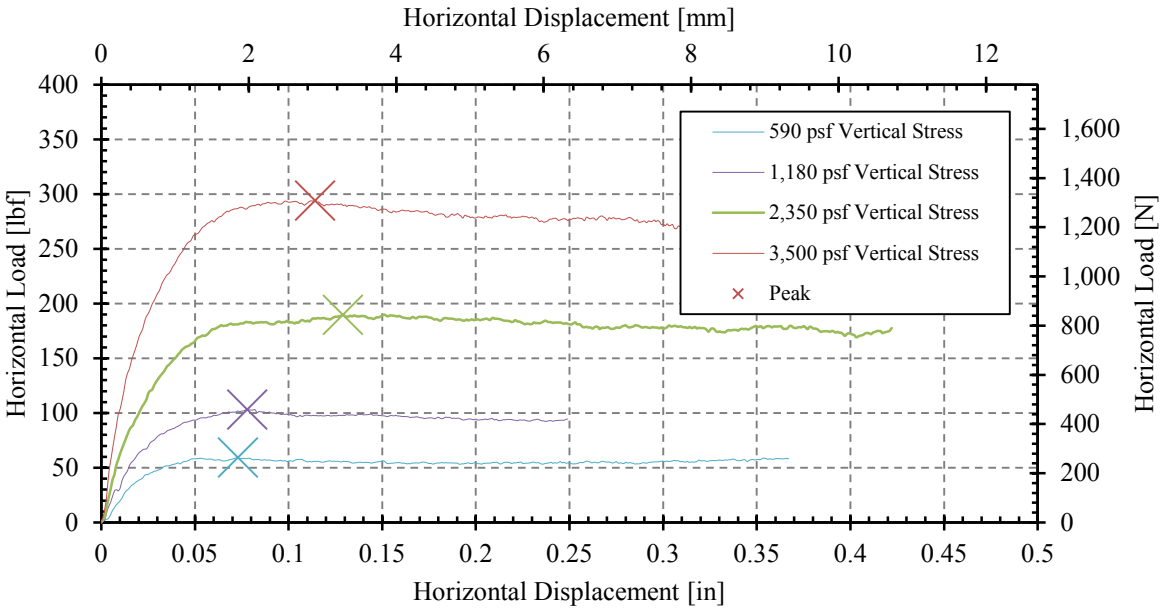

Figure 3-11: Horizontal Load-Deflection Plots for Saturated Direct Shear Tests (Rollins and Marsh 2013)

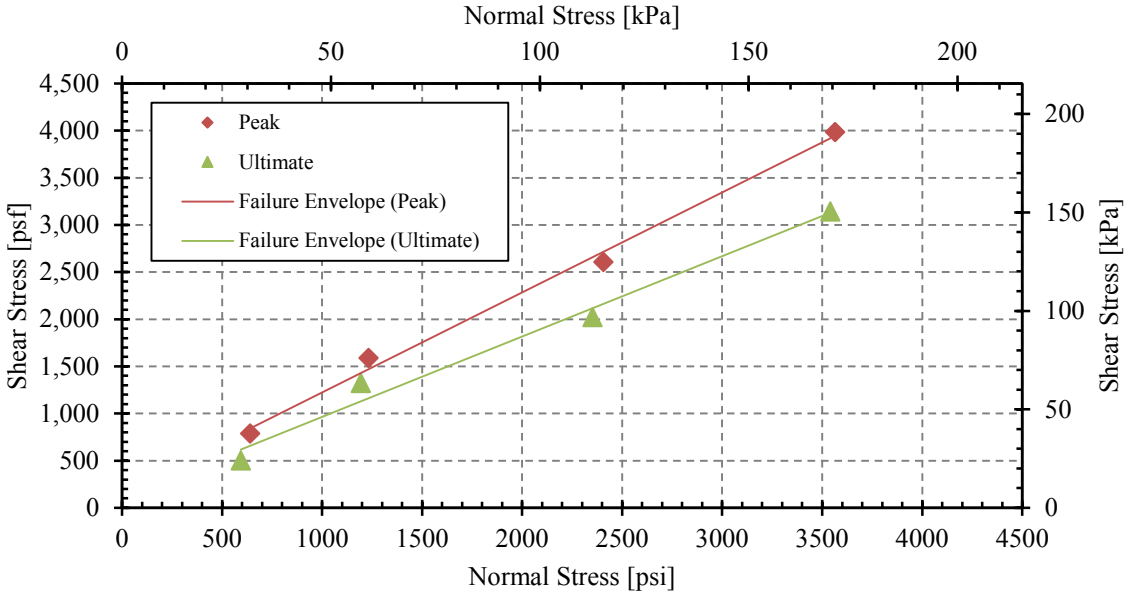

Figure 3-12: Normal Stress versus Shear Stress Plots for Dry Tests (Rollins and Marsh 2013)

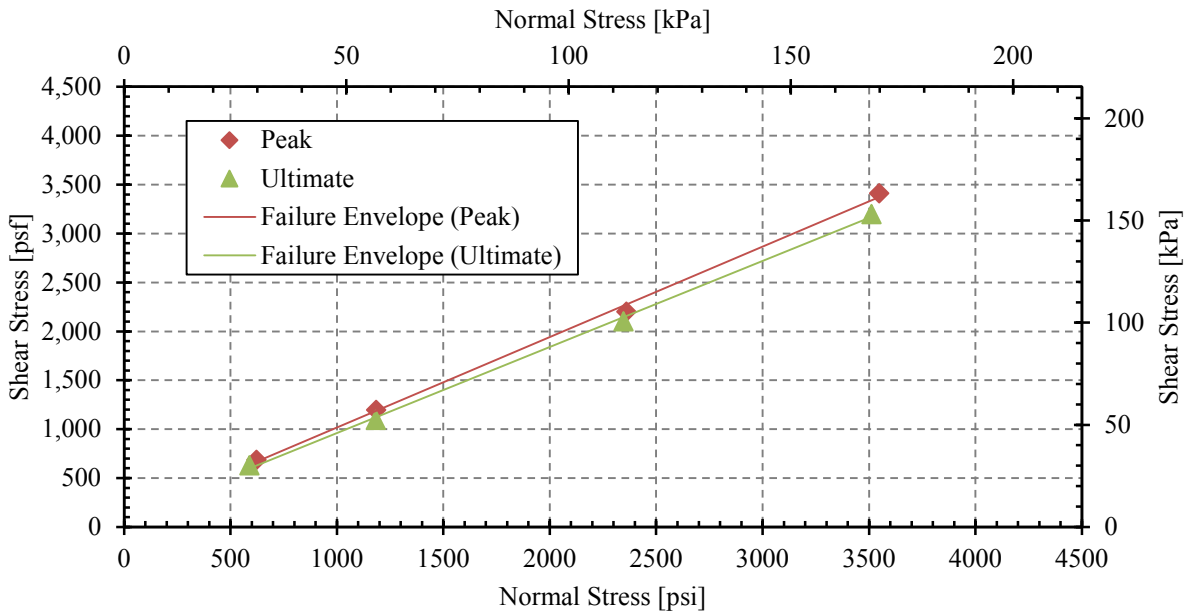

Figure 3-13: Normal Stress versus Shear Stress Plots for Saturated Tests (Rollins and Marsh 2013)

Table 3-2: Backfill Strength Parameters (Rollins and Marsh 2013)

Source of Test Result	*Peak*		*Ultimate*	
	ϕ	*c (psf)*	*ϕ*	*c (psf)*
Direct Shear (dry)	46.7°	161.6	40.4°	113.8
Direct Shear (dry, cohesionless)	48.3°	0	41.8°	0
Direct Shear (submerged)	42.7°	92.9	41.4°	78.8
Direct Shear (submerged, cohesionless)	43.8°	0	42.3°	0

In-situ direct shear tests were performed at the site. A 1.5 feet long by 1.5 feet wide by 8 in high shear box was used to contain a block of sand. The sand block was scraped from the edge of the shear box first, and then it was gradually tapped down until the top of the sand block was flush with the top of the box. Two tests were performed with 30 and 47 weights providing the normal force, with each weighing 16 kilograms. As shown in Figure 3-14, a bottle jack pushed the shear box. Force and deflection results were measured simultaneously. Results indicate that the

soil back fill has a soil friction angle of ϕ=41.9° and an apparent cohesion of c=191psf. These values were similar to the lab direct shear test.

Figure 3-14: In-situ Direct Shear Test Setup.

3.5 General Testing Procedure and Results

The backfill sand was compacted in 6 to 8 inch thick layers using a vibratory drum roller and a walk behind vibratory plate compactor. The backfill eventually reached a height of a 5.5 feet about the base of the pile cap with density greater than or equal to 95% of the modified proctor value. During compaction, water was sprayed over each layer in order to obtain the proper moisture content. On top of the backfill, a 2-foot grid square was painted and red-dyed sand columns were installed as shown in Figure 3-15.

Figure 3-15: Photo of Painted Grid on the Ground Surface to Define Heave

After the backfill was set up, and initial readings were taken. Two hydraulic actuators started to push the bridge abutment into the backfill at a velocity of 0.25 inches per minute. At approximately each 0.25 inches displacement increment, were taken to measure force and displacements. This procedure continued until the maximum displacement reached approximately 3.25 inches to 3.75 inches.

The results were presented as follows and the finite element modeling results will be compared accordingly in Chapter 1.

3.5.1 Load Displacement Relationship

Before backfill was put in place, a baseline load versus deflection test was conducted in order to measure the pile resistance alone from the abutment. The baseline resistance provided by

the piles was subtracted from the measured force to obtain the longitudinal force as shown below in equation (3-1). Passive force was obtained afterwards by multiplying by the cosine of the skew angle as shown in equation (3-2) as proposed by Burke (1994).

$$P_L = (P_{total} - P_{baseline}) \quad (3\text{-}1)$$

$$P_p = P_L cos\theta \quad (3\text{-}2)$$

Where P_{total} = total actuator load required to displace abutment into backfill,

$P_{baseline}$ = actuator load required to displace abutment with no backfill,

θ = skew angle.

The load-displacement curves for 0°, 15°, 30° skew (Rollins and Marsh 2013), and 45° skew angles abutments were plotted in the Figure 3-16. Maximum passive force for each test occurred between 2 to 3 inches which is approximately 3 to 5% of the backwall height. Passive force in 45 degree skew set kept increased up to a deflection of 3.0 inches or 4.7% of the wall height. As shown in Table 3-3, the maximum passive force decreases with increasing skew angle.

Table 3-3: Summary of Maximum Passive Force Measurements versus Skew Angle

Skew Angle	*Max value occur at (in)*		*Max Values (kips)*		*% decrease*
	in	mm	kips	kN	
0°	3	(76.2)	478	(2126)	N/A
15°	2	(50.8)	348	(1547)	27
30°	2	(50.8)	277	(1233)	20
45°	3	(76.2)	171	(761)	38

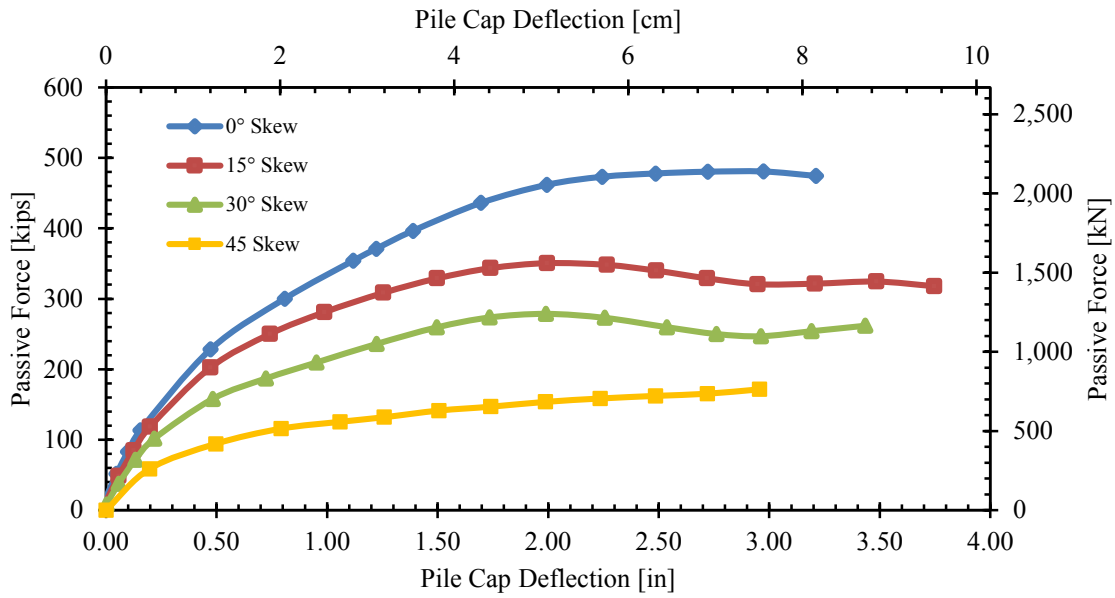

Figure 3-16: Passive Force versus Deflection Curves for Four Skew Angles (Rollins and Marsh 2013)

3.5.2 Heave Contours and Surface Cracks

Plots of the heave contours and surface cracks at the completion of the 0°, 15°, 30° (Rollins and Marsh 2013) and 45° skew tests are shown in Figure 3-17, Figure 3-18, Figure 3-19, and Figure 3-20, respectively. Heave measurements were taken using a total station. Maximum heave values were reported in Table 3-4. The location of maximum heave for 15°, 30° and 45° skew tests was observed to be near the acute corner of the pile caps (west side). In contrast, for the zero skew tests, the heave pattern was essentially symmetric about the centerline. In all cases maximum heave was nearly 3% to 4% of the maximum height of the backfill [5.5 ft (1.68 m)].

The 0°, 15°, and 30° skew tests appeared to exhibit similar surface crack widths and lengths. In these cases, the failure bulb extended approximately 20 feet (6.10 m) wide when measured parallel to the face of the backwall, and 17 feet (5.2 m) long when measured perpendicular to the backwall face. However, in contrast to the non-skewed case where the shear

planes were essentially symmetric longitudinally, the failure bulb for the skewed tests was skewed towards the acute side. Surface cracks for 45° skew were minimal and spread outward from the corners of the pile cap on the unconfined backfill after 2.96 in of longitudinal displacement. For the 15°, 30° and 45° skew tests, the surface cracking was normal to the wall face on the obtuse corner but parallel to the wall face on the acute corner.

Table 3-4: Max. Heave for Different Skew Sets

Skew Angle	*Max Heave (in) in*	*(mm)*	*% of Wall Height*
0°	1.8	70	3
15°	2.75	56	4
30°	2.2	43	3
45°	1.7	76	3

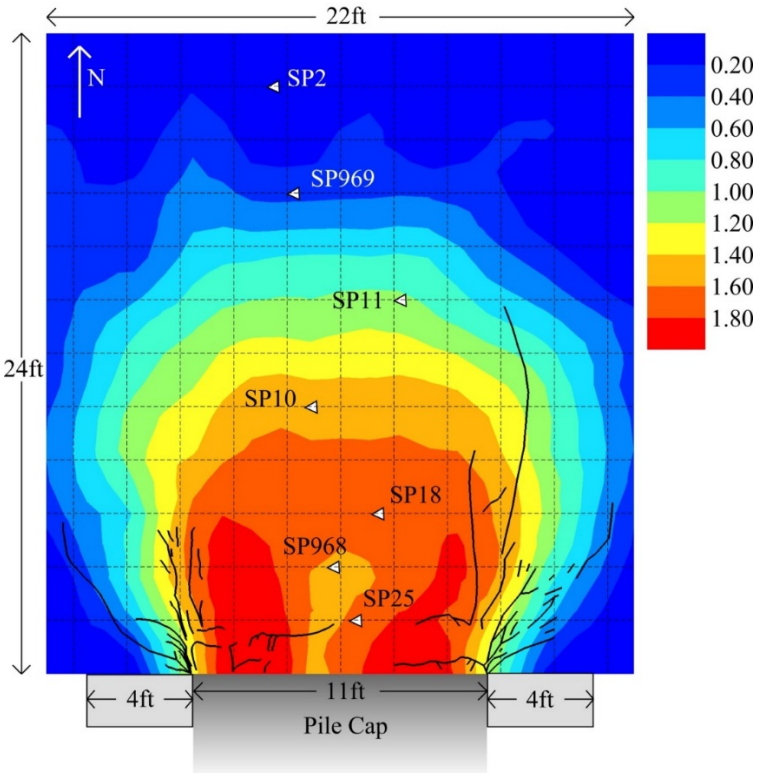

Figure 3-17: Backfill Heave Contours, Final Surface Cracks, and String Pot Locations on a 2-ft (0.61-m) Grid for the 0° Test (Rollins and Marsh 2013)

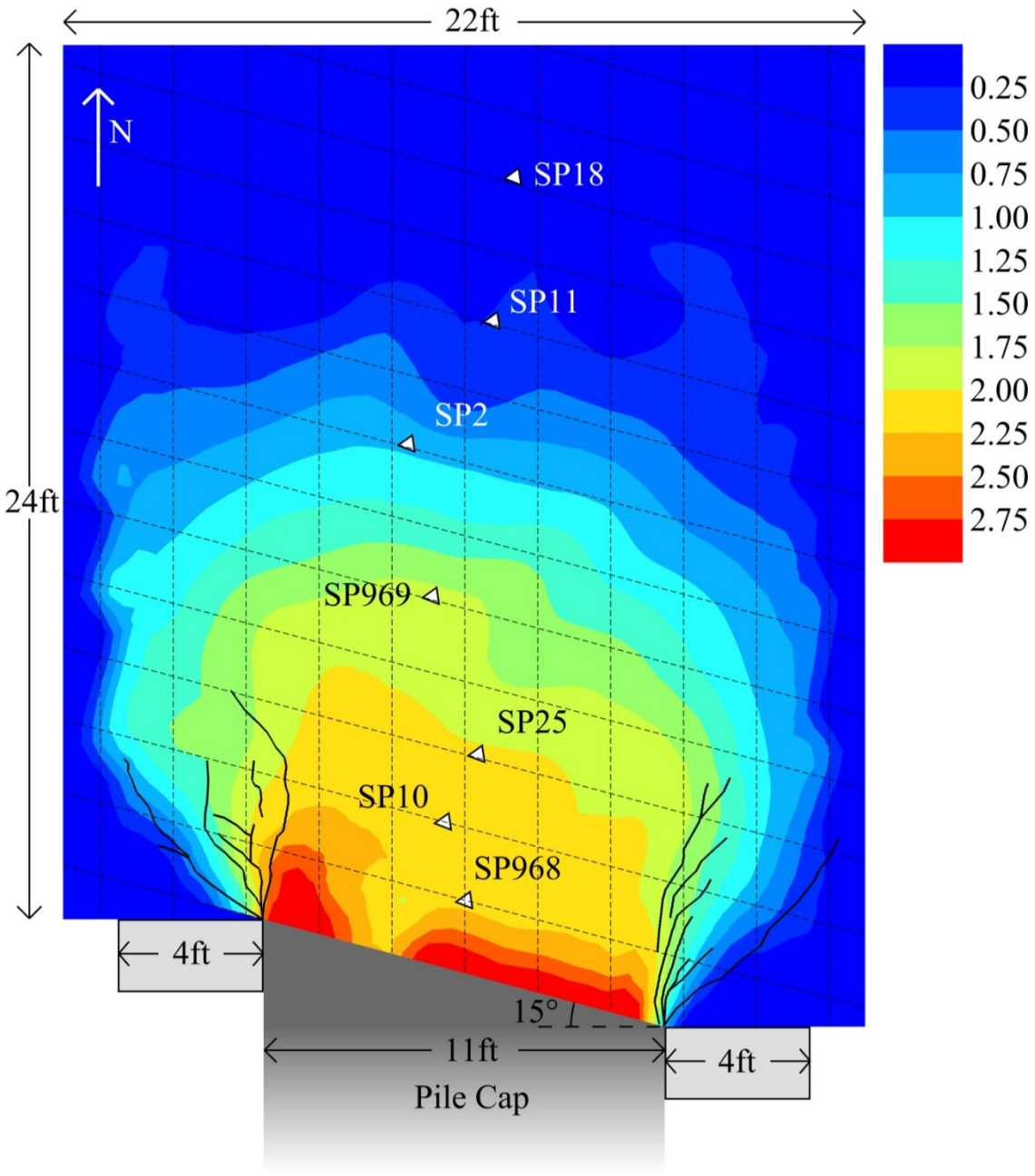

Figure 3-18: Backfill Heave Contours, Final Surface Cracks, and String Pot Locations on a Skewed 2-ft (0.61-m) Grid for the 15° Test (Rollins and Marsh 2013)

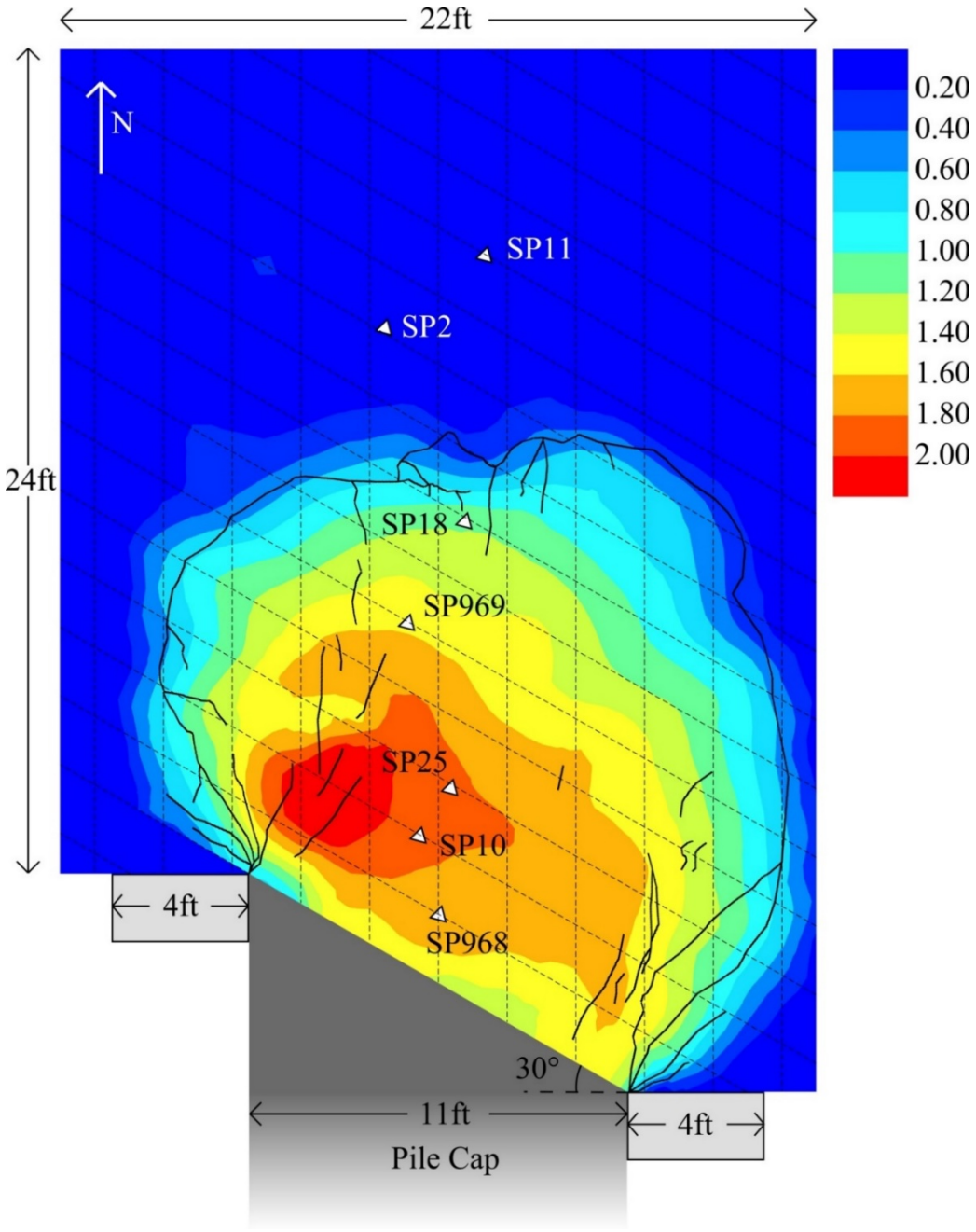

Figure 3-19: Backfill Heave Contours, Final Surface Cracks, and String Pot Locations on a Skewed 2-ft (0.61-m) Grid for the 30° Test (Rollins and Marsh 2013)

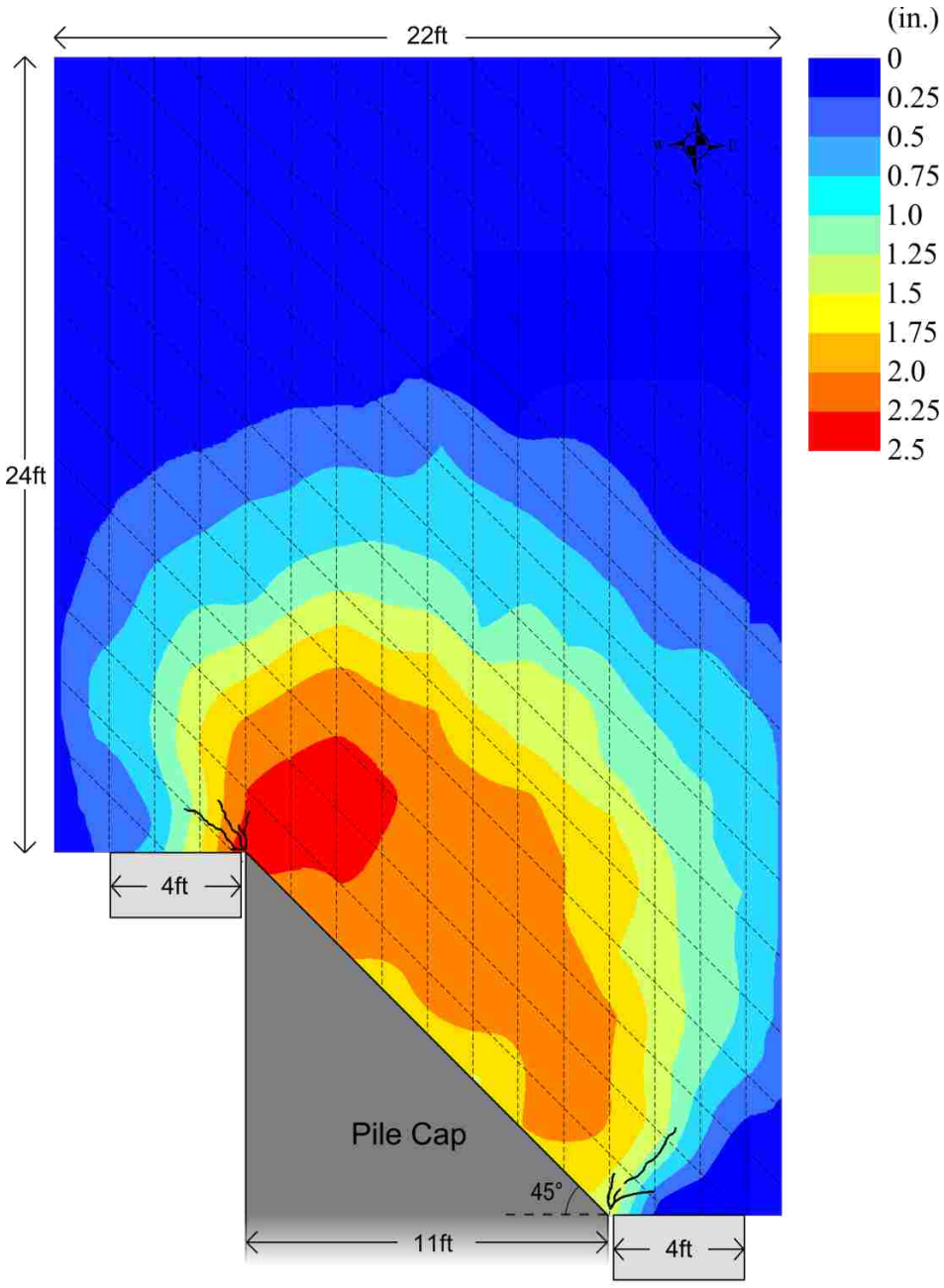

Figure 3-20: Backfill Heave Contours, Final Surface Cracks on a Skewed 2-ft (0.61-m) Grid for the 45° Test (Rollins and Smith 2014)

3.5.3 Internal Failure Surfaces

Figure 3-21, Figure 3-22, Figure 3-23 and Figure 3-24 (Rollins and Marsh 2013, Rollins and Smith 2014) show the internal failure surfaces for the 0°, 15°, 30° and 45° tests, respectively.

The internal failure planes were similar to the shear planes for a log-spiral failure described by Terzaghi (1943). A curved lower shear plane extended first downward from the bottom of the backwall with a log-spiral shape and then became relatively linear as it extended upward to the surface of the backfill at an angle approximately equal to $45° - \phi/2$. In addition, an upper shear plane descended from the top of the backwall to intersect the rising shear plane at an angle also approximately equal to $45° - \phi/2$. Rollins and Nasr (2010) in their finite element analysis also showed those shear planes and speculated that they were the interface between the Prandtl (log-spiral) and Rankine (triangular) failure zones.

Upper shear planes were not observed for the 30° test. The lower shear surface progressed up from the bottom of the backwall to the backfill surface in a nearly linear pattern.

Lower shear planes were observed for the 45° test which is similar to the shear plane fashion in the 30° test up to 4 feet away from the backwall; however, the failure plane could not be identified beyond this distance. Perhaps the pile cap deflection was insufficient to develop the failure plane completely. Information was missing for the rest of the backfill Upper shear plane were not observed. Perhaps there was insufficient movement to develop the failure planes.

Different behavior in 30° and 45° tests may result from low lateral resistance from pile caps in the field tests. Low wall friction between the back wall and backfill caused the backwall to slip into the soil backfill. This phenomenon will be discussed in the Section 5.1.1.

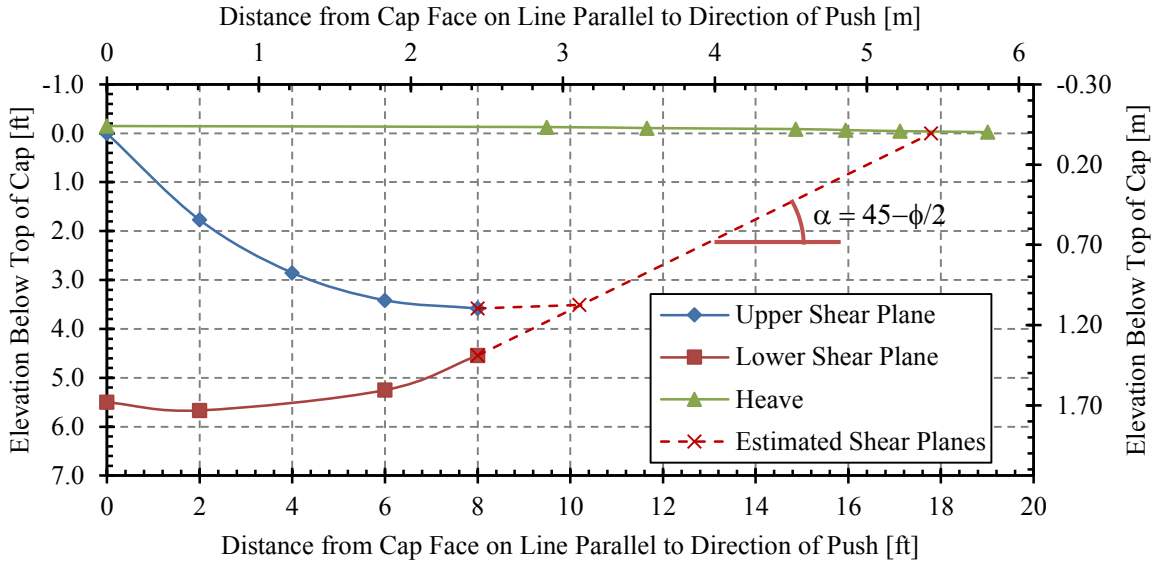

Figure 3-21: Internal Failure Surfaces for the 0° Test (Rollins and Marsh 2013)

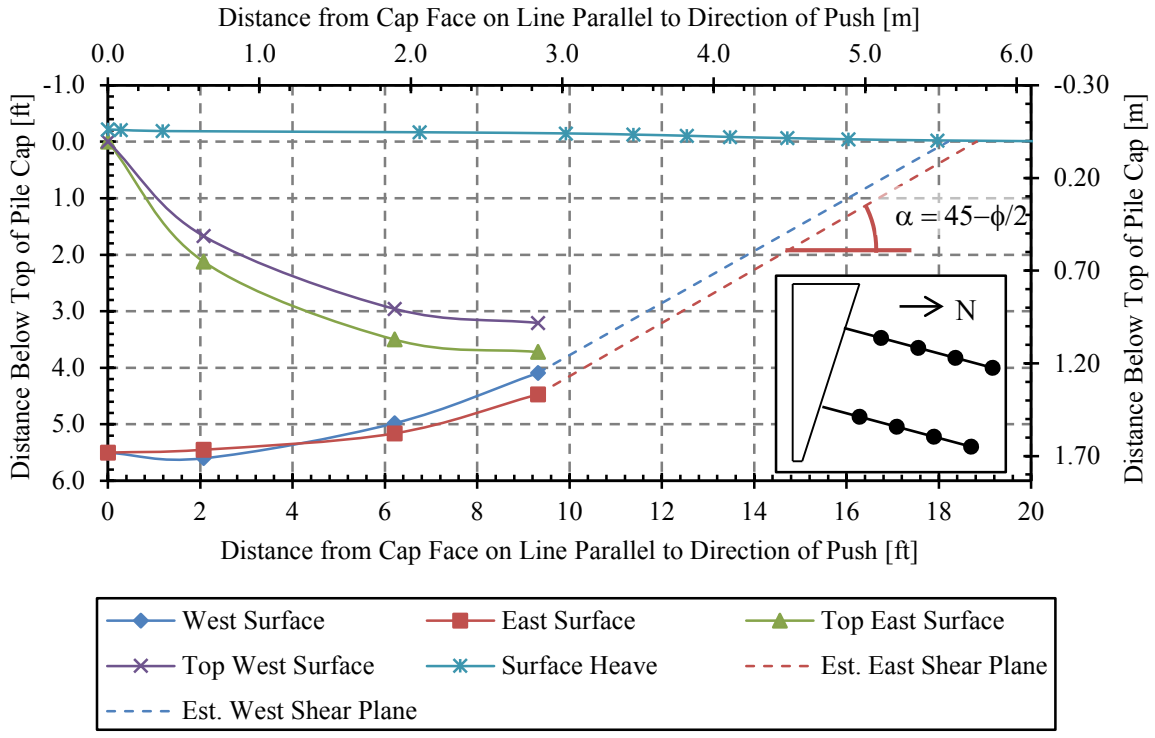

Figure 3-22: Internal Failure Surfaces for the 15° Test (Inset shows locations sand columns) (Rollins and Marsh 2013)

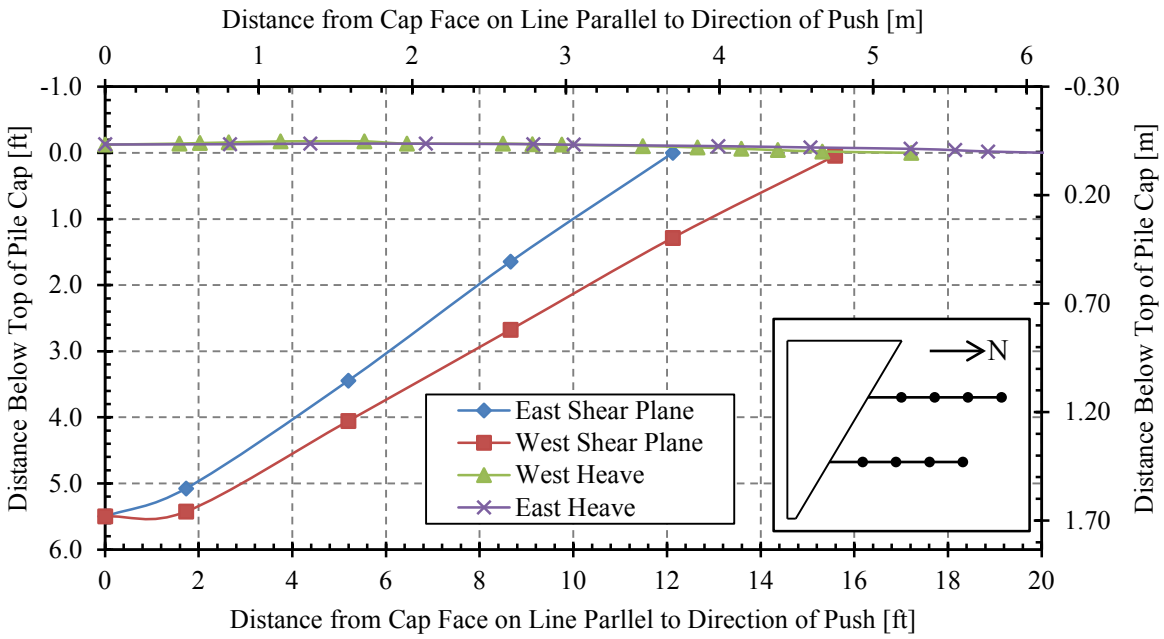

Figure 3-23: Internal Failure Surfaces for the 30° Test (Inset shows location of sand columns) (Rollins and Marsh 2013)

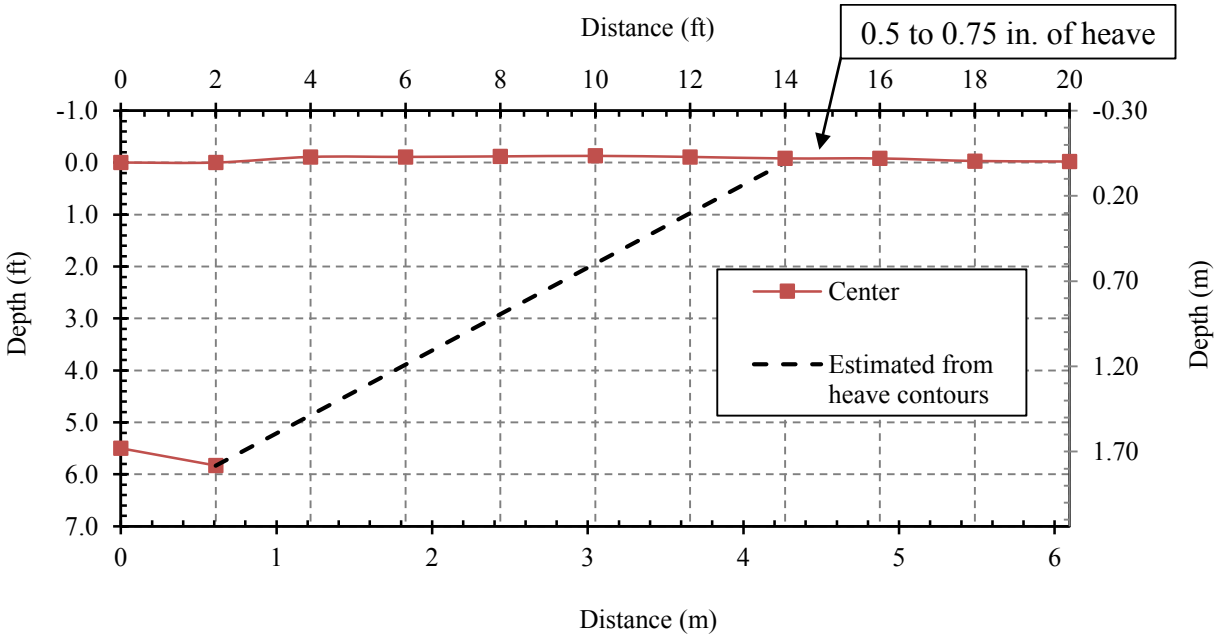

Figure 3-24: Internal Failure Surfaces for the 45° Test (Rollins and Smith 2014)

4 OVERVIEW OF PLAXIS 3D

Information presented in this section is based on the Plaxis 3D Reference Manual and the Plaxis 3D Materials Manual (PLAXIS 3D-2015).

4.1 Geometry Modeling

Plaxis 3D 2012 is a three-dimensional finite element analysis software package designed to analyze the non-linear properties of soil and rock as well as soil-structure interaction problems. Like other programs published by Plaxis, the software package is broken into a number of subprograms; in this particular case the subprograms are Plaxis 3D Input, and Plaxis 3D Output.

Plaxis 3D Input is used for defining the project geometry, material sets, boundary conditions, and calculation phases. Plaxis 3D Output is used to view the results of the finite element analysis, including deformed geometry and cross section views, and to plot various relationships between soil deformations, load, etc.

To begin, a conceptual model should be created in the Plaxis Input program that represents soil conditions and structural systems. Soil stratigraphy and water table elevations are defined by

creating “boreholes” at specific locations. If only one borehole is used in the model (as is the case with this series of tests) the characteristics of that borehole define the soil stratigraphy for the entire model. Once the soil layers have been defined, relevant structural geometries can then be defined.

Following the creation of a geometric model, soil and structural material properties, as well as loads and prescribed displacements should be defined. Soil parameters (e.g. friction angle, cohesion, stiffness, etc.) should then be selected based on the chosen soil constitutive model (e.g. Hardening Soil Model, Mohr-Coulomb model, Cam-Clay Model, etc.). However, structural properties (e.g. Young’s Modulus, Poisson’s ratio, plate element thickness, etc.) are defined the same regardless of the selected soil constitutive model.

Once all model geometries are defined, a 3-dimensional tetrahedral mesh can be applied to the model. Options for refining or coarsening the entire mesh at local points, lines, surfaces, or volumes are also available.

Just prior to performing calculations, Gaussian stress points can be selected in the model for which Plaxis will save all calculation data. This data can then be used to generate relationships between, for example, stress and strain, or load and displacement. During the calculation phase, data from each calculation step is saved for these selected points. However, if no points are selected prior to performing calculations, these relationships can still be determined, though the maximum number of step data points saved must be specified prior to performing calculations. This procedure instructs the program to save the data associated with all points for the specified number of calculation steps.

After meshing is complete, calculation stages can be defined. Calculation stages can be used for a number of different purposes. Most often, calculation stages are used to simulate construction stages. For example, when modeling an excavation, one might model the installation

of sheet pile walls as the first stage, the removal of the top level of soil as the second, the installation of soil nails the third, and so on. This method of performing calculations in stages enables the engineer to obtain a more complete picture of the soil conditions during the whole construction process.

Once the geometry and materials have been defined, and a mesh applied to the model, calculation can begin. Depending on the size and complexity of the model, this may take a few minutes, a few days, or even a week or more. Following the completion of the calculation step Plaxis 3D Output can be used to view the results of the calculation phase. Calculation results can be viewed in graphical of tabulated form. Additionally, relationships (e.g. stress-strain, load-displacement) can be plotted either for pre-selected Gaussian stress points, or for any given point in the model but with less detail than if the point had been selected prior to performing the calculation, as has been discussed previously.

4.2 Materials Modeling

As mentioned previously, Plaxis allows the use of a number of soil constitutive models with varying degrees of complexity. Models available in Plaxis include the Mohr-Coulomb model (linear-elastic perfectly plastic), the Hoek-Brown model (rock behavior), the Hardening Soil model (isotropic hardening), the Hardening Soil Model with Small-Strain Stiffness, the Soft Soil model, the Soft Soil Creep model (time dependent behavior), the Jointed Rock model (anisotropy), the Modified Cam-Clay Model, the NGI-ADP model (anisotropic undrained shear strength), and the Sekiguchi-Ohta model. Additionally, Plaxis also allows user-defined soil constitutive models. Of these models, Hardening Soil is the only one that apply specifically to the soil conditions studied in this thesis. The Mohr-Coulomb model has limitation in accuracy as discussed in section 2.4.1.

Therefore, only the Hardening Soil model will be used to compare the field test data with the computer modeling.

4.3 Development and Calibration of Finite Element Model

As outlined in Section 4.1, the first step in creating a numerical model in Plaxis is to define the project geometries. The geometric models for the 0°, 15°, 30°, and 45° skew load tests are shown in Figure 4-1, Figure 4-2, Figure 4-3 and Figure 4-4, respectively.

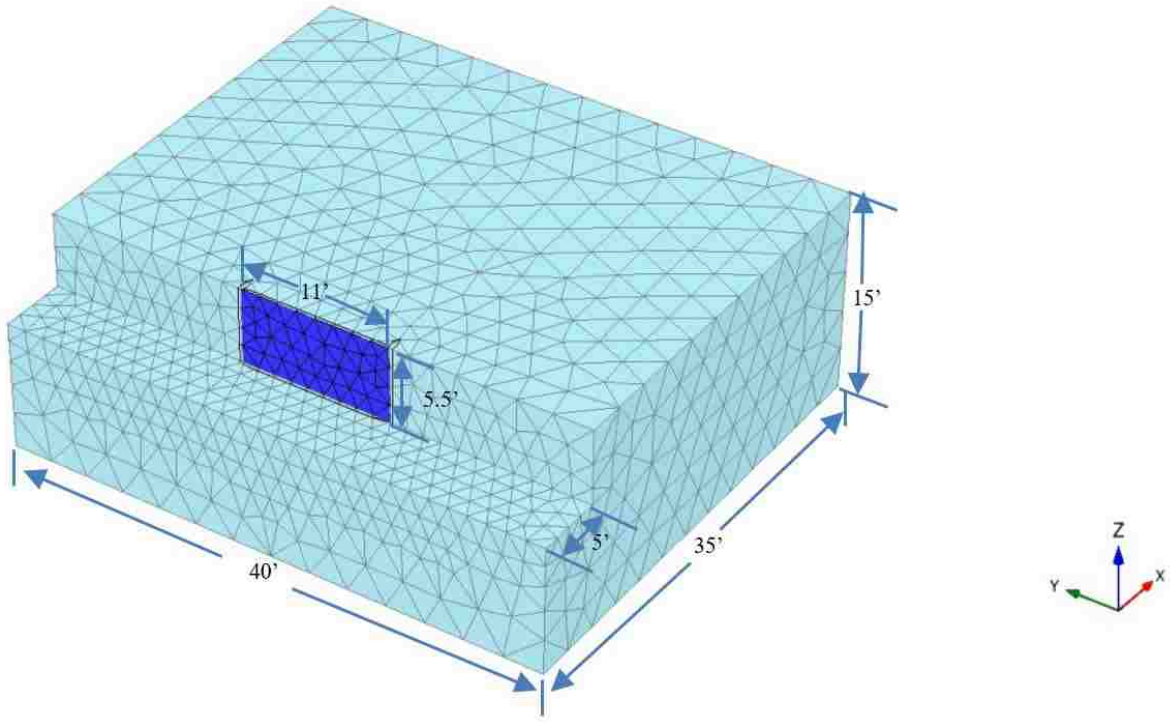

Figure 4-1: 0° Skew Finite Element Model with Dimensions

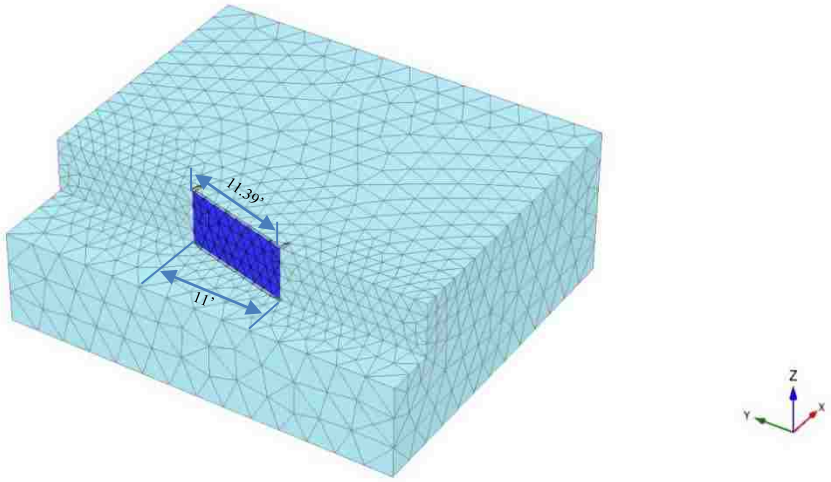

Figure 4-2: 15° Skew Finite Element Model (Other Dimensions Are the Same as 0° Skew Set.)

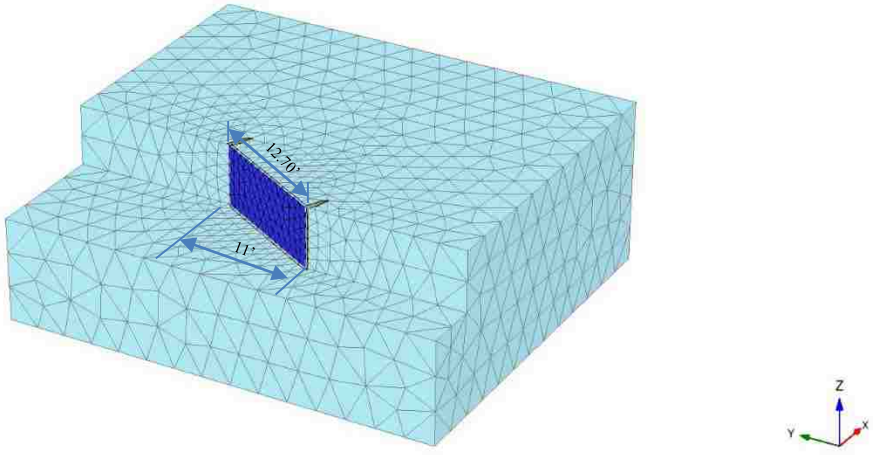

Figure 4-3: 30° Skew Finite Element Model (Other Dimensions Are the Same as 0° Skew Set.)

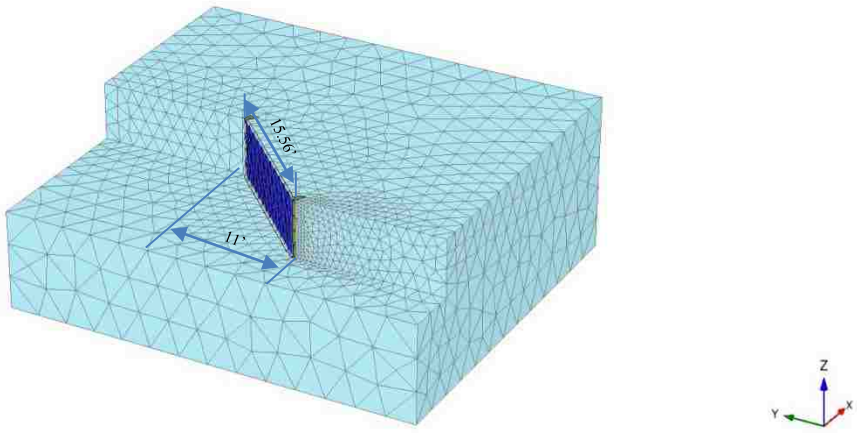

Figure 4-4: 45° Skew Finite Element Model (Other Dimensions are the Same as 0° Skew Set.)

Each model uses the automatic mesh generation option and the numbers of nodes and soil elements are listed accordingly for each model in Table 4-1. Typically, a model with finer mesh has more elements and number of nodes. This will lead to smaller element sizes and better approximation. However, the fact that more nodes are to be analyzed means more computer resources are to be used; and longer time to be expected to finish modeling. Only appropriate mesh density was used to finish each running in this research. For example, Figure 4-5 shows passive force versus displacement for coarse mesh, medium mesh and fine mesh in 0° skew test. Peak passive force dropped from 470 kips to 454 kips from coarse mesh to medium mesh, which is 3.4% decrease; while peak passive force for the medium and fine meshes were almost the same. Although finer mesh provides somewhat more accurate results, fine mesh model took significantly longer time to run than the medium mesh model. Thus medium mesh was used for 0° skew model.

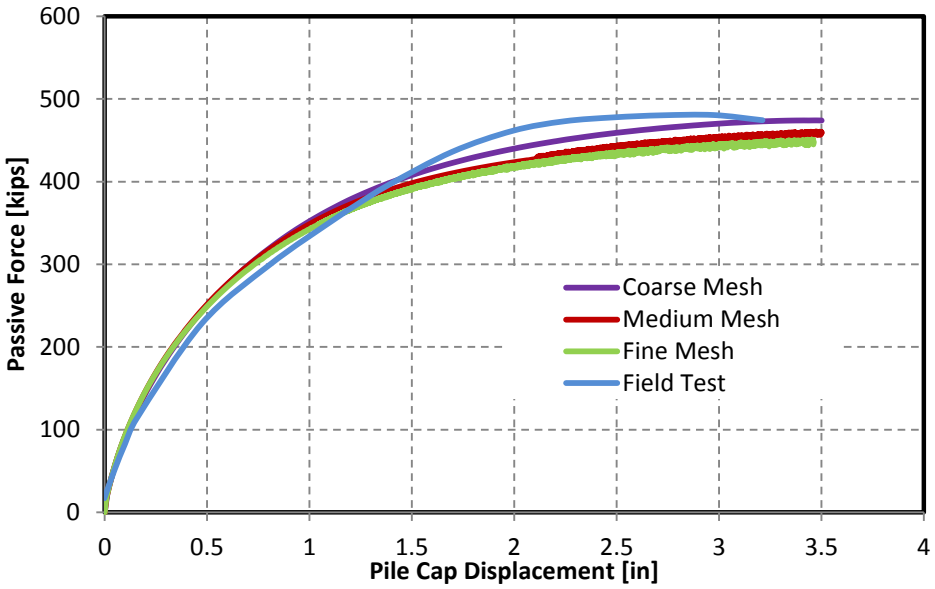

Figure 4-5: Mesh Density Affects Final Peak Passive Force

For the 0°, 15° and 45° skew models medium setting was used to create the mesh; however, for the 30° skew mode a fine mesh setting was necessary to achieve an appropriate mesh density. Generally, as the skew angle increased, the numbers of nodes, soil elements and stress points increase and at the same time, the average element size decreases.

In Plaxis 3D, fineness factor/ratio was used to describe the shape of individual elements. Specifically, it is the ratio of the length of an element to its maximum width. Short and fat element has a low fineness factor; Long and skinny element has a high fineness factor. Typically, an element with equal length of each side is deemed to be a good element for simple structure like this.

The minimum and maximum quality value for fineness factor is listed in Table 4-1. Fineness factor values in the range from 0.0625 to 8.0 are considered acceptable. (PLAXIS 3D-2015).

Table 4-1: Summary of Nodes, Elements, and Quality Values for the Four Numerical Models

Model	*Elements*	*Number of Nodes*	*Number of Soil Elements*	*Avg. Elem. Size (ft)*	*Quality Minimum Value*	*Quality Maximum Value*	*Mesh Method*
0	10 noded	18741	12366	1.303	0.4801	0.9988	Automatic
15	10 noded	19986	13025	1.27	0.3654	0.9998	Automatic
30	10 noded	28964	19591	1.035	0.2502	0.9993	Automatic
45	10 noded	30015	19850	1.029	0.06846	0.9986	Automatic

Boundary conditions for each of the four models were very similar, with the backfill zone extending approximately 25 feet to 30 feet (7.62 meters 9.14 meters) from the face of the backwall, 10 feet to 15 feet (3.05 meters to 4.57 meters) from the edges of the backwall, and 14.5 feet (4.42 meters) below the bottom of the backwall.

Though groundwater in the field existed approximately 2 feet below the base of the pile cap, in order to simplify model conditions, groundwater was not included in the numerical models. Because the shear zone did not extend below the ground water level, this simplification is not expected to have had any significant effect.

Boundary condition on the external margins on the sides of the soil backfill is fixed in x and y direction, and free in z direction. However, nodes on the base of the model are fixed in all directions.

The pile cap was modeled as a plate element with stiffness properties shown in Table 4-2. These properties made the pile cap essentially rigid in comparison with the surrounding soil.

Boundary condition for the pile cap is fixed in the z direction and free in the y direction and prescribed displacement in the x direction.

To simplify the analysis, the piles below the pile cap were not modeled explicitly with actual physical piles. Instead, the vertical restraint produced by the piles was modeled by applying a boundary condition to the pile cap which restricted vertical movement to be zero.

Model boundaries were sufficient to not influence the results. This conclusion was investigated by running other models with dimension of 60 feet by 60 feet by 20 feet, with the same material and load settings. Plaxis 3D produced the same load-deflection curves and other final results with the same skew angle. Therefore, models with dimension of 40 feet by 35 feet by 15 feet were sufficient to run in order to reduce the memory used and running time.

Table 4-2: Plate Element Properties for Pile Cap

Property	*Value*	*Units*
Plate Thickness, d	15	ft
Unit Weight, γ	150	lbf/ft^3
Young's Modulus, E	635.8E6	lbf/ft^2
Poisson's Ratio, ν	0.30	–
Shear Modulus, G	264.9E6	lbf/ft^2

Interface elements with positive and negative planes need to be added when the model is set up, in order to simulate the interaction between the structure and the soil. Without interface elements, the pile cap would be tied to the soil preventing relative movement between two materials as shown in Figure 4-6.

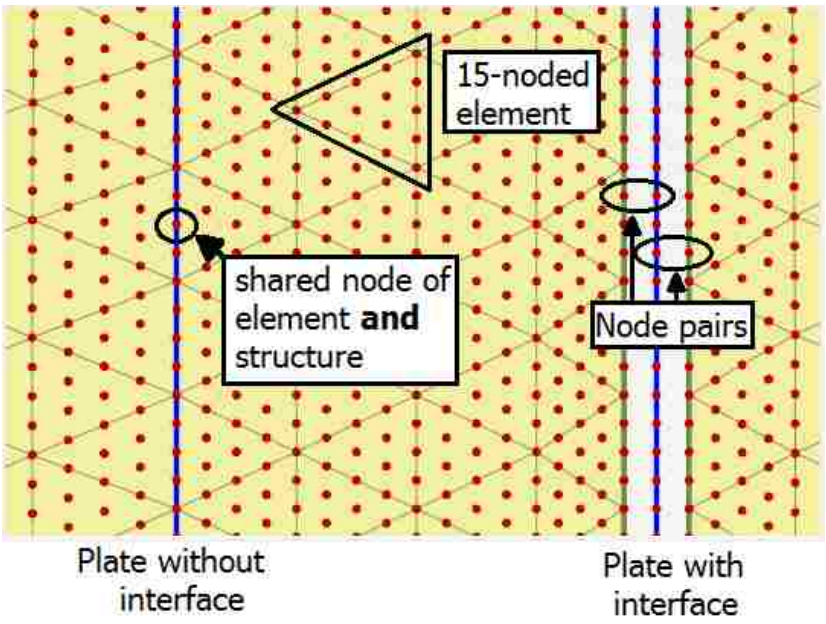

Figure 4-6: Example of Plate (15 nodes) with or without Interface Element Extension Plates (Plaxis 3D Reference Manual PLAXIS 3D-2015)

Similar to Plaxis 2D, interface plates should also be placed where acute angles are formed between the structure and the soil. Without interface plates, a singularity forms producing oscillating stress distributions around structure corner points and providing unrealistic results, as shown in Figure 4-7 a.

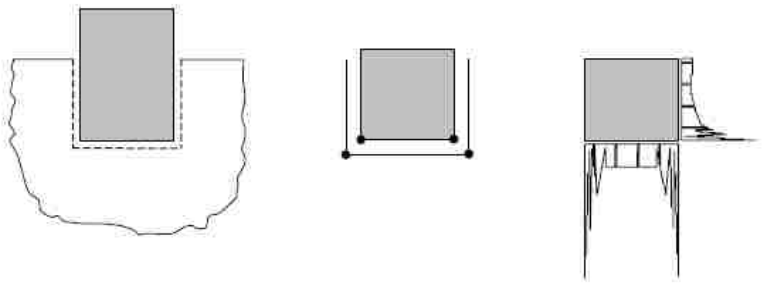

(a) Oscillating stress distributions occur around structure corner points

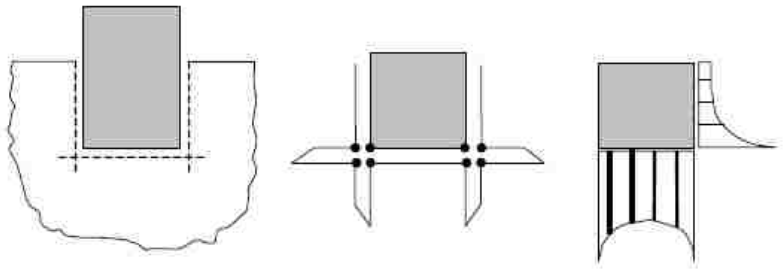

(b) Enhanced stress results using interface element extension plates

Figure 4-7: Corners of a Stiff Structure with: (a)Oscillating Stress Distributions; and (b) Enhanced Stress Results (PLAXIS 3D-2015Reference Manual)

Plaxis recommends extending the interface element plates beyond the edges of the pile cap into the backfill soil. Any reasonable length will work for the model since the material strength properties for the interface were set to be the same as the surrounding soils.

Length values of one foot, two feet and five feet were tested in the Plaxis 3D models, and model results are almost identical. A length of one foot was chosen herein for the extension plates' length. An interface element extension plate is merely a tool to generate feasible models without the formation of singularities. The material properties should be the same as ones of the surrounding soil backfill.

The other type of interface plane identifies boundary condition between the backwall and backfill soil, which should be separated from the first type of the interface plane.

In Plaxis 3D, the strength reduction factor is used to relate the wall friction and adhesion to the soil cohesion and internal friction angle. This parameter is defined by the following equation (4-1):

$$R_{inter} = \frac{tan\delta}{tan\phi} \qquad (4\text{-}1)$$

Where δ is the wall/interface friction angle, and ϕ is the soil friction angle.

The first type of the interface plane which separates relative movement between two soil volumes should have the strength reduction factor with a value of one, since the plane and the surrounding soil have common properties; whereas the second type should use equation (4-1) above to solve for the reduction factors.

An illustration showing the locations of the interface planes is presented for the 0 skew test in Figure 4-8. Interface element plates with positive and negative interfaces were placed where the adjacent soil volumes have large relative movement values.

As shown in the Figure 4-8, planes with a brown color represent positive and negative interfaces; whereas planes with a gray color represent interface element plates. Planes with blue color represents interfaces between soil and back wall. Because the pile cap is moving in the X direction, element plates along two vertical sides and bottom end were generated. On the bottom end, along the pile cap surface, another interface element plate was generated to account for the vertical movement of the pile cap.

Backfill materials were modeled using the Hardening soil model. Initial soil strength and stiffness parameters were obtained using an optimization routine built for PYCAP (Mokwa and Duncan 2001) by Franke (2013). These optimized parameters are shown in Table 4-3.

However, in order to get the best agreement between field and numerical results, input Hardening Soil model parameters were modified to those shown in Table 4-4. Many of the properties remained essentially the same; however, the Young's modulus changed significantly in order to model the behavior of the pile cap in the field. This difference is largely due to the definitions of the stiffness in PYCAP and PLAXIS. For example, PYCAP uses the initial tangent stiffness while PLAXIS uses the secant stiffness at 50% of the strength.

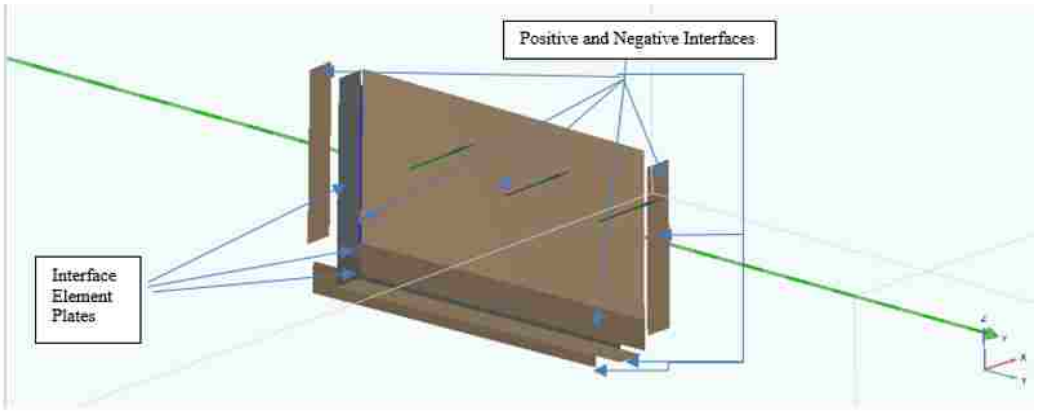

(a) 3 Dimensional View 1

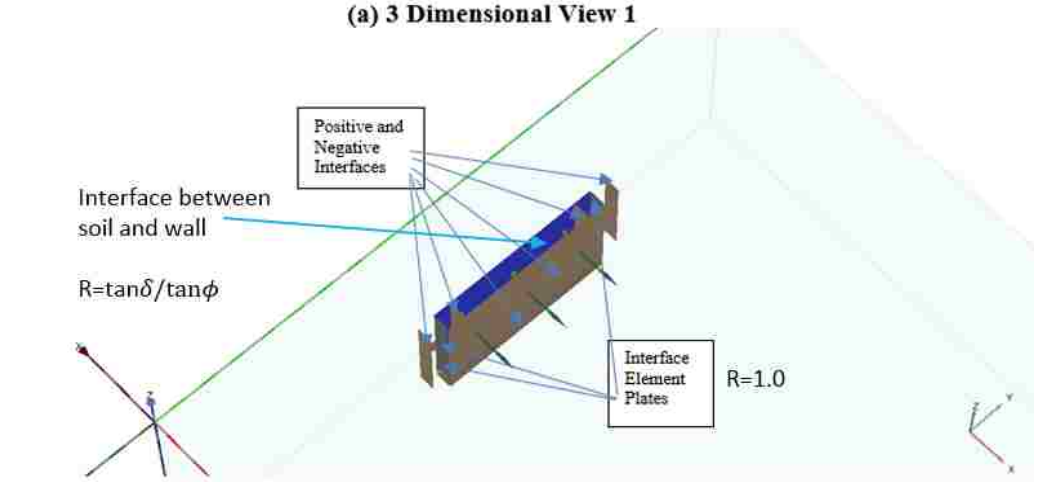

(b) 3 Dimensional View 2

Figure 4-8: Interface Element Plates with Positive and Negative Interfaces

Table 4-3: Optimized PYCAP Soil Strength and Stiffness Parameters

Property	*Value*	*Units*
Young's Modulus, E	415	kip/ft^2
Soil Friction Angle, ϕ	40	Degrees
Wall Friction Angle, δ	28	Degrees
Cohesion, c	85	lbf/ft^2
Poisson's Ratio, ν	0.2	N/A
Soil Unit Weight, γ	117	pcf
Adhesion Factor,α	1	
Dmax/H	0.032	-

In Table 4-4, the cohesion and angle of internal friction were determined from field and laboratory measurements along with back-calculated values from the spreadsheet program PYCAP. The drained cohesion was found to be 85 lb/ft^2 primarily due to matric suction in the partially saturated soil

Soil friction angle was first assigned a value of 40° based primarily on the in-situ direct shear testing and the back-calculated PYCAP analyses. Using this value for soil friction angle, other hardening soil model parameters were calibrated to match the measured load-deflection curve for the field test with 0° skew., Once a generic model was generated, the same parameters were used to analyze the behavior of the pile caps with skew angles of 15°, 30° and 45° to help understanding the effects of varying skew angle. Subsequently, parametric studies were conducted to better understand the effect of various parameters in the Strain Hardening Model on the computed passive force-deflection curves as presented in Section 5.2.

For a soil friction angle of 40°, the best agreement with the measured passive force-deflection curve was obtained with wall friction angle of 30°. A value of 28° was first obtained from the PYCAP program a. However, using this value, Plaxis 3D produced slightly smaller passive force values at large displacements than the measured curve. Better agreement was obtained with a wall friction of 30° which represents a δ/ϕ value of 0.75 which is typical of sand-concrete interfaces.

The wall friction is introduced in PLAXIS 3D using an interface friction ratio, R_{inter} given by the equation (4-1). Therefore, R_{inter} was set at 0.6881.

Angle of dilatancy, ψ, defines the tendency for the sand to dilate during shearing. This parameter was not accounted in PYCAP so it had to be estimated using other guidelines.

The angle of dilatancy in this study was estimated using the following equation.

$$\psi = \phi - a \tag{4-2}$$

Where

ϕ =Soil Friction Angle

a =Degrees within the range from 25° to 35°, but is typically about 30°

In this test, 25° was used.

Unsaturated unit weight and saturated unit weight were obtained from the field measurement.

Stiffness values were obtained from calibration of the models in order to match the initial slope of the passive force-displacement curve. It is worth noticing that the ultimate unloading/ reloading stiffness is 12 times bigger than initial soil stiffness which was achieved from PYCAP.

Parameters, such as power m, Poisson's ratio $\nu_{ur,}$ reference stress p^{ref}, K_0^{nc}, failure ratio R_f, tensile strength $\sigma_{tension}$, Incremental increase c_{inc}, compression index C_c, swelling index C_s etc., were used as default values built into Plaxis 3D.

Initial void ratio, $e_{initial}$, was obtained from a lab test with the soil sample on site

In conclusion, some parameters were obtained from the field test; some parameters were calibrated from the finite element models comparing to the field tests; some parameters were default values in Plaxis 3D.

Table 4-4: Plaxis Model Parameters for Hardening Soil Model

	Symbol	*Parameter*	*Value*	*Default Units*
		Failure parameters (same as for Mohr-Coulomb model)		
	c	(Effective) cohesion	85	[lb/ft^2]
	ϕ	(Effective) angle of internal friction	40	[°]
	δ	Wall friction angle	30	[°]
	ψ	Angle of dilatancy	15	[°]
	R_{inter}	Interface Friction Ratio	0.6881	
		Basic soil stiffness parameters		
	γ_{unsat}	Unsaturated Unit Weight	116.5	[lb/ft^3]
	γ_{sat}	Saturated Unit Weight	120	[lb/ft^3]
	E_{50}^{ref}	Secant stiffness in standard drained triaxial test	1.920E6	[lb/ft^2]
	E_{oed}^{ref}	Tangent stiffness for primary oedometer loading	1.920E6	[lb/ft^2]
	E_{ur}^{ref}	Unloading/reloading stiffness (default $E_{ur}^{ref} = 3E_{50}^{ref}$)	4.800E6	[lb/ft^2]
	m	Power for stress-level dependency of stiffness	0.5	[-]
		Advanced parameters		
A	ν_{ur}	Poisson's ratio for unloading-reloading (default $\nu_{ur} = 0.2$)	0.2	[-]
	p^{ref}	Reference stress for stiffness (default $p^{ref} = 100$ kN/m^2)	2089	[lb/ft^2]
	K_0^{nc}	K_0-value for normal consolidation (default $K_0^{nc} = 1 - sin\phi$)	0.3601	[-]
	R_f	Failure ratio q_f/q_a (default $R_f = 0.9$)	0.9	[-]
	σ_{tensio}	Tensile strength (default $\sigma_{tension} = 0$ stress units)	0	[lb/ft^2]
	c_{inc}	Incremental increase in cohesion with depth (default $c_{inc} = 0$)	0	[lb/ft^2]
		Alternative soil stiffness parameters		
	C_c	Compression index	3.865E-3	[-]
	C_s	Swelling index or reloading index	1.392E-3	[-]
	e_{init}	Initial void ratio	0.5450	[-]

4.4 Finite Element Analysis

To carry out the finite element analysis using Plaxis 3D, the following steps were followed:

1) A structural model (outer boundary limits) was generated in the Plaxis input program. Material properties and boundary conditions were assigned to the model.
2) A medium or fine density finite element mesh was generated which depends on the density of the elements and the shape of the structure. The basic soil element for the 3D finite element mesh is the 10-node tetrahedral element shown in Figure 4-9.(PLAXIS 3D-2015)

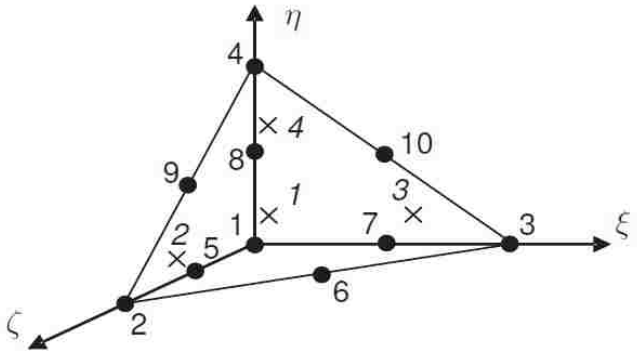

Figure 4-9: Typical 3D Soil Element (10-Node Tetrahedrons) Used in the Model (PLAXIS 3D-2015)

3) Gaussian stress points were selected along the pile cap to obtain the relationship between longitudinal force and prescribed displacement in the Plaxis Output Program. Because the wall was essentially rigid, all points on the pile cap moved the same amount.
4) The analysis was performed by defining an initial phase first which applies all material settings and model dimensional settings into a constitutive model and starts the

calculation. The program then follows a single operating phase where the prescribed boundary conditions, including movement direction, velocity, maximum displacement value, stress on the objects and etc., were activated. In this case, a maximum of 3.5 inches total displacement in x direction was applied for all different skew angle models. After the analysis procedure was completed, the load-displacement curves could be accessed by choosing the Gaussian stress points in the Plaxis output program. In addition, selected results such as pressure distribution and displacement contours could be plotted with the Plaxis Output program.

5 RESULTS AND DISCUSSION

5.1 Numerical Simulation

The computer model was initially calibrated with the field results for the 0° skew test. To obtain agreement between the measured and computed results, only small variations in the friction angle and wall friction were necessary; however, the stiffness of the soil had to be adjusted considerably. After the calibration of the numerical model for the 0° skew test, the same parameters were employed for all of the subsequent analyses of the other skew angle models. In this section, the field test results and numerical simulation results will be presented and discussed.

5.1.1 Passive Force versus Deflection Curves

A plot of the computed passive force versus deflection curve for the 0° skew case is provided in Figure 5-1 in comparison with the measured curve from the field test. For a Plaxis 3D finite element model, computed passive forces within about a 10 percent of the measured passive force from the field tests is considered acceptable accuracy. For the zero skew test, the computed passive force was typically within a few percent of the measured force until a deflection of about 1.5 inches. At higher deflections, there is some divergence between measured and computed resistance. The field test reached a maximum value at around 3 inches yielding a maximum passive

force of 480 kips. The Plaxis 3D program computed a maximum passive force of 450 kips which is only 6% less than the field test. However, the computer model predicted a more gradual increase in the force with a peak at 3.5 inches while the measured force peaked at 3 inches.

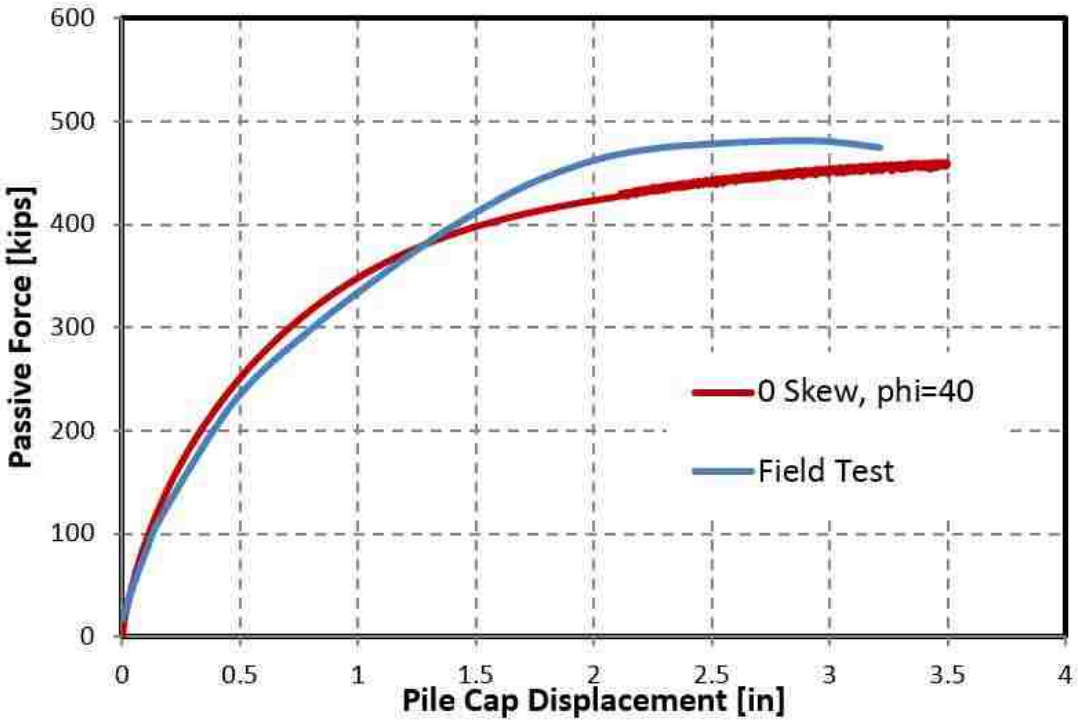

Figure 5-1: Measured and Computed Passive Force- Deflection Curves for 0 Skew test

A plot of the computed passive force versus deflection curve for the 15° skew case is provided in Figure 5-2 in comparison with the measured curve from the field test. For the 15 skew, field test, the agreement between measured and computed force is within 10% up to a deflection of about 2 inches. However, the measured passive force peaked at around 2 inches yielding a maximum passive force of 350 kips and then decreases. In contrast, the Plaxis 3D program predicted a continued increase in passive force beyond a deflection of 2 inches with a peak passive force of 385 kips which is about 10% more than the field test results. The discrepancy between the

measured and computed resistance after 2 inches is likely a result of the higher density for the backfill for the 15° skew test relative to the 0° skew test. The higher density backfill soil tends to dilate and experience a reduction in resistance after reaching the peak. However, the computer model is based on the density of the 0° skew test and exhibits a hyperbolic shape without a reduction in the resistance after the peak.

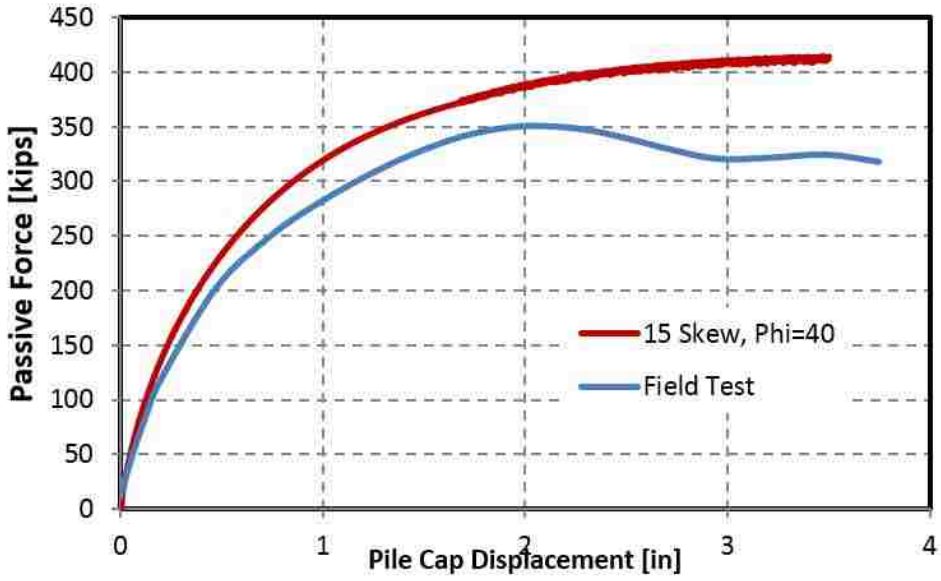

Figure 5-2: Measured and Computed Skew Passive Force- Deflection Curves for 15° Skew Test

A plot of the computed passive force versus deflection curve for the 30° skew case is provided in Figure 5-3 in comparison with the measured curve from the field test. For deflections less than 1.5 inches, the computed passive force is 10 to 20% higher than the measured curve. However, at higher deflections the agreement improves somewhat. The measured passive force from the field test reaches a peak at around 2 inches yielding a maximum passive force of 279 kips. The Plaxis 3D program computed a peak passive force of 261 kips which is 6.9% less than

the field test. Nevertheless, the computed response seems to reflect the average curve obtained from the field testing.

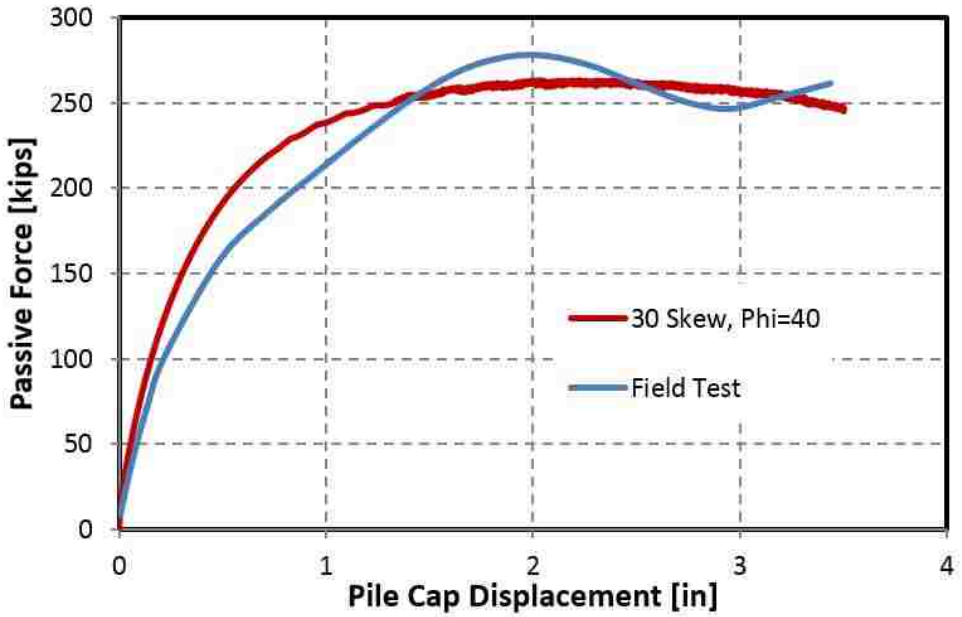

Figure 5-3: Measured and Computed Passive Force-Deflection Curves for the 30° Skew Test.

A plot of the computed passive force versus deflection curve for the 45° skew case is provided in Figure 5-4 in comparison with the measured curve from the field test. For the 45° skew test, the measured passive force has a hyperbolic curve shape which reaches a maximum value of 171 kips at 3 inches of displacement. In contrast, the passive force computed by Plaxis 3D peaks at a displacement of about 1 inch with a value of 100 kips and then slowly decreases to a value of 70 kips as the pile cap displaces further into the backfill. This discrepancy occurs because the computer model is unrestrained in the transverse direction and the shear force at the pile cap-backfill interface exceeds the shear resistance on this interface. As a result, the pile cap in the computer model slides several inches in the transverse direction and cannot mobilize additional

passive force. In the field test, however, piles are located under the pile cap which provide additional shear resistance after the soil fails and allow the passive force to increase to the maximum level.

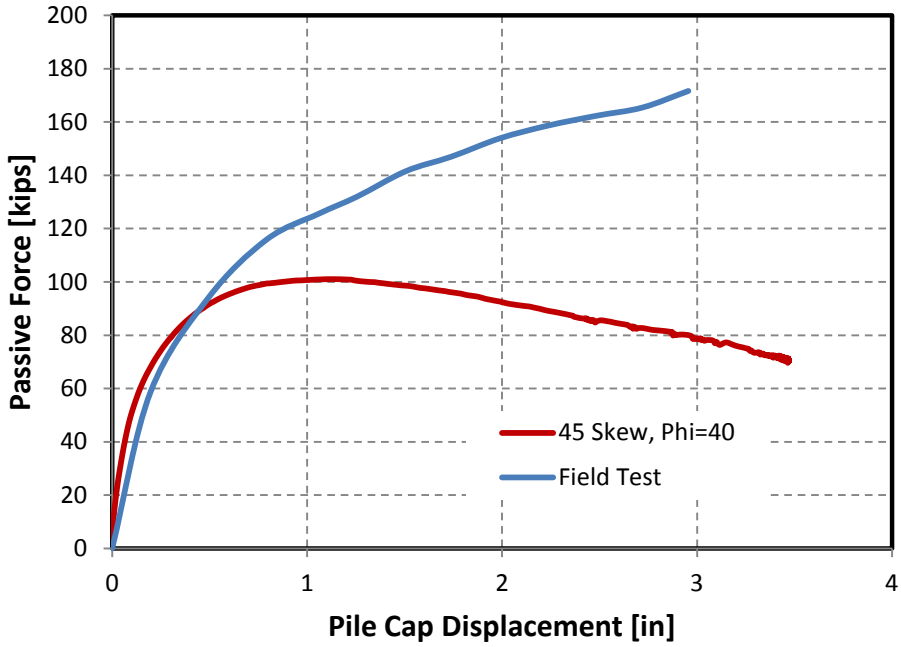

Figure 5-4: Measured and Computed Passive Force-Deflection Curves for the 45° Skew Test

5.1.2 45 Degree Set Sliding Failure

Additional understanding regarding the issue which was mentioned in the previous section can be obtained by examining the distribution of forces at the interface between a skewed bridge and the adjacent backfill soil as illustrated in Figure 5-5 as originally outlined by Burke (1994).

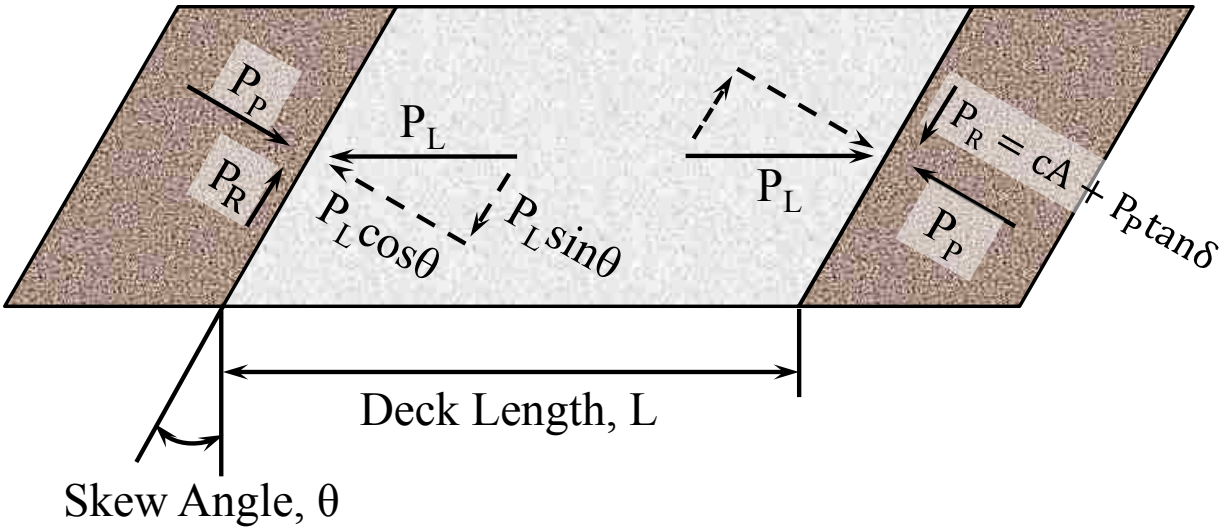

Figure 5-5: Distribution of Forces at the Interface between a Skewed Bridge and the Adjacent Backfill Soil by Burke (1994)

The longitudinal force (P_L) can be induced by thermal expansion or seismic forces. The components of the longitudinal force normal and transverse to the abutment must be resisted by the passive force (P_p) normal to the abutment backwall and the shear resistance (P_R) on the backwall. Summing forces normal to the abutment produces the equation

$$P_p = P_L\cos\theta \tag{5-1}$$

Where θ is the skew angle of the backwall.

The transverse applied shear force (P_T) can be computed using the equation

$$P_T = P_L\sin\theta \tag{5-2}$$

While the transverse shear resistance (P_R) can be given by the following equation (next page):

$$P_R = cA + P_p\tan\delta \tag{5-3}$$

Where c is the soil cohesion, A is the area of the backwall, and δ is the angle of wall friction between the backfill soil and the concrete abutment backwall.

Summing forces transverse to the backwall produces the equation

$$(cA + P_p \tan\delta)/F_s \geq P_L \sin\theta \qquad (5\text{-}4)$$

Where F_s is a factor of safety. If the applied transverse shear force exceeds the ultimate shear resistance, the abutment could slide against the soil leading to an unstable condition.

A plot of the longitudinal force, passive force, applied shear force and shear resistance as a function of skew angle is provided in Figure 5-6. In this case the friction angle (ϕ) was 40°, the cohesion was 85 psf, and the interface friction angle (δ) was 75% of the soil friction angle or 30° based on results field and laboratory testing. As the skew angle increases the applied shear force increases despite the fact that both the longitudinal and passive force decrease. In addition, the shear resistance decreases as skew angle increases. At a skew angle of about 30° the shear force is approximately equal to the applied shear resistance and the system remains stable. However, at a skew angle of 45° the applied shear force exceeds the shear resistance and the wall would be expected to slide in the transverse direction as predicted by the computer model. However, in the field case, the piles underneath the pile cap provide additional transverse shear force to prevent excessive movement.

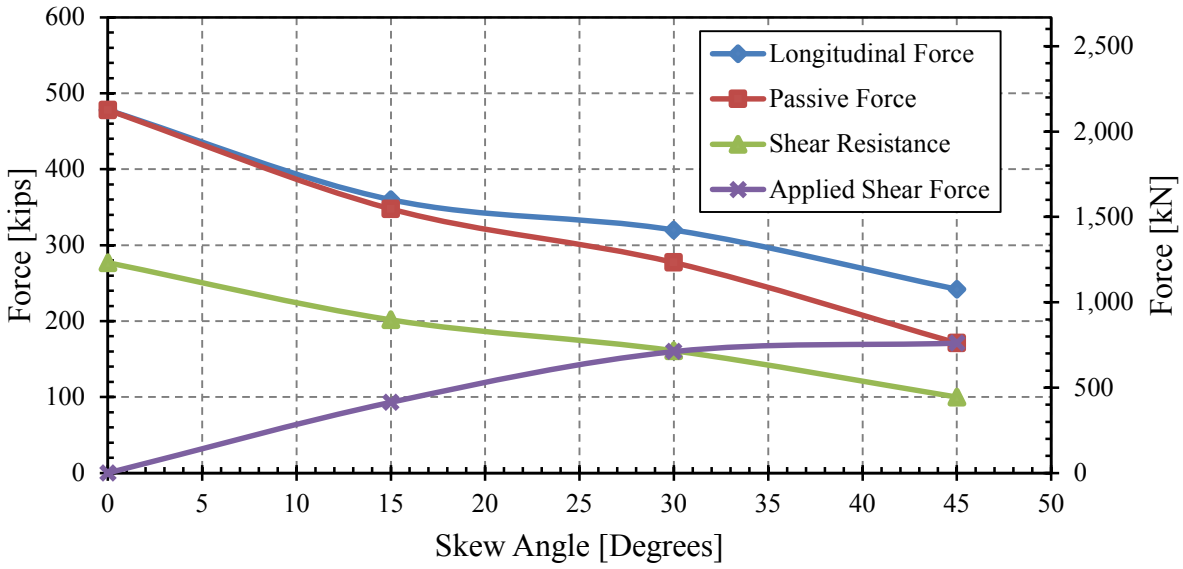

Figure 5-6: Comparison of Peak Passive Force, Longitudinal Force, Shear Strength, and Applied Shear Force with respect to Skew Angle

For the 45° skew configuration, the pile cap wall was computed to displace laterally in the same plane as the backwall of the pile cap with a deflection of 5.54 inches and the soil adjacent to the acute side of the cap began to fail as shown in Figure 5-7. In the field test, the lateral displacement was not as great as computed by the model because the six piles under the pile cap likely provided the additional resisting force to prevent lateral movement. Because the pile cap was only source to drive the increasing value of the passive force in the Plaxis 3D model, without the proper restraint in traverse direction (Y direction), the pile cap will likely slip to the acute corner. This was verified by the calculation mentioned above: that is, the total slip distance of the pile cap is 5.54 inches as shown in Figure 5-7. The effect of completely restrict y directional movement will be presented in Section 5.2.5.

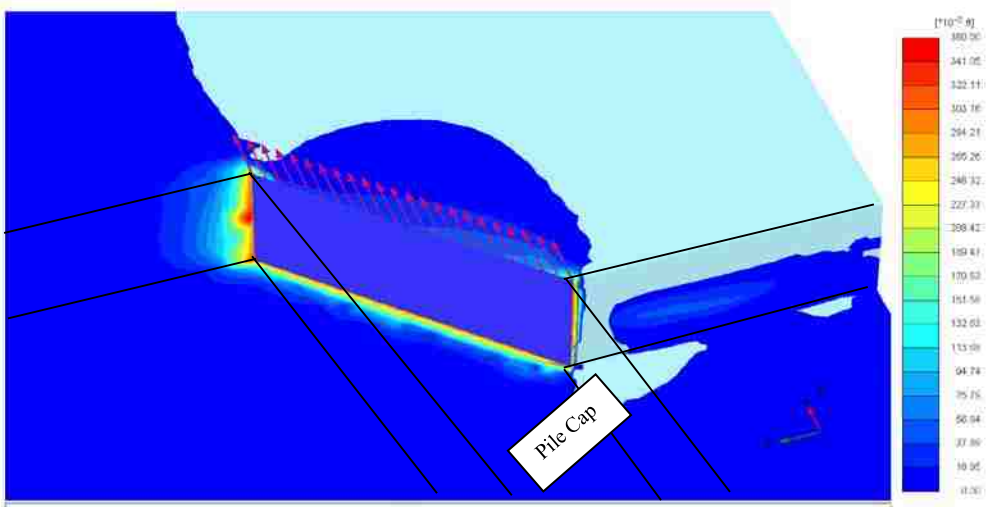

Figure 5-7: Pile Cap Slipped into Soil Backfill for 45° Skew Configuration

Since the different behavior between the field test and computer model, results from 45 skew set will be omitted.

5.1.3 Reduction Factor for Skew Effects

In order to determine the relationship between the skew angle and peak passive force, the concept of a reduction factor was applied as discussed background section of this thesis (1.1). Rollins and Jessee (2013) proposed that the reduction factor to account for skew effects on passive force be computed using equation (1-1). To determine the reduction factor based on the result of this study, the peak passive forces were normalized against peak passive force for the 0° skew test by using the following equation:

.

$$R_{skew} = \frac{P_{P-skew}}{P_{P-no\ skew}} \qquad (5\text{-}5)$$

Where

θ= Skew angle

$P_{P\text{-}skew}$= Peak passive force for a skewed abutment

$P_{P\text{-}no\ skew}$= Peak passive force for a non-skewed abutment

Figure 5-8 shows reduction factor curve versus skew angle using the data published by Rollins and Jessee (2013), and numerical model results obtained by Shamsabadi et al. (2007). Numerical results from this test using Plaxis 3D were also included to compare with other tests. The equation for R_{skew} shown in this figure was derived using the lab test results.

For the 15° skew field test and Plaxis 3D model, peak passive force was found to be 73% and 86%, respectively, of the peak passive force for the 0° skew test. For the 30° skew test, field test and Plaxis 3D model have the same correction factor, which is 58%. The value is close to predicted value by using equation for $R_{skew,}$ which is approximately 52%. This shows the good quality of the Plaxis 3D model set up.

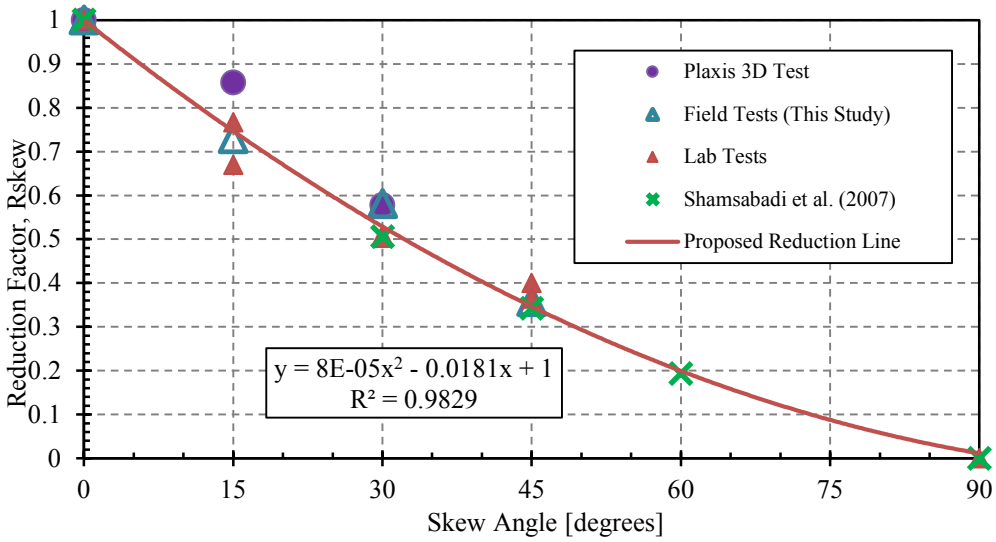

Figure 5-8: Comparison of Correction Factor among Plaxis 3D, Field Test(Rollins and Marsh 2013, Rollins and Smith 2014, Lab Tests (Rollins and Jessee 2013) and Shamsabadi et al. (2007)

5.1.4 Total Deflected Shape, Heave Pattern and Total Displacements

At the end of the calculation step for 3.5 inches of longitudinal displacement, the total displacement and displacement in the x, y and z directions was recorded. The maximum total and longitudinal displacements modeled by Plaxis 3D for the backfill soil are listed in Table 5-1 below.

Table 5-1: Maximum Total Displacements Modeled by Plaxis 3D

Skewness	*Total Displacement*		Longitudinal Displacement	
degree	*inches*	*(mm)*	*inches*	*(mm)*
0	4.4928	114	3.5	88.9
15	4.3704	111	3.5	88.9
30	6.7584	172	3.5	88.9
45	38.868	987	3.5	88.9

The total displacement contains x, y, and z components and these directions were identified in Figure 5-9. A uniformly distributed prescribed displacement with a magnitude of 3.5 inches in the x-direction was placed on the front face of the pile cap as indicate by dark blue color in Figure 5-9. This displacement caused passive pressure to develop on the pile cap, and the heave pattern of the soil behind the pile cap to develop. The heave pattern is relatively symmetric for the zero skew case but becomes more asymmetric as the skew angle increases as shown in Figure 5-9 a-d. The greatest displacement and heave appears to be concentrated in the backfill near the acute corner of the abutment wall. Very little heave occurs for the 45° case because the abutment primarily slides along the skewed abutment rather than deforming the backfill soil.

.

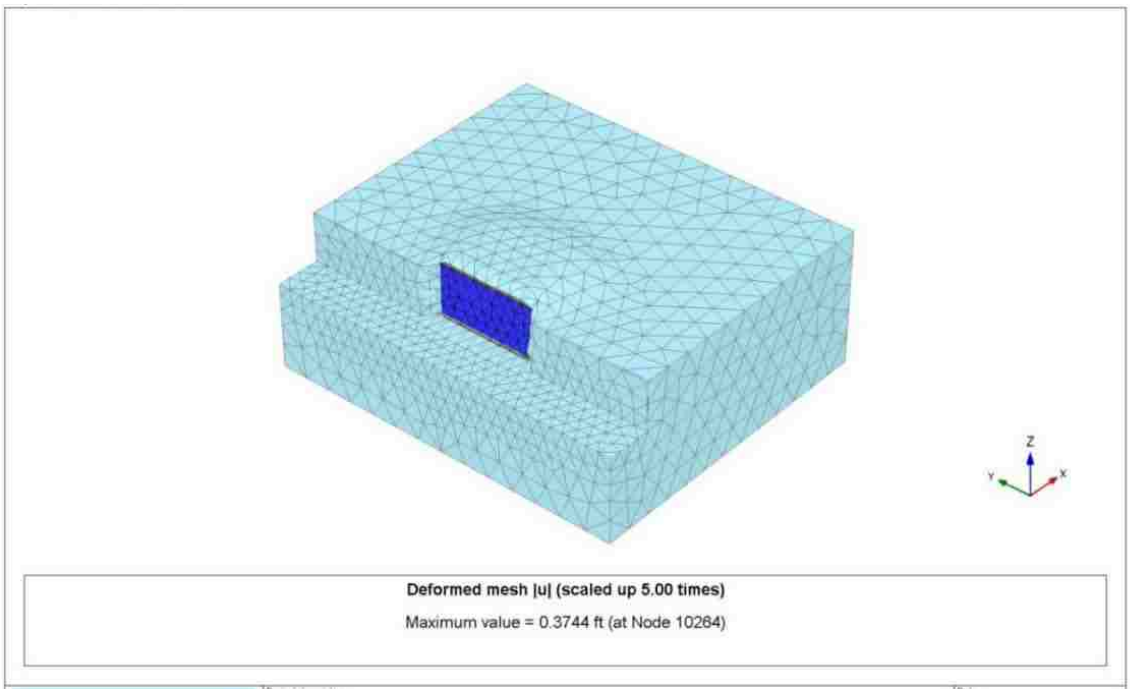

(a) 0° skew pile cap with homogenous compacted sand backfill

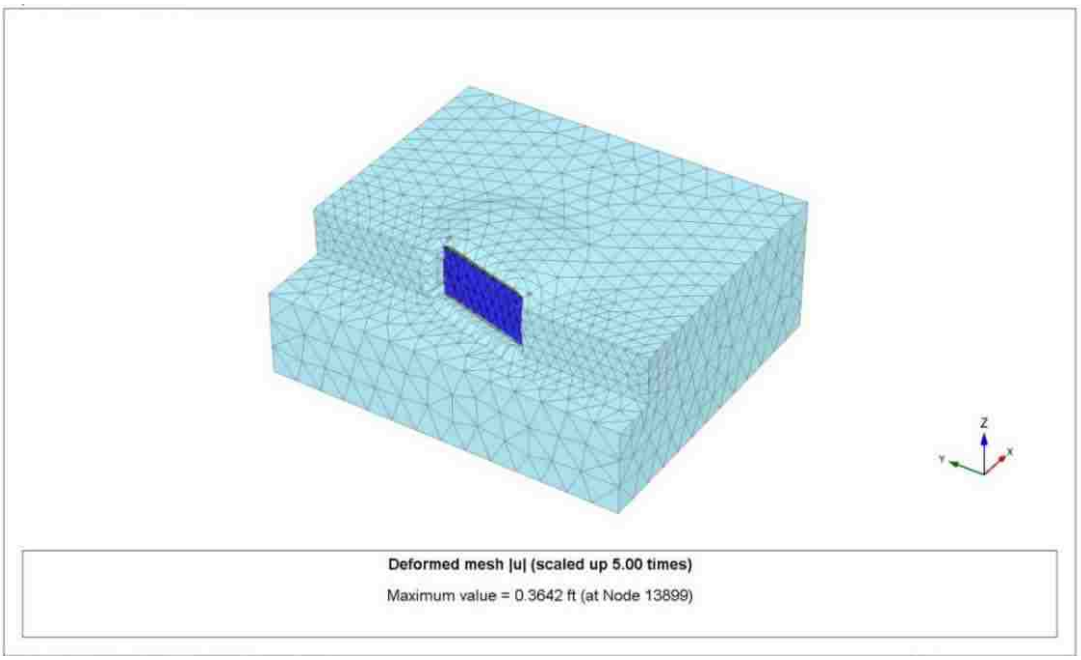

(b) 15° skew pile cap with homogenous compacted sand backfill

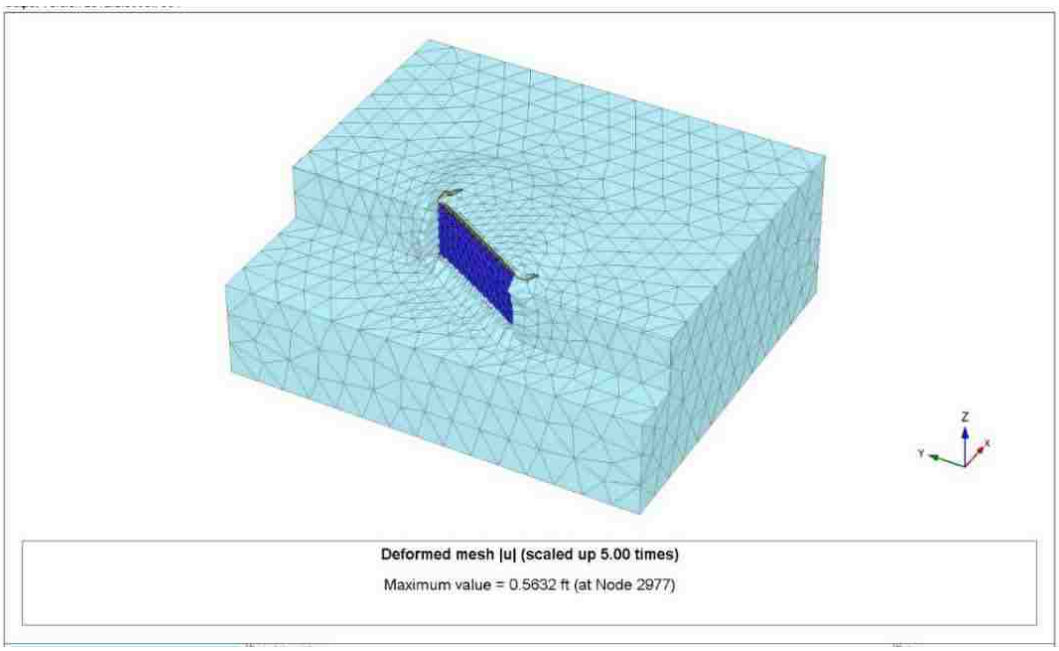

(c) 30° skew pile cap with homogenous compacted sand backfill

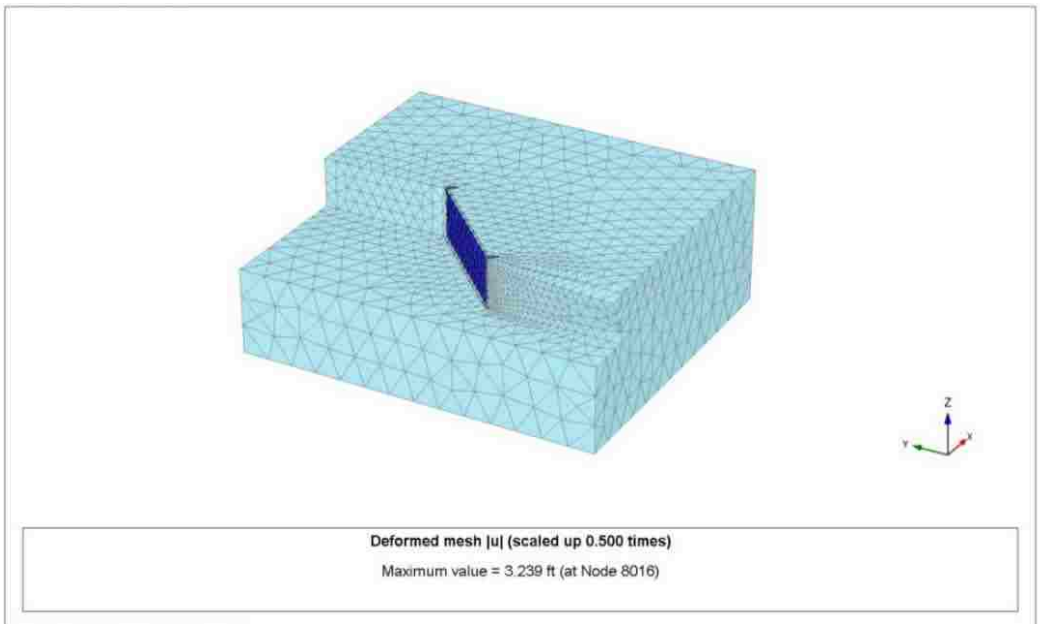

(d) 45° skew pile cap with homogenous compacted sand backfill

Figure 5-9: Vertical Displacement (Heave) Pattern for (a) 0 °,(b) 15 °,(c) 30 °,(d) and 45 ° Skew Models

Figure 5-10, Figure 5-11, Figure 5-12, and Figure 5-13 compare measured and computed heave results for the 0°, 15°, 30°, and 45° skew tests. For each figure the top plot shows a plan view of measured backfill heave contours and surface cracks while a plan view of heave contours computed by Plaxis 3D is shown in the companion bottom figures.

In Figure 5-10, showing the 0° skew case, both the top and bottom figures exhibited similar maximum heave patterns at the corner of the backwall with somewhat lower heave near the center of the backwall. This pattern is consistent with previous research which indicates that the highest passive pressures on a wall face occurs at the edges of the wall (Borowicka 1938; Cummins 2009). The heave contours for both the measured and computed cases are symmetric about the longitudinal centerline.

The semi-elliptical heave bulbs extend 22 feet into the soil backfill for both measured and computed results. In contrast, the computer model shows an approximately 25-feet wide heave zone in the transverse direction. However, the heave zone measured in the field was only 22 feet wide likely due to the backfill boundary limitation. The field test has a more irregular outer boundary due to complexity of the site conditions but overall the computed results show very good agreement with the measured results.

Maximum heaves for the field test and computer model were approximately 2 inches and 3 inches, respectively. These values equal to 3% and 4.5% of the backfill height. This phenomenon is due to complexity of the backfill and mesh density in Plaxis 3D program.

In Figure 5.11, showing the 15° skew case, both the top and bottom figures show similar heave patterns with the maximum heave located near the acute corner. In contrast to the 0° skew

test, the heave contours were not symmetric but were somewhat higher on the acute side of the pile cap.

The semi-elliptical heave bulbs extend 19 feet into the soil backfill in longitudinal direction from the tip of the acute corner for both measured and computed results. Heave zone width in the transverse direction was measured to be 22 feet and 24 feet for the field test and the computer model, respectively. Compared to the computer model, the field test has more irregular outer boundary due to complexity of the site conditions.

Maximum heave for the field test and computer model was approximately 3 inches and 3.17 inches, respectively which is within about 5.6% of error. These values are approximately equal to 4.5% of the backfill height. Overall, the 15° computer model provides very good agreement with the field test in terms of heave and the error is typically from 0% to 9%.

In Figure 5.12, which shows the 30° skew test, the maximum heave occurred in a small zone approximately 4 feet to the north of the acute corner of the backwall for both measured and computed tests. A similar trend was seen for the 15° degree test as well which shows a different failure mechanism relative to the 0° test. In addition, the overall shapes of the measured and computed heave contours are very similar

The semi-elliptical heave bulbs extend 15 feet into the soil backfill in the longitudinal direction from the tip of the acute corner for both measured and computed results. The width in the transverse direction was measured to be 22 feet for both the field test and the computer model. Compared to other tests, the 30° field test has a smoother outer boundary and better matches with the computer model.

Maximum heave for the field test and computer model was approximately 2.2 inches and 2.94 inches, respectively. These values are approximately equal to 3.3% and 4.5% of the backfill height.

Overall, the 30° computer model exhibits the best agreement among the three tests in terms of heave results error ranging from 0% to 3.4%.

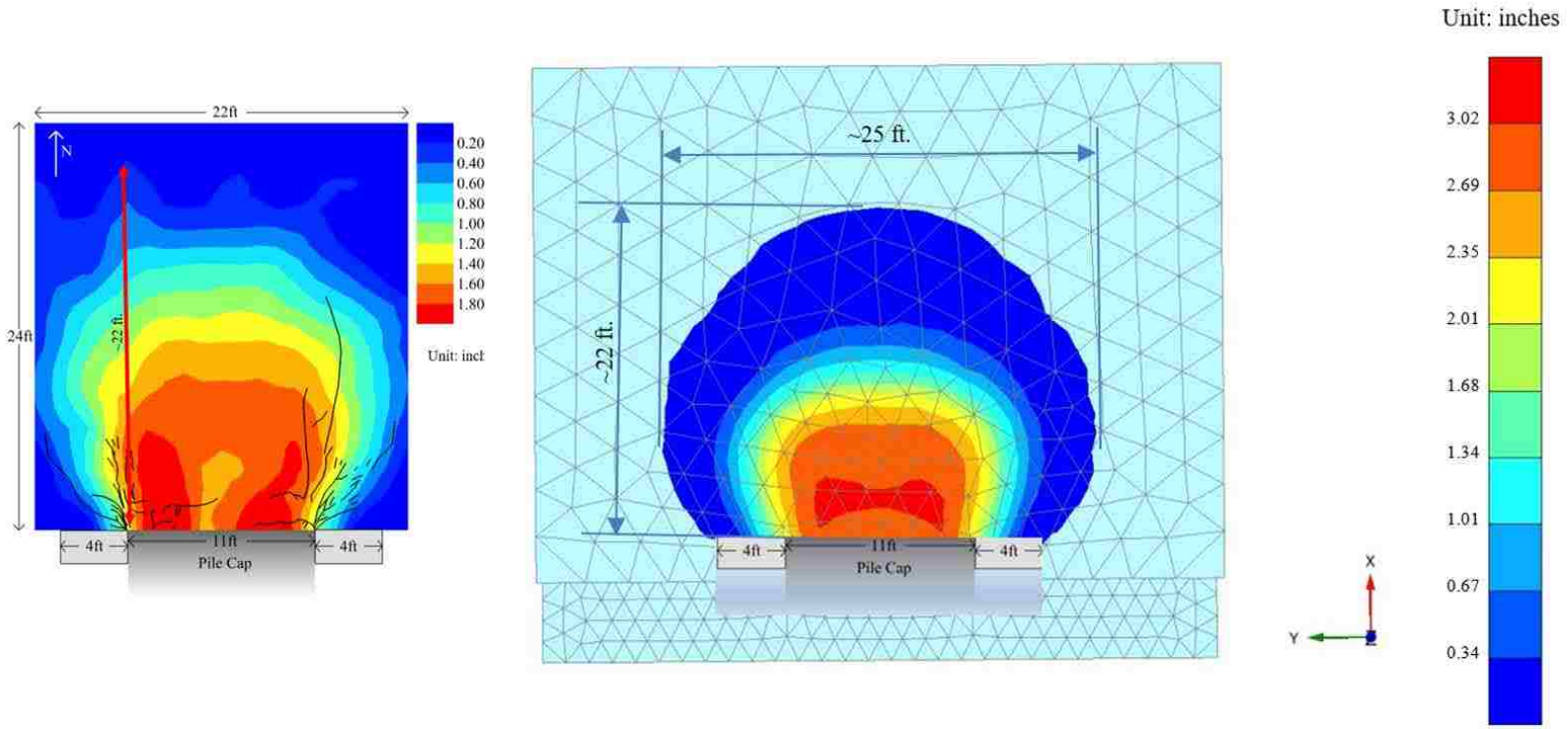

Figure 5-10: Comparison of Measured and Computed Heave Contours for 0º Skew Pile Cap (Top figure was measured from field tests; Bottom figure was computed by Plaxis 3D.)

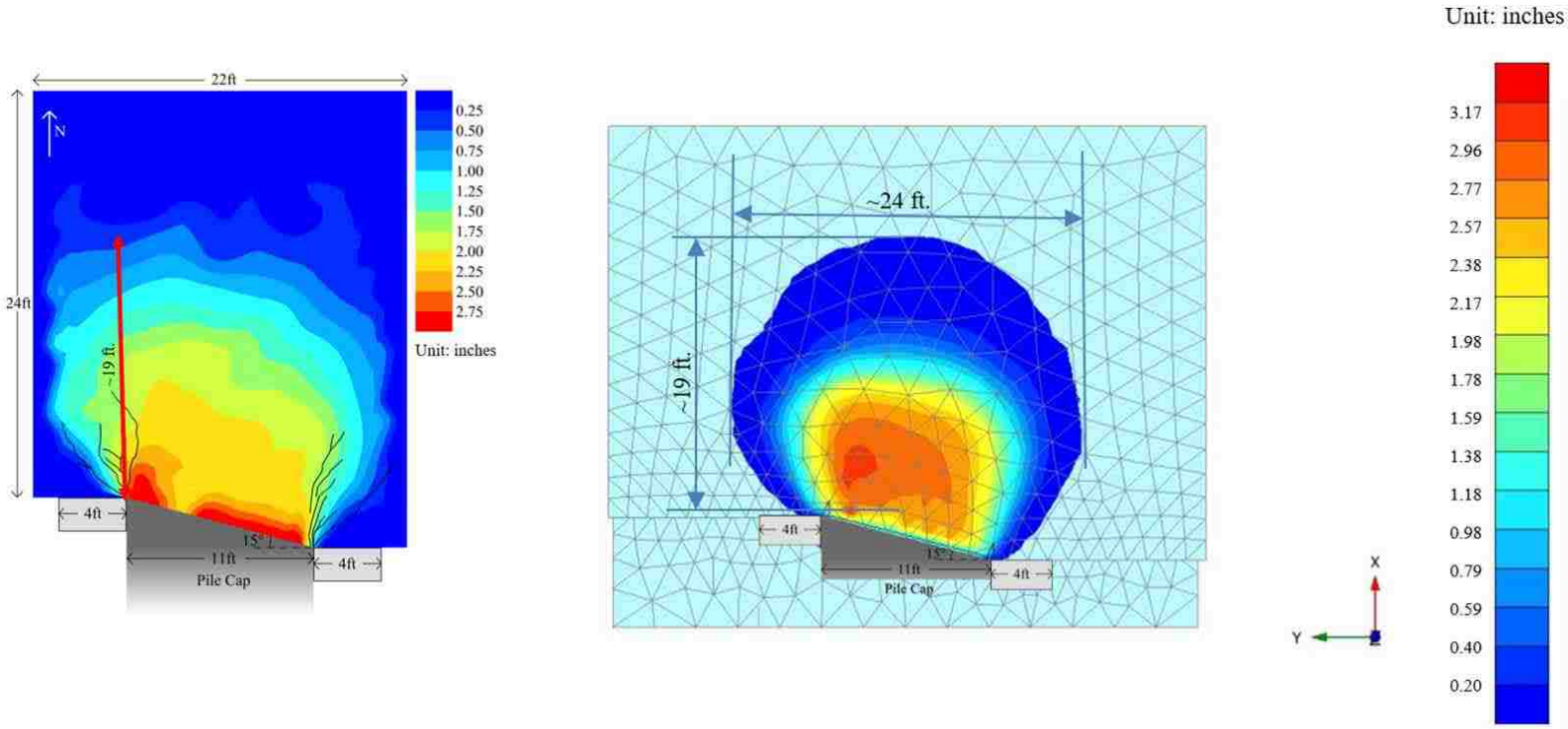

Figure 5-11: Comparison of Measured and Computed Heave Contours for 15° Skew Pile Cap (Top figure was measured from field tests; Bottom figure was computed by Plaxis 3D.)

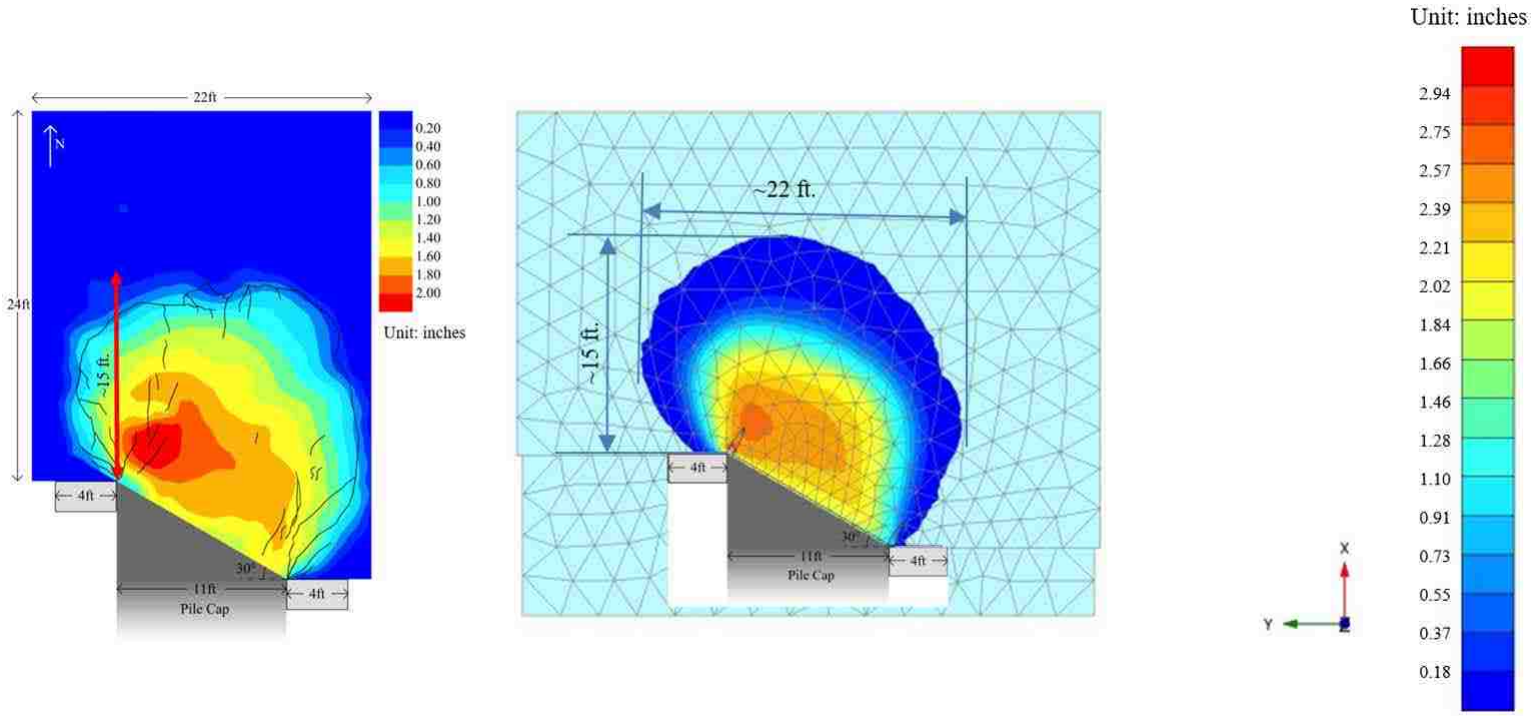

Figure 5-12: Comparison of Measured and Computed Heave Contours for 30° Skew Pile Cap (Top figure was measured from field tests; Bottom figure was computed by Plaxis 3D.)

Figure 5-13 shows the plots comparing the measured and computed heave contours for the 45°. In general, the same trends are observed as seen for the 15° and 30° tests, that is, maximum heave zone appears even closer to the acute corner. This zone is approximately 8 feet from the tip of acute corner to north end of the zone in longitudinal direction; and approximately 15 feet from the tip of the acute corner to the east side of the zone in transverse direction. In contrast, the heave zone in the field test was 22 feet in width. The heave zone also extended 14 feet into the soil backfill from the tip of the acute corner in longitudinal direction.

The discrepancy between the measured and computed heave contours in this case is due to the transverse slipping of the pile cap which was discussed in Section 5.1.2. Because of the slippage the heave was more locally concentrated and the heave zone predicted by the computer model stopped growing.

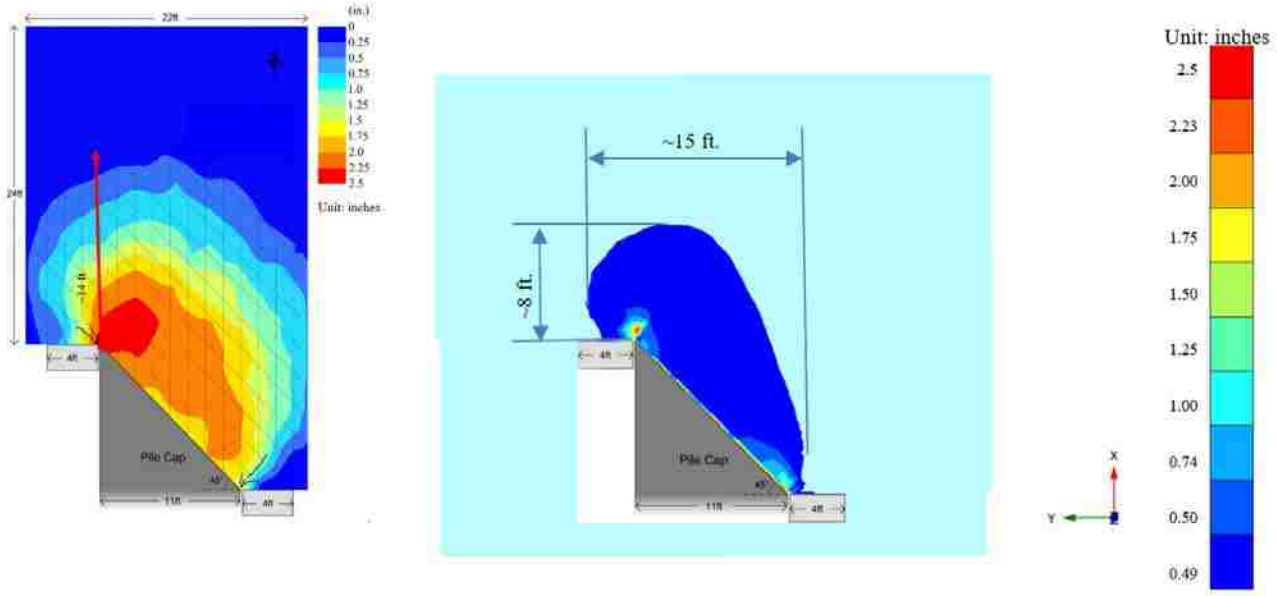

Figure 5-13: Comparison of Measured and Computed Heave Contours for 45° Skew Pile Cap (Top figure was measured from field tests; Bottom figure was computed by Plaxis 3D.)

5.1.5 Longitudinal Displacement (Ux)

Longitudinal displacements (Ux) only account for the horizontal displacements in the x direction. Figures (a) to (c) in Figure 5-14 show the three dimensional shape of the longitudinal displacement profiles for 0°, 15°, and 30° skew models in an iso-surface view in Plaxis 3D.

All the models have bulb shapes which suggest a log spiral failure surface at the bottom along with semi elliptical bulb shapes on the ground surface. The shapes also indicate that longitudinal cross sections will have log spiral shapes as mentioned in Section 2.1.3. With an increase in the skew angle, the shape of the bulb becomes less symmetric about the longitudinal axes and skews more and more to the acute angle of the pile cap as shown in Figure 5-14.

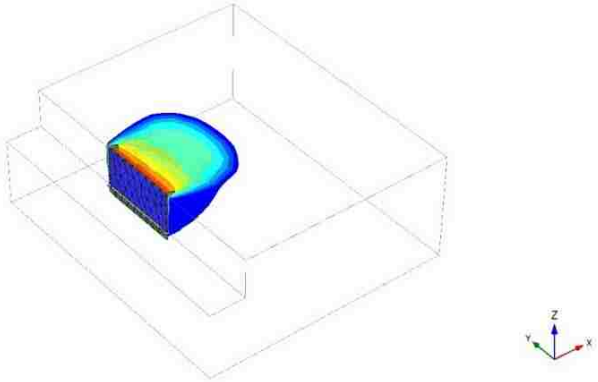

(a) 0° Skew Pile Cap with Homogenous Compacted Sand Backfill

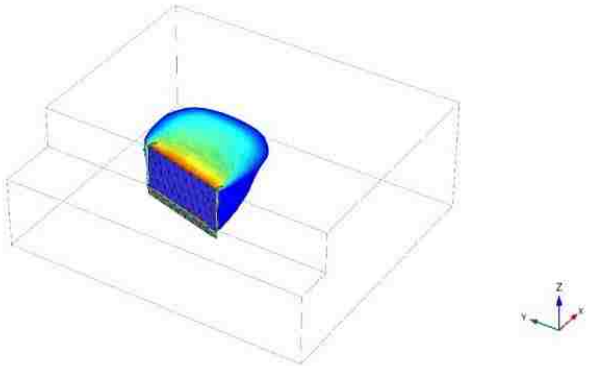

(b) 15° Skew Pile Cap with Homogenous Compacted Sand Backfill

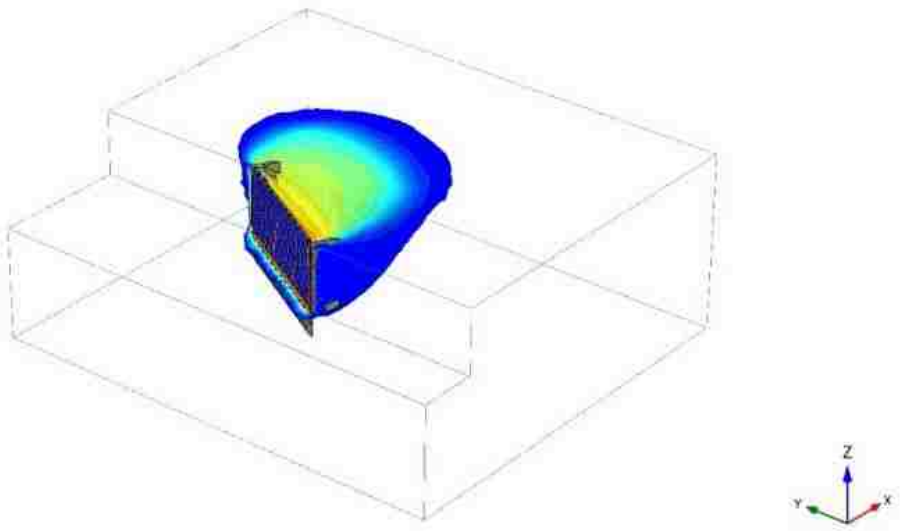

(c) 30° Skew Pile Cap with Homogenous Compacted Sand Backfill

Figure 5-14: Iso-Surface Views of Longitudinal Displacements for 0,15 and 30 Skew Sets

Figure 5-15 shows plan views of the longitudinal displacements. As stated previously, semi-elliptical bulbs skews toward the acute angle of the backwall as shown in Figure (b) and (c) for 15° and 30° models, respectively.

The maximum longitudinal displacement zone occurred within a 2 feet range behind the backwall for all sets. The widths of the longitudinal displacement zone are the same when measured parallel to the backwall with a value of 20 feet. The extent values of the failure zones were measured to be 17 feet, 15 feet, and 13 feet for 0°, 15° and 30° skew sets, respectively. Section view planes were indicated on each figure in Figure 5-15 to prepare information for Figure 5-16.

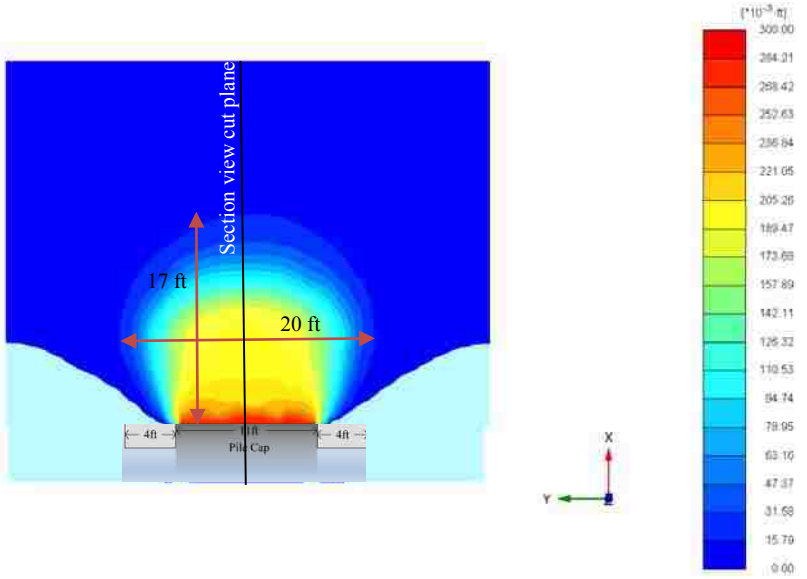

(a) Top View for Longitudinal Displacement for 0° Skew Pile Cap

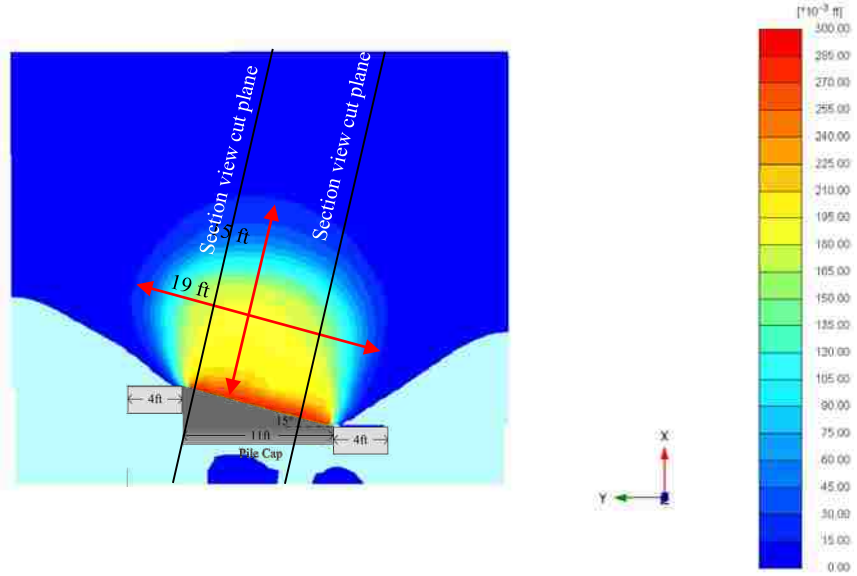

(b) Top View for Longitudinal Displacement for 15° Skew Pile Cap

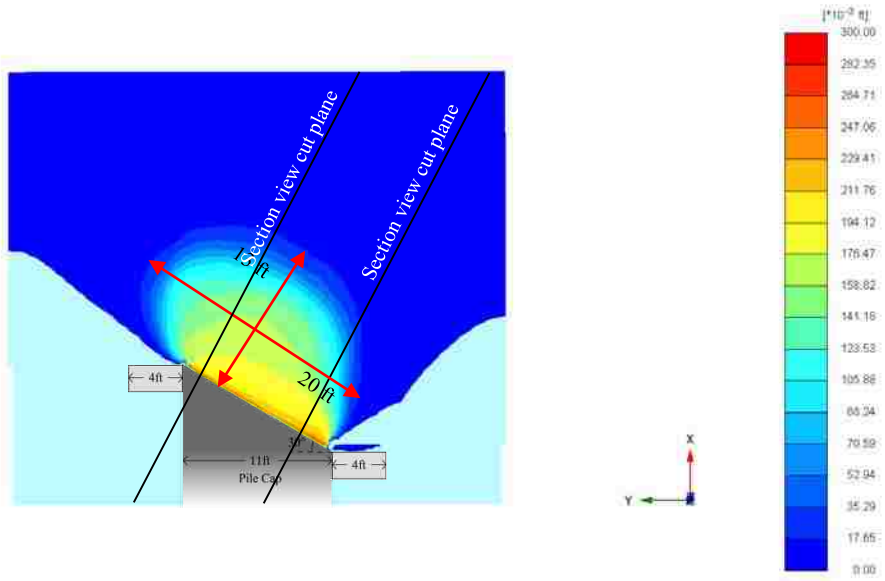

(c) Top View for Longitudinal Displacement for 30° Skew Pile Cap

Figure 5-15: Top View showing Longitudinal Displacements for All Models

Figure 5-16 shows individual section views for 0°, 15°, and 30° skew models, where locations of these section planes were identified in Figure 5-15. The results were analyzed qualitatively. Three section views show log-spiral interfaces which first go down from the bottom corner, then curve upward and extend outward in an approximately linear manner until it intersects the ground surface. Displacement bulbs along the backwalls appeared to have parabolic shapes. Displacements are minimal around top and bottom of the backwall and peak around two third of the total height from the ground down. Figure (b) to (c) show decreasing trend in longitudinal displacement from the 15° skew set to the 30° skew set. This phenomenon is due to the fact which was mentioned previously: with increasing skew angle, the shape of the bulb skews more and more to the acute angle of the pile cap.

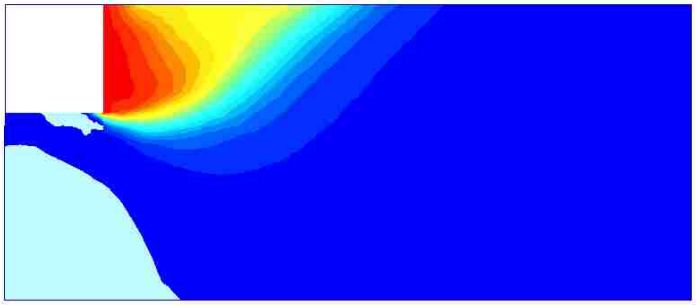

(a) Section View for Longitudinal Displacement for 0° Skew Pile Cap

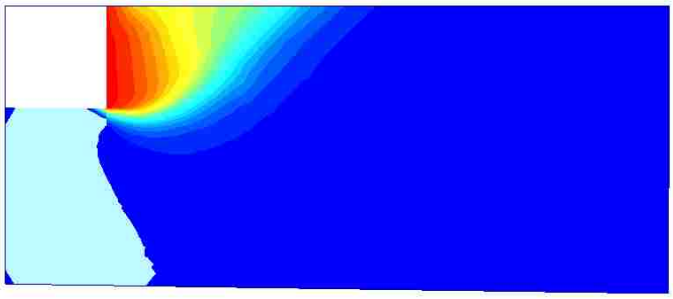

(b) Section View for Longitudinal Displacement for 15° Skew Pile Cap (Closer to the Obtuse Side)

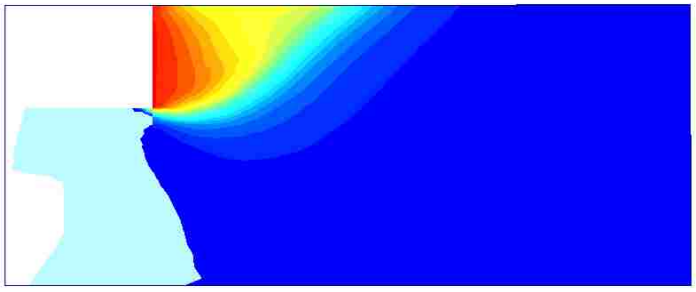

(c) Section View for Longitudinal Displacement for 15° Skew Pile Cap (Closer to the Acute Side)

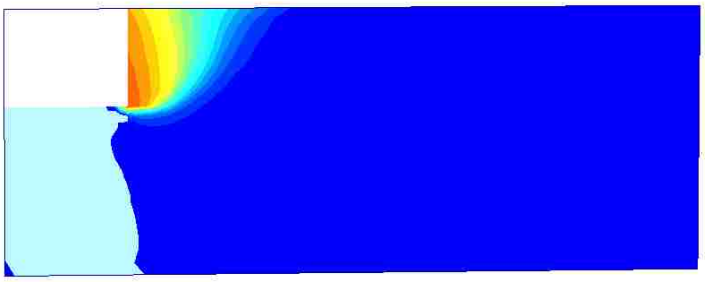

(d) Section View for Longitudinal Displacement for 30° Skew Pile Cap (Closer to the Obtuse Side)

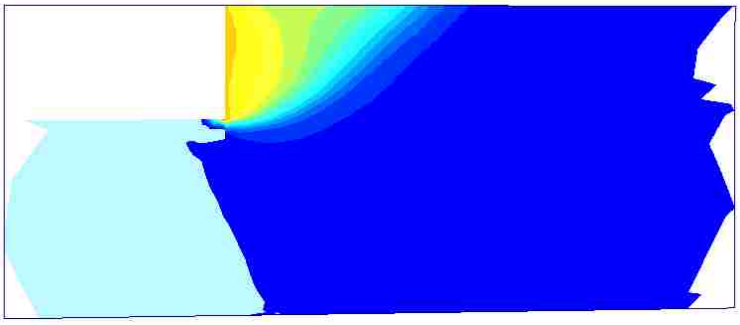

(e) Section View for Longitudinal Displacement for 30° Skew Pile Cap (Closer to the Acute Side)

Figure 5-16: Section View for Longitudinal Displacements for All Sets

Figure 5-17 shows the summary comparison of longitudinal displacements for 0°, 15° and 30° models. All sections on the left were obtained by cutting perpendicularly to the backwall and offsetting 2 feet from the west point of the backwall; All sections on the right were obtained by cutting perpendicularly to the backwall and offsetting 2 feet from the east point of the backwall. Figures on each row show that as skew angle increases the longitudinal displacement close to the acute corner extends further than that the displacement close to the obtuse corner. Figures on left

column show that as skew angle increases, longitudinal displacement close to the acute corner slightly extends into soil back fill. Figures on right column show that as skew angle increases, longitudinal displacement close to the obtuse corner retreats back dramatically. All of this evidence indicates that as skew angle increases, the longitudinal displacement profile skews more to the acute side of the backwall.

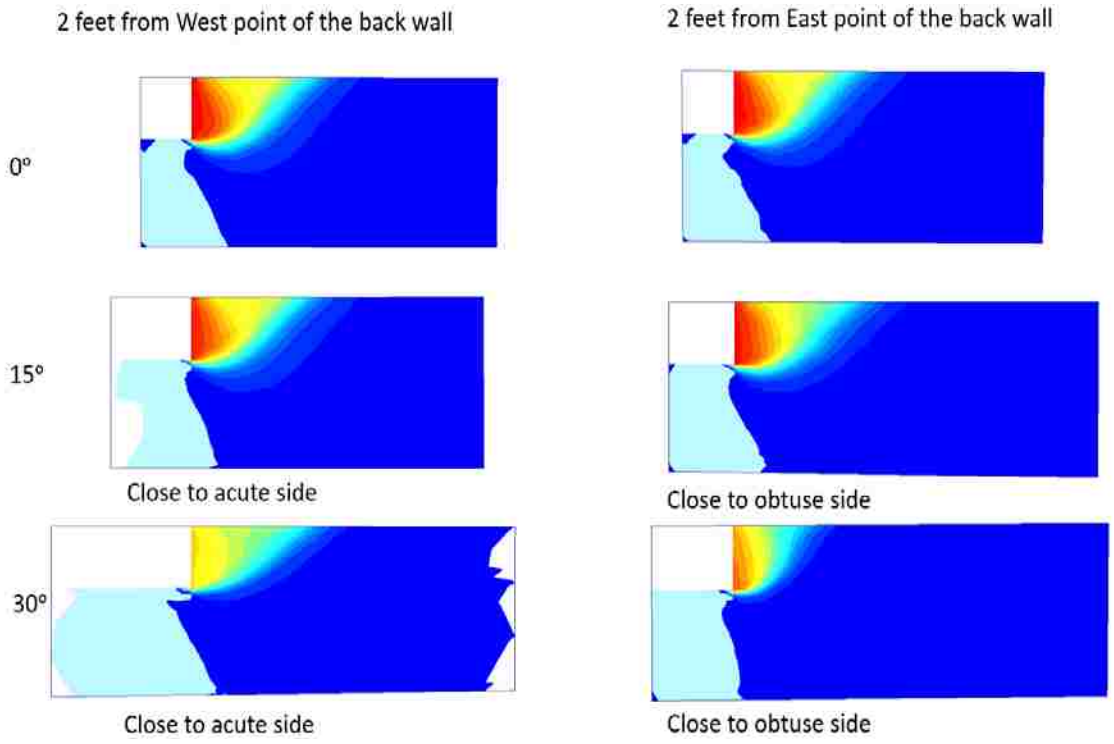

Figure 5-17: Longitudinal Displacement Comparison for All Sets

Figure 5-18, Figure 5-19 and Figure 5-20 are total backfill displacement versus distance curves from the face of the backwall at selected cap displacement intervals for the 0°, 15° and 30° tests from Rollins and Marsh (2013).

In order to compare the measured and computed results, measured displacement versus distance curves for the maximum cap displacement were selected for each test. Longitudinal displacement versus distance curves computed at the ground surface by Plaxis 3D are plotted along with the measured curves in Figure 5-21, Figure 5-22, and Figure 5-23 for the 0°, 15° and 30° tests, respectively. Eight data points were picked to define the curve for the 0°, and 15° skew tests with maximum measured cap displacements of 3.21 inches and 3.77 inches, respectively, while 7 points were used to define the curve for the 30° skew set which a maximum total cap displacement of 3.45 inches.

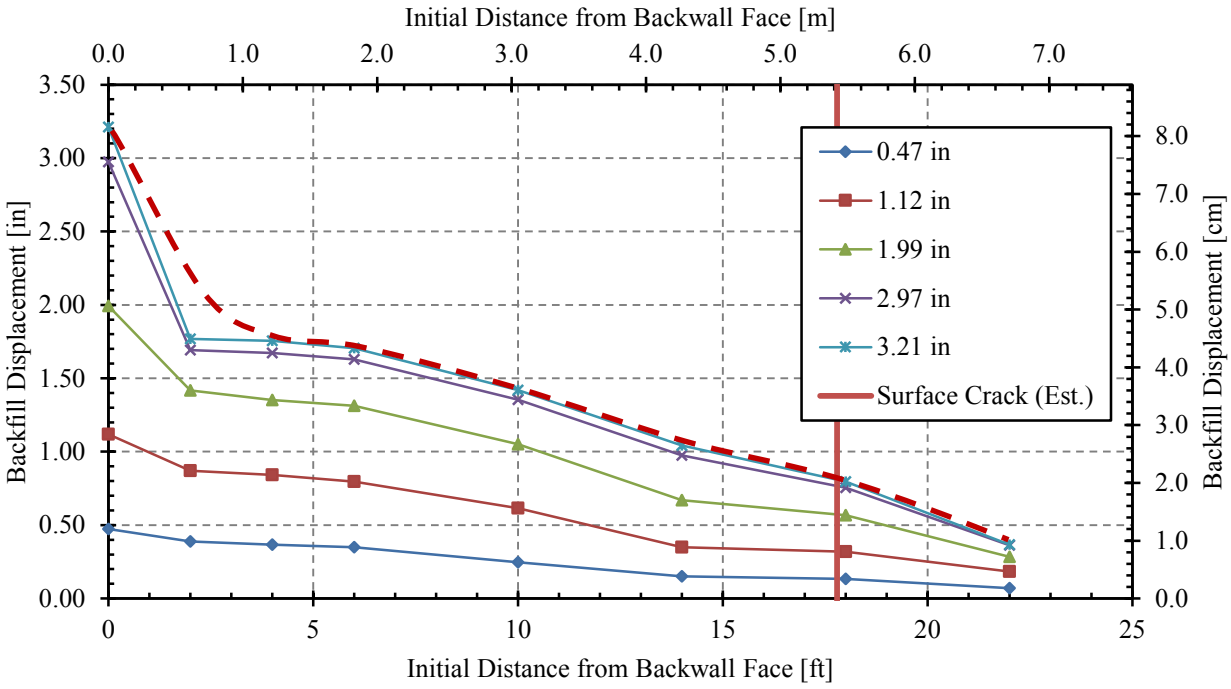

Figure 5-18: Total Backfill Displacement versus Distance from Backwall Face at Selected Cap Displacement Intervals for the 0° Test (Rollins Marsh 2013)

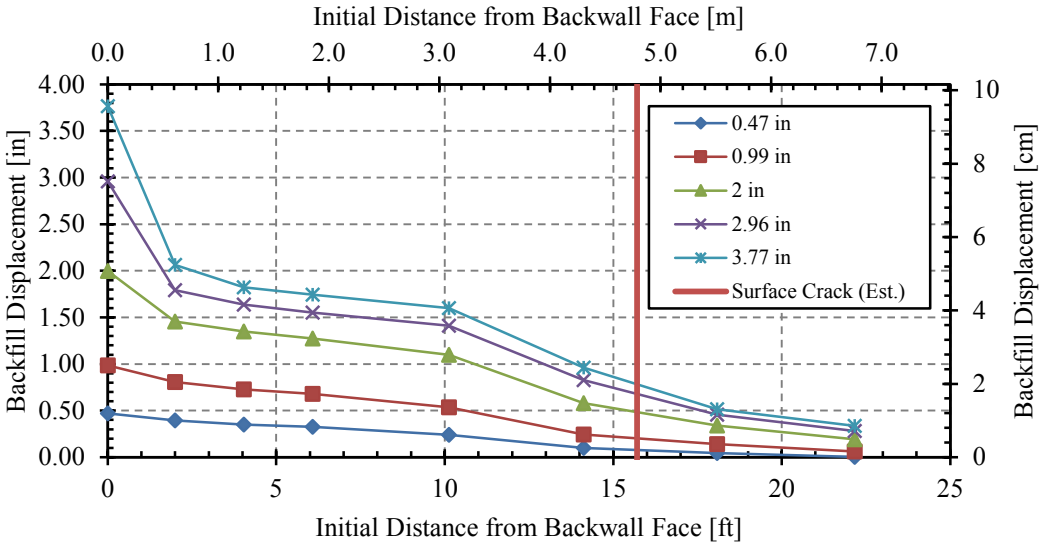

Figure 5-19: Total Backfill Displacement versus Distance from Backwall Face at Selected Cap Displacement Intervals for the 15° Test (Rollins and Marsh 2013)

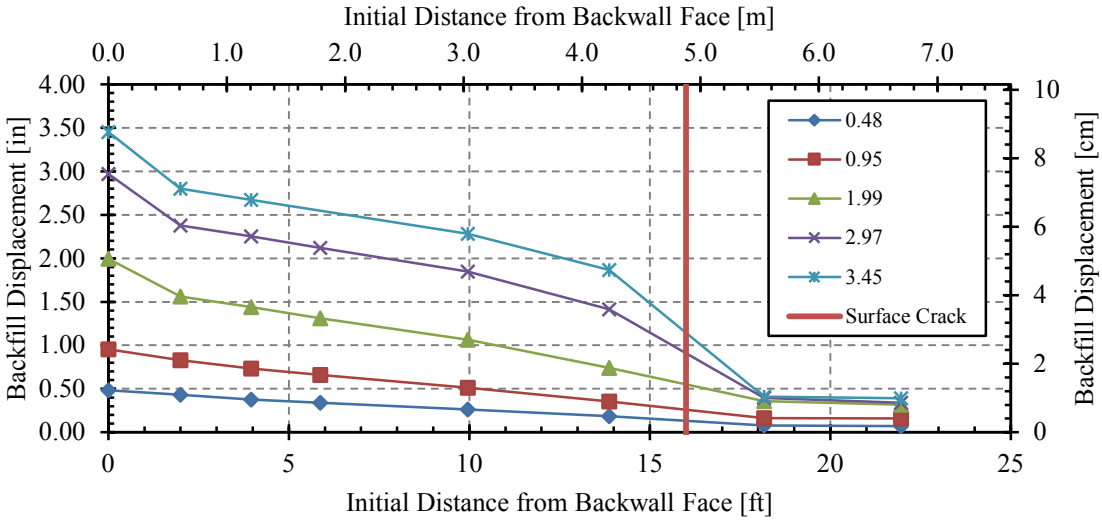

Figure 5-20: Total Backfill Displacement versus Distance from Backwall Face at Selected Cap Displacement Intervals for the 30° Test (Rollins and Marsh 2013)

Figure 5-21, Figure 5-22 and Figure 5-23 compare total backfill displacement at the largest cap displacements with computed longitudinal backfill displacements from Plaxis 3D for the 0°, 15°, and 30° skew tests. Computed displacements from each finite element model were obtained by first cutting a section through the middle of the soil volume in longitudinal direction to correspond with the field measurements. Then a line was drawn on the top surface of the cross section to gather longitudinal displacement versus relative distance from the face of the backwall.

On the surface of the ground, the total displacement includes x, y and z directional movement, where y directional movement (lateral movement) is negligible for the 0°, 15° and 30° skew models. However, z directional heave (vertical movement) is significant in comparison with x directional movement (longitudinal movement). Thus, the measured curves in Figure 5-21, Figure 5-22 and Figure 5-23 are not strictly longitudinal displacements. In addition, there is some discrepancy between the maximum pile cap displacement in the field and in the computer models, so that the comparison is not direct one to one comparisons.

All three figures show that the backfill displacement from the finite element models are in reasonably good agreement with the displacements measured in the field tests. Typically, the greatest change in displacement occurred within the first 2 feet from the backwall for all three tests. For the 0° and 15° tests, after a rapid decrease in backfill displacement at about 2 feet from the pile cap, a much more gradual decrease of backfill displacement occurred from 2 feet to 10 feet from the pile cap. Beyond about 10 feet from the cap, a rapid decrease in backfill displacement occurred again as the backfill compressed against the relatively stationary soil behind the failure zone. For the 30° test, computed results show behavior somewhat similar to that for the 0° and 15° tests. However, the rapid decrease in displacement boundaries started to become less clear and the whole curve tended to become a more linearly decreasing pattern, which provides an upper bound

to the measured data. Overall, for the three tests, the computed results show similar decreasing pattern in comparison with the measured curves for the 0°, 15° and 30° tests.

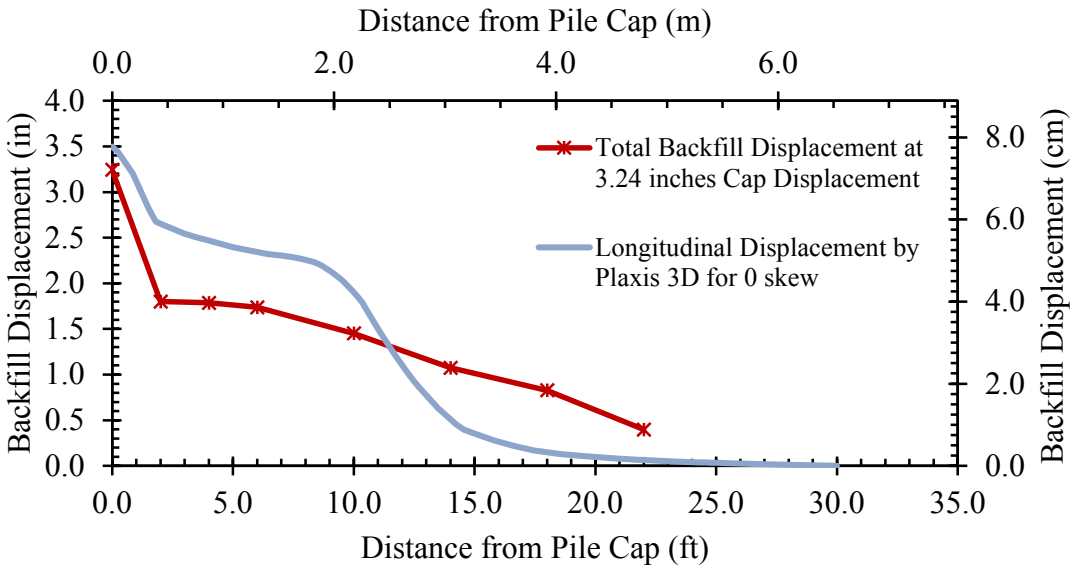

Figure 5-21: Total Backfill Displacement Curve from Field Test and Longitudinal Displacement Curve from Plaxis 3D for 0° Skew Set

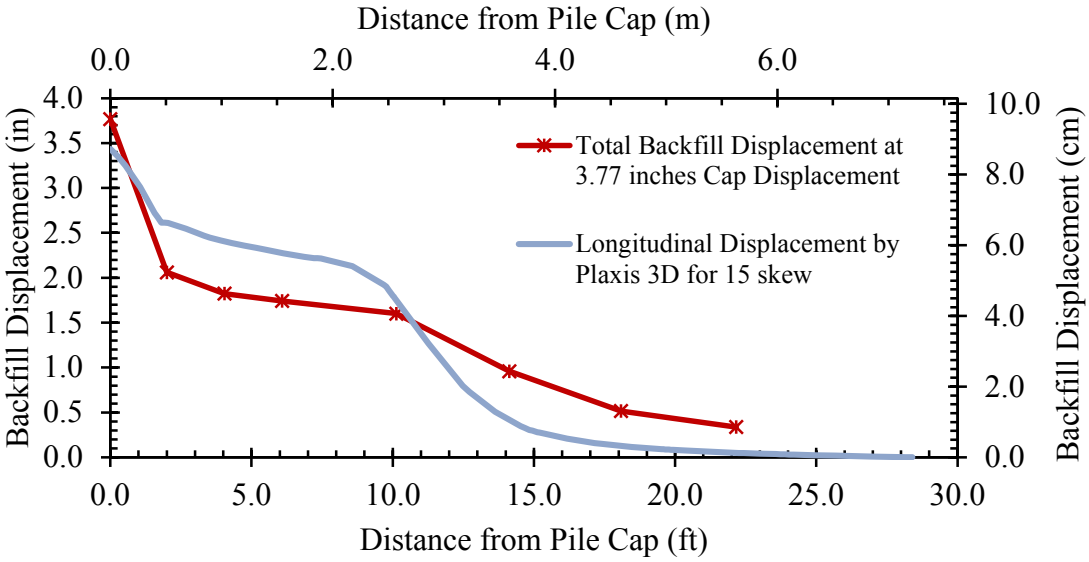

Figure 5-22: Total Backfill Displacement Curve from Field Test and Longitudinal Displacement Curve from Plaxis 3D for 15° Skew Set

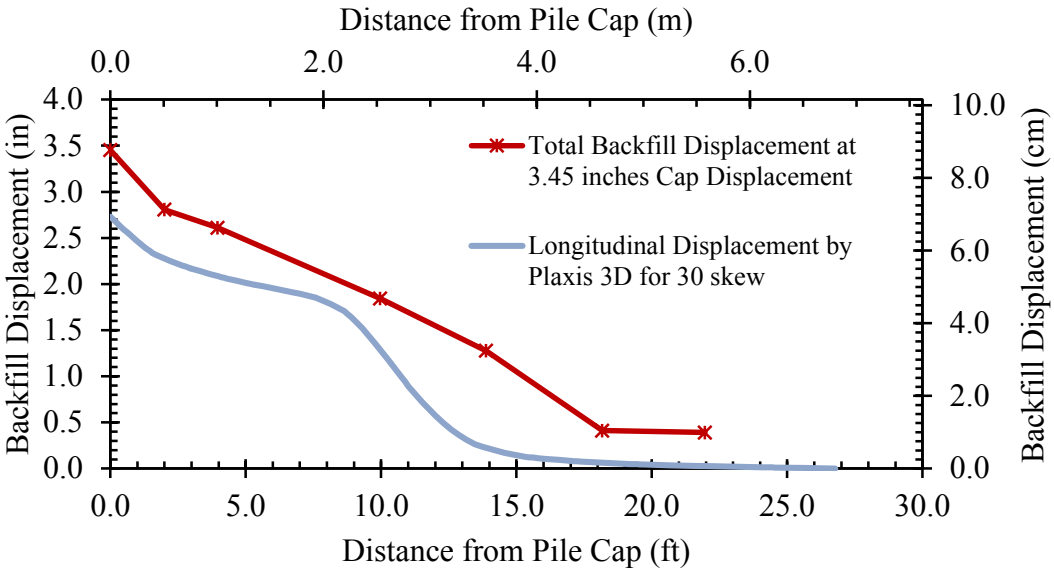

Figure 5-23: Total Backfill Displacement Curve from Field Test and Longitudinal Displacement Curve from Plaxis 3D for 30° Skew Set

5.1.6 Incremental Shear Strains and Total Shear Strains

The concept of incremental shear strain was invented by Norris (1977) and Ashour et al. (1998). Incremental shear strain contours can show critical shear failure surfaces caused by longitudinal translation of the back wall into the soil back fill. Figure 5-24 shows incremental shear strain contours computed with Plaxis 2D by Rollins and Nasr (200) with 5.5ft deep back wall pushing into backfill with Homogenous loose sand and with a narrow gravel zone adjacent to the pile cap. The failure surfaces show a punching shear behavior which initiates from the base of the back wall with a curved log spiral shape, and extends outward in an approximately linear manner to the ground surface.

Figure 5-25 shows the incremental shear strain contours obtained from Plaxis 3D for the 0° skew test. The figure was overlaid with the field test results for shear plane. The shear strain

profile from Plaxis 3D exhibits good agreement with the field test up to about 9 feet from the backwall. This portion is approximately within the log-spiral section. Then the failure surface in the field test developed in a linear fashion to the ground surface. In contrast, the Plaxis 3D results suggest that the failure surface takes a more parabolic path to the ground surface with a failure surface that is at least two times shorter than the linear surface exhibited in the field. Comparing to Rollins and Nasr (2010), the results from Plaxis 3D shows a less defined linear shape, but well defined upper and lower curved log spiral portion. This is similar to the shape of the contours from longitudinal displacement mentioned in section 5.1.5.

This result is for the purpose of comparison with Rollins and Nasr (2010). Thus, shear strain for 15° and 30° will be omitted.

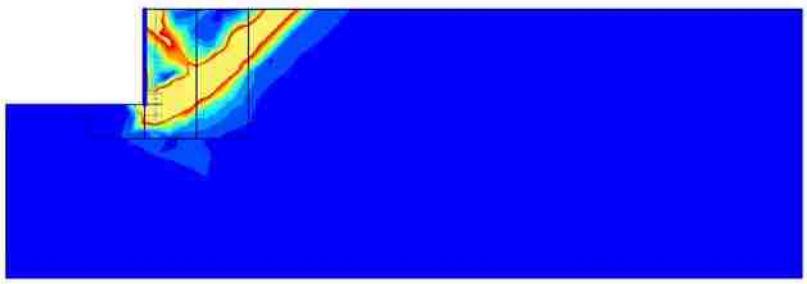

(a) Homogenous loose sand backfill

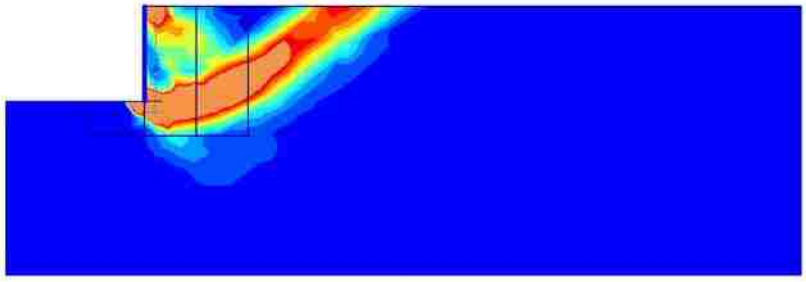

(b) Homogenous gravel backfill

Figure 5-24: Incremental Shear Strain Profiles of 5.5-ft (1.68-m) Deep Pile Cap with Backfills Consisting of: (a) Full width (Homogeneous) Loose Silty Sand; (b) Full Width (Homogeneous) Dense Gravel; (Rollins and Nasr 2010)

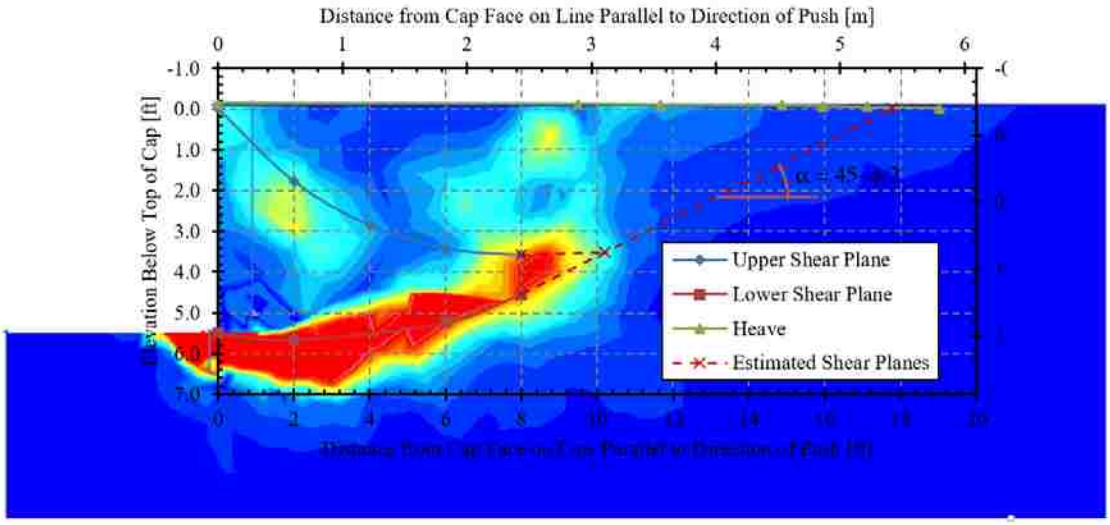

Figure 5-25: Incremental Shear Strain versus Internal Failure Surfaces for 0° skew

Figure 5-26 shows comparison of Plaxis 2D results from Rollins and Nasr (2010), and Plaxis 3D results from this research using calibrated figure dimensions for the 0° skew model. It may be seen that the Plaxis 3D results have a more complicated pattern than the results from Plaxis 2D as discussed above. The log spiral portion in Plaxis 3D result is similar in length and shape to that in the Plaxis 2D model with homogenous gravel backfill which seems reasonable because the friction angle of the backfills is similar. However, the failure surface in the 3D models does not appear to follow a linear shape as it extends to the ground surface. Instead the Plaxis 3D model appears to show a curvilinear failure surface which reaches the ground more quickly that observed in the field. This failure surface intersects the ground surface at a distance that is similar to that seen for the Plaxis 2D model with homogenous loose sand backfill. Plaxis 3D result is likely more realistic since it considers the whole soil volume's behavior in three dimensional space.

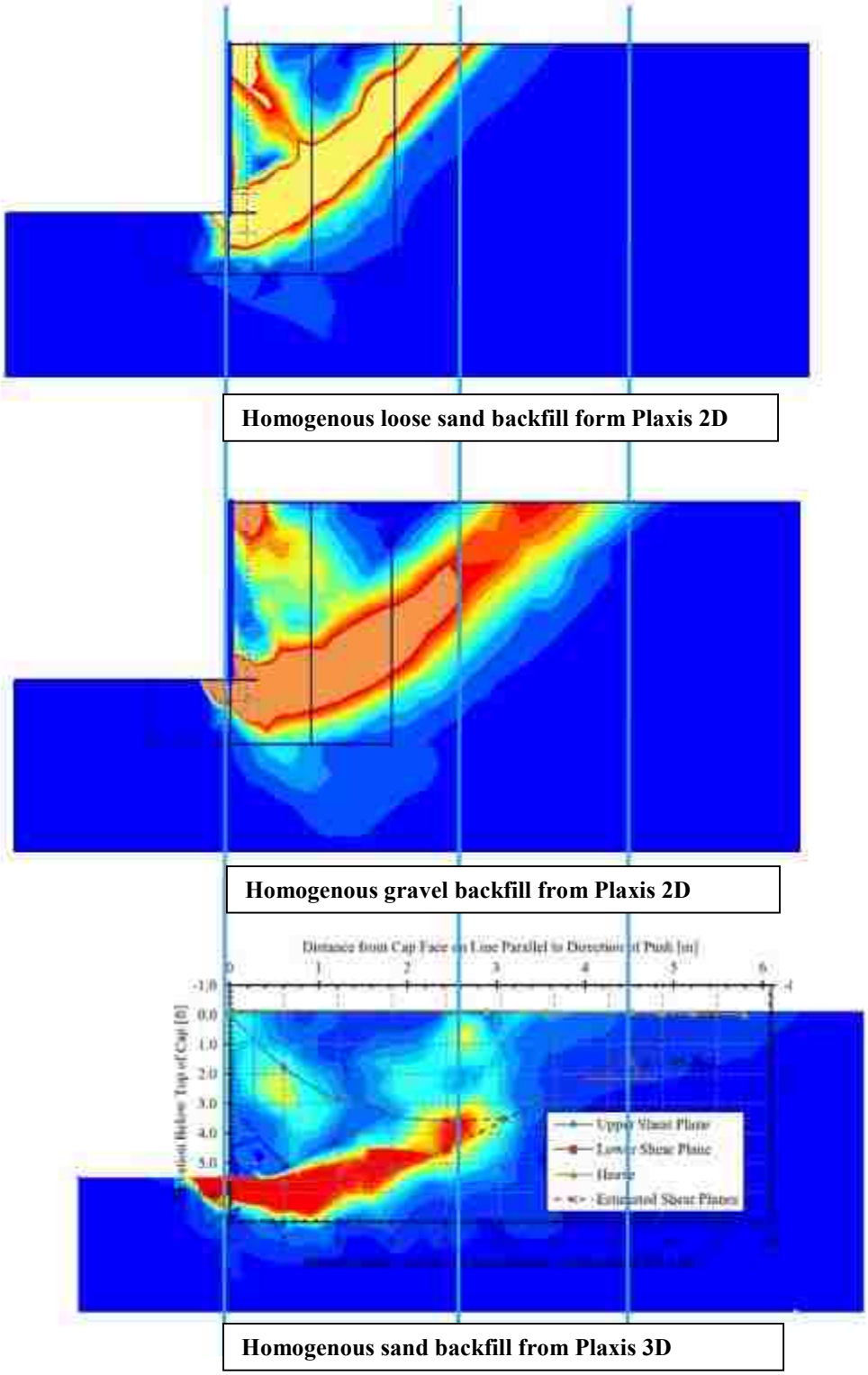

Figure 5-26: Plaxis 2D and 3D Results Comparison for 0° Skew

To compare the measured and computed internal failure planes for the 0°, 15° and 30° skew tests, total horizontal shear strain (normal horizontal shear strain, γ_{xz} in Plaxis 3D) was used to present difference between the computer models and field test.

Figure 5-27 shows the total horizontal shear strain plot against measured the failure plane geometry measured in the field for 0° skew set. There are two sections of total shear strain with different direction of movement. The upper shear plane measured in the field occurred between these two computed sections. The lower shear plane occurred in a log spiral fashion within the maximum computed shear strain zone. The upper section has smaller strain and close to zero, which agrees with the fact that in field, no shear plane was observed in the linear part of the failure surface until it intersected the ground surface and created cracks. Overall, the computed total horizontal shear strain is in good agreement with failure planes obtained in field test for 0° skew.

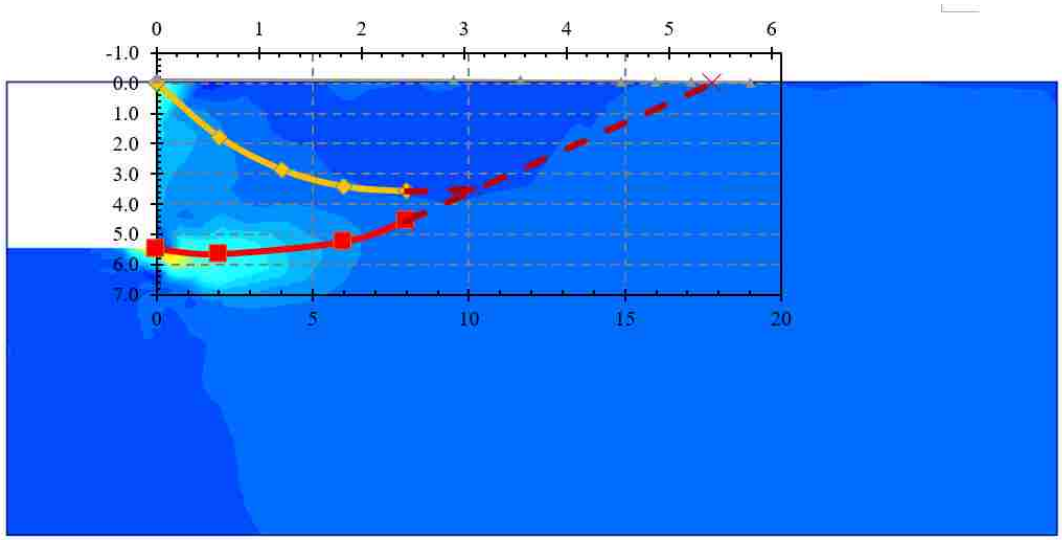

Figure 5-27: Total Shear Strain versus Failure Plane for 0° Skew Set

Figure 5-28 and Figure 5-29 show the total horizontal shear strain plot against measured failure plane in the field close to the west and east side of the pile cap respectively for 15° skew

test. Both figures show good agreement on the log spiral section of the lower failure plane. In Figure 5-28, a shear zone close to the backwall could lead to upper measured shear plane. Further extending to the soil away from the backwall, a shear zone developed upward in a linear fashion, and increased faster than what is predicted in the field. Figure 5-29 on east side shows really good agreement on both the log spiral section and linear section.

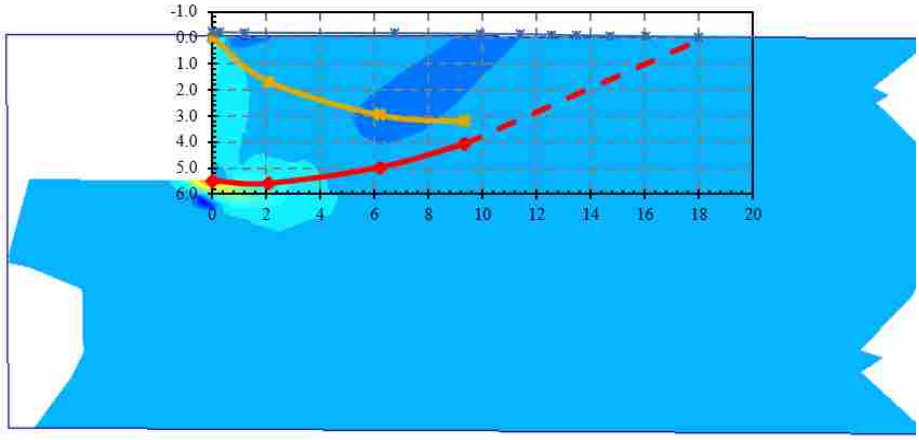

Figure 5-28: Total Shear Strain versus Failure Plane for 15° Skew Set on West Side near Acute Angle

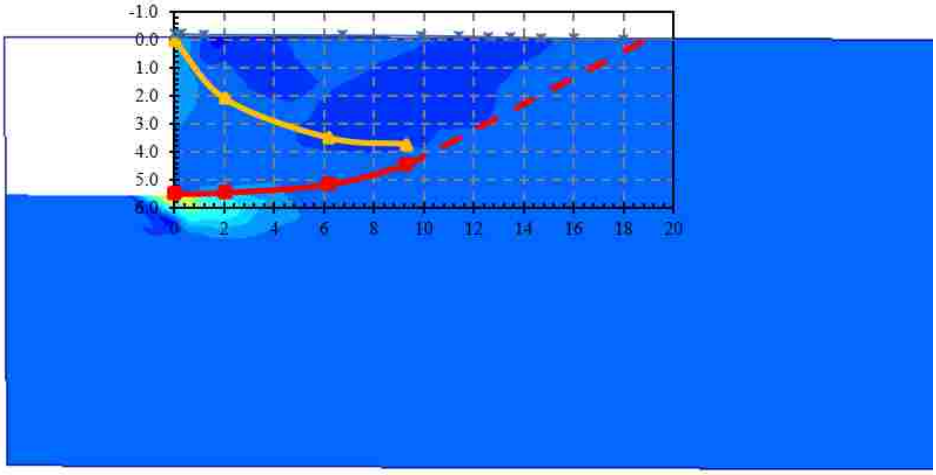

Figure 5-29: Total Shear Strain versus Failure Plane for 15° Skew Set on East Side near Obtuse Angle

Figure 5-30 and Figure 5-31 show the total horizontal shear strain plotted against the measured failure plane in the field close to the west and east sides of the pile cap respectively for 30° skew test. Both cases have a fairly small portion of measured log-spiral failure section, which is consistent with the Plaxis 3D model that shows a small section of total shear strain near the bottom of the back wall. Linear failure planes were observed in field and computed model afterwards, for both west and east section cut planes. It worthwhile to notice that on the west side close to the acute corner of the cap, the computed model lined up with the field test quite well. In conclusion, the finite element model successfully matched the measured results.

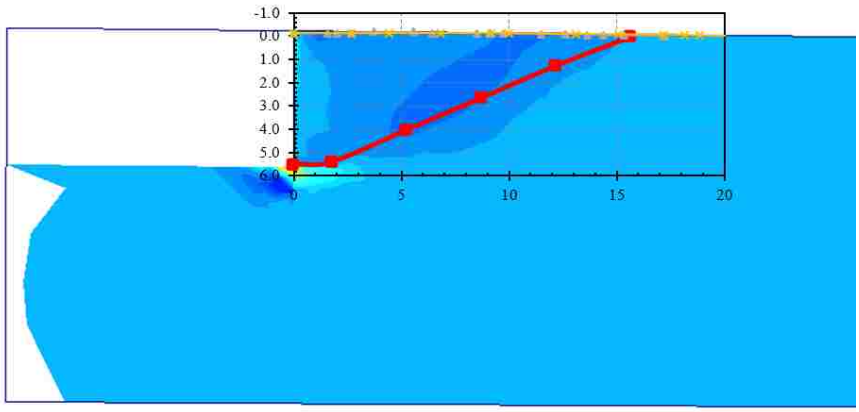

Figure 5-30: Total Shear Strain versus Failure Plane for 30° Skew Set on West Side near Acute Angle

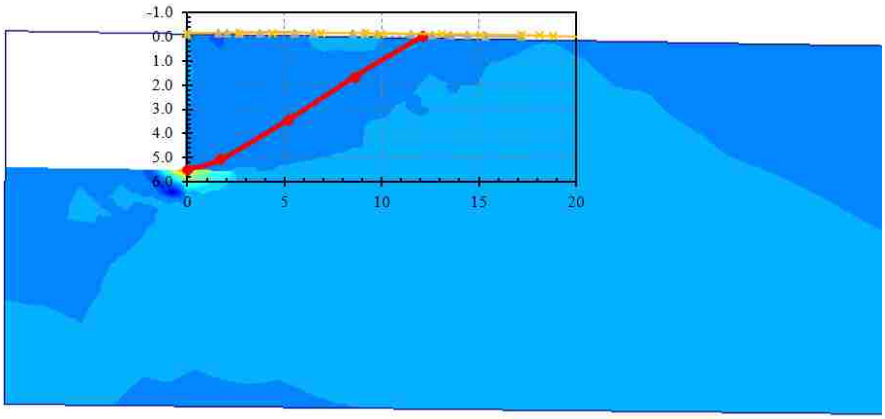

Figure 5-31: Total Shear Strain versus Failure Plane for 30° Skew Set on East Side near Obtuse Angle

5.2 Parametric Studies

The studies described previously suggest that the computer models can predict many of the essential features observed in the field tests with an acceptable accuracy. In this section, a series of parametric studies were conducted using calibrated models for 0 skew abutment in Plaxis 3D. The purpose of these studies is to evaluate the influence of individual parameter on the passive behavior of the backfill-abutment wall system. The results and conclusion can be used for future studies. The selected factors include: soil friction angle, wall friction angle, soil angle of dilatancy, soil stiffness, and y directional restraint.

5.2.1 Effect of Soil Friction Angle (ϕ)

Figure 5-32 shows passive force versus displacement curves for three 0° skew models with identical geometries and material parameters but with varying soil friction angles. At an approximate displacement of 2.5 inches, the passive force-displacement curve from the field test reached its peak value. The corresponding peak values for the three sets are summarized in Table 5-2. The observation shows that for every 1 degree increase in soil friction angle, passive force will increase 7 percent relative to the previous value. The result indicates that the soil friction angle has a profound effect on the passive force-deflection relationship and should be selected carefully. This observation can also help in the calibration of original model if a great range of value needs to be adjusted in order to fit within a 10 % error of the passive force-deflection curve obtained from the field test.

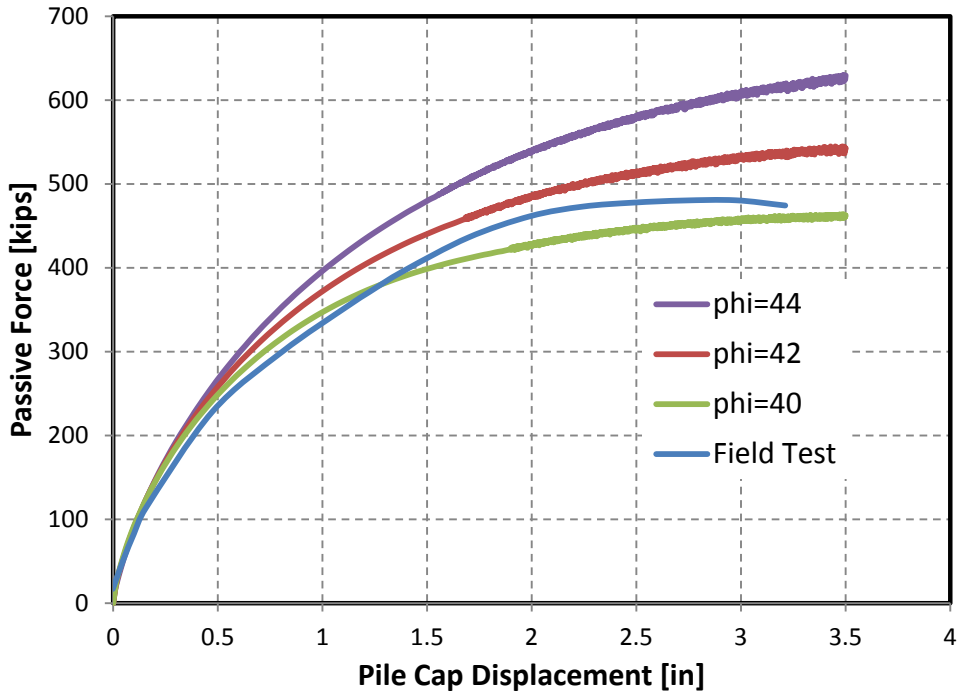

Figure 5-32: Passive Force - Deflection Curve for Different Soil Friction Angle Sets

Table 5-2: Max. Passive Force for Different Soil Friction Angles

Soil Friction, ϕ degree	*Passive Force*		*% increase*	*% increase per unit change*
	kips	*kN*		
40	445	1979	N/A	N/A
42	511	2273	14.8%	7.4%
44	579	2576	13.3%	6.6%

5.2.2 Effect of Wall Friction Angle (δ) and Strength Reduction Factor (R_{inter})

As mentioned in Section 4.3, the strength reduction factor is defined by the equation (4-1).

Figure 5-3 illustrates the results of changing wall friction angles with corresponding strength reduction factors. The curves show that passive force increases when the strength reduction factor and wall friction increase.

Passive force values increase one percent with respect to a one-degree change in soil friction angle as shown in Table 5.3. However, the passive force values are not linearly increased corresponding to changes in strength reduction factor.

Table 5-3 shows that increasing reduction factor from 0.6337 to 0.6881 leads to increasing 38 percent per unit change in Rinter; whereas increasing reduction factor from 0.6881 to 0.7447 leads to increasing 36 percentage per unit change in Rinter. This is due to non-linear equation for strength reduction factor as show in Equation (4-1).

These results suggest that the Plaxis 3D model is less sensitive to variations in wall friction than a conventional Log-spiral solution in which the passive force would increase by about 3.5% for a one degree change in the wall friction for the conditions involved in this test. It is unclear if this is true in all cases.

Table 5-3: Max. Passive Force for Different Wall Friction Angle Sets

Wall Friction, δ Degree	*R_{inter}*	*δ/ϕ*	*Passive force at 2.5 inches displacement*		*% increase per unit change in R_{inter}*	*% increase per unit change in δ*
			kips	*kN*		
28	0.6337	0.7	433	1926	N/A	N/A
30	0.6881	0.75	442	1966	38%	1%
32	0.7447	0.8	451	2006	36%	1%

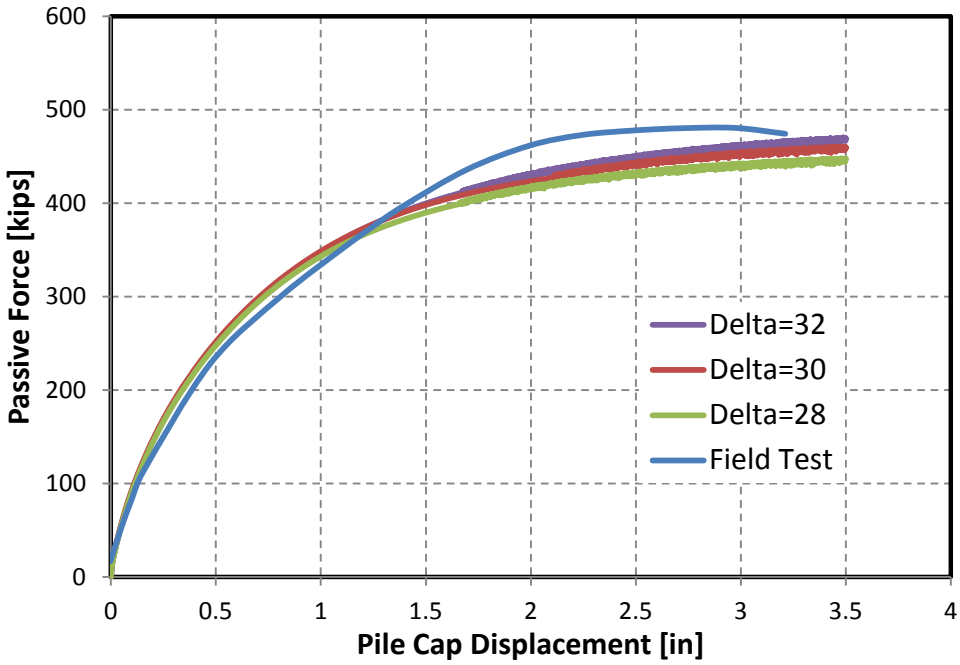

Figure 5-33: Passive Force - Deflection Curve for Different Wall Friction Angle Sets

5.2.3 Effect of Angle of Dilatancy (ψ)

Figure 5-34 shows individual passive force versus displacement curves for varying angles of dilatancy. The dilatancy angle is an indication of the strength gain accompanying dilation and increases as the soil becomes denser Passive force increases significantly as the angle of dilatancy increases. As shown in the calculated values listed in Table 5-4, every degree of increase in the angle of dilatancy results in a 1.7 to 1.8 percent increase in the passive force.There is apparently a small decline in the rate of increase as the dilatancy angle increases.

Table 5-4: Max. Passive Force for Different Dilatancy Angle Sets

Dilatancy angle, ψ *degree*	*Passive Force* *kips*	*kN*	*% increase*	*% increase per unit change in degree*
10	432	1922	N/A	N/A
15	474	2108	9.7%	1.9%
20	513	2282	8.2%	1.7%

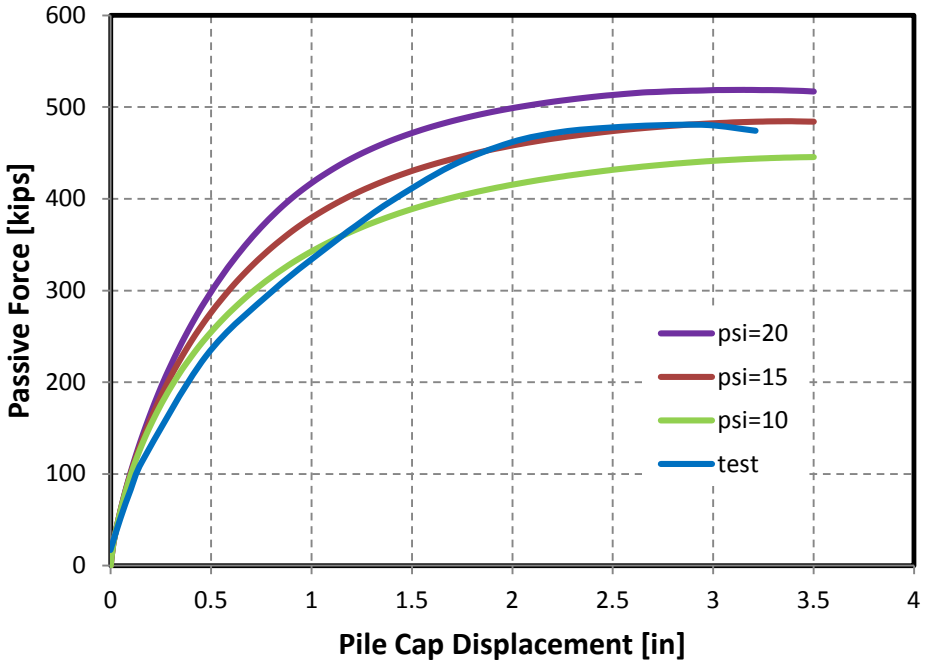

Figure 5-34: Passive Force - Deflection Curve for Different Angle of Dilatancy Sets

5.2.4 Effect of Soil Stiffness (E_{50} E_{oed} and E_{ur})

Figure 5-35 shows passive force vs. deflection curves with respect to increasing E_{50} and E_{oed} values. In those three models, E_{ur} values were held constant where E_{50} and E_{oed} are a fraction of E_{ur} value. Typically, Plaxis suggests that E_{50} is equal to E_{ur} divided by 2.0 to 3.0. As shown in Table 5-5, decreasing the divisor from 3 to 2 leads to an increase in the E_{50} value which results in a progressively stiffer passive force-deflection curve as shown in Figure 5-35 along with a small

increase in the ultimate passive force. As shown in Table 5-5, every unit decrease in the denominator of the fraction will result in about a 6.4 percent increase in passive force. When the test results were measured at 0.5 inches, each million pound per square feet increase in E_{50} and E_{oed} will result in 19% to 25% increase in the secant slope at 0.5 inches displacement.

Table 5-5: Max. Passive Force for Diferent E_{50} and E_{oed} Sets

Stiffness	*Passive Force* kips	kN	*% increase*	*% increase per unit change in denominator*	*Measured @ 0.5"* kips	kN	$E_{0.5"}$ Kips/in^2	$E_{50 \text{ or } oed}$ Lb/ft^2	*% increase of slope per unit mil. Lb/ft^2 change in $E_{50 \text{ or } oed}$@0.5"*
E50 or Eoed = 1/3 Eur	445	1979	N/A	N/A	228	1014	456	1.60E+06	N/A
E50 or Eoed = 1/2.5 Eur	459	2042	3.15%	6.29%	242	1076	484	1.92E+06	19%
E50 or Eoed = 1/2 Eur	474	2108	3.27%	6.54%	271	1205	542	2.40E+06	25%

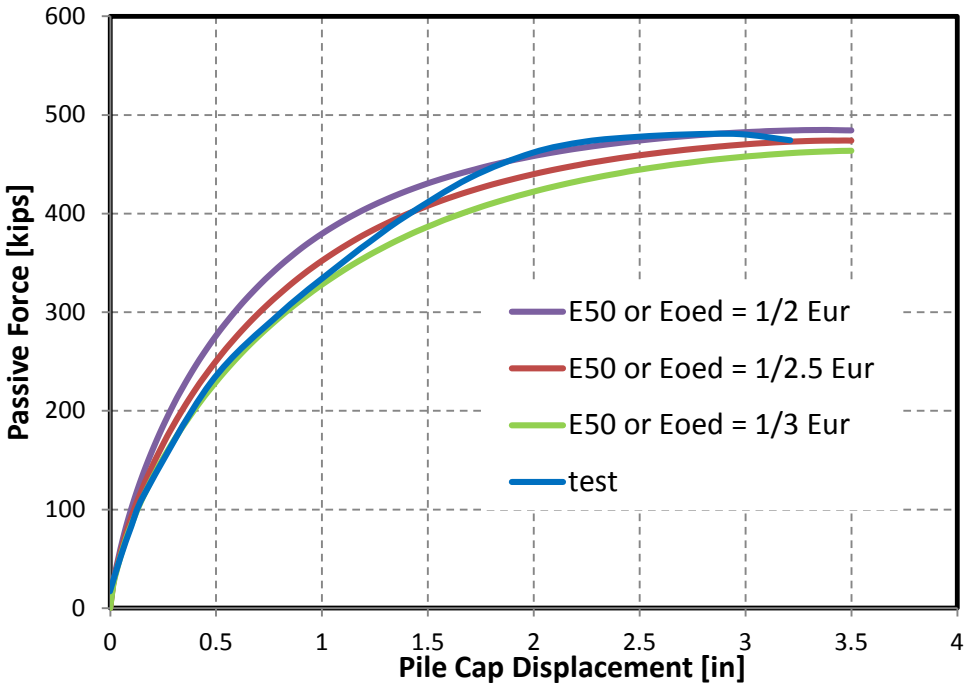

Figure 5-35: Passive Force - Deflection Curve for Different E_{50} and E_{oed} Sets

Figure 5-36, three model shave the same parameter settings except for E_{ur} values. With increasing values of E_{ur}, initial slope of the passive force versus displacement curve increases. Simultaneously, passive force values also increase. As shown in Table 5-6, each unit increase in one million pounds per square foot of E_{ur} will lead to a 4 percent increase in the ultimate passive force. When the test results were measured at 0.5 inches, each million pound per square feet increase in E_{ur} will result in 8% to 15% increase in the secant slope at 0.5 inches displacement.

Table 5-6: Max. Passive Force for Different E_{ur} Sets

Eur (Million lb/ft²)	*Passive Force*		*% increase*	*% increase per unit change*	*Measured@0.5"*		$E_{0.5"}$	*% increase of slope per unit mil. Lb/ft² change in E_{ur} @0.5"*
	kips	kN			kips	kN	Kips/in²	
3.8	421	1873	N/A	N/A	217	965	434	N/A
4.8	439	1953	4.3%	4.3%	250	1112	500	15%
5.8	455	2024	3.6%	3.6%	271	1205	542	8%

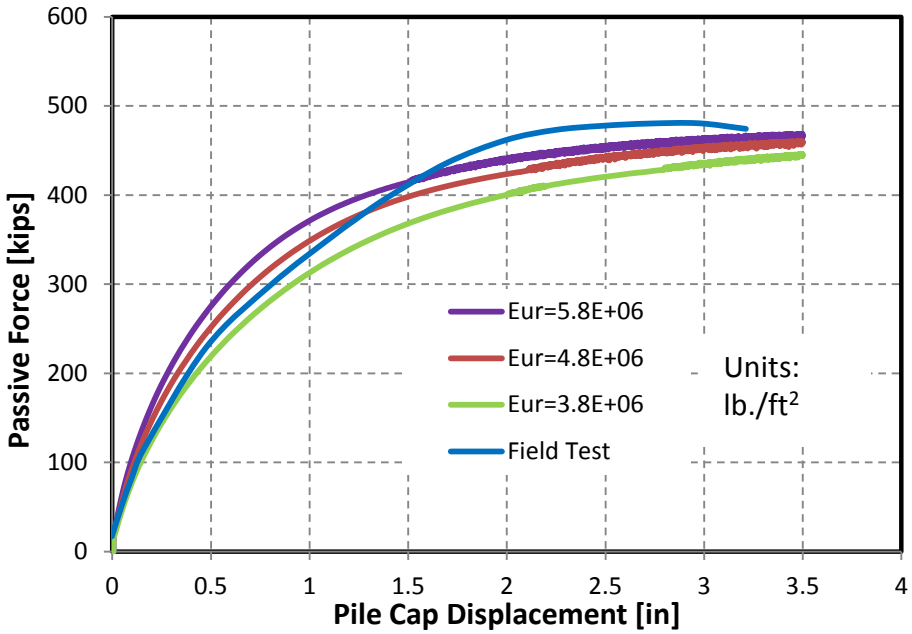

Figure 5-36: Passive Force - Deflection Curve for Different E_{ur} Values

5.2.5 Effect of Free or Fixed Directional Movement in Y-Direction

While setting up models, y directional restraint had a tremendous effect on the ultimate passive force. Figure 5-37 shows passive force increased by 5.7 percent when y directional restraint applied for 15 skew model. Furthermore, in Figure 5-38, passive force increased by 243 percent when y directional restraint was applied for 45 skew model. The reason is that with increasing skew angle, there will be less friction between the backwall and soil fill. If there is no restraint in the y direction, slipping plane effect will occur as mentioned in section 5.1.2. However, if y directional restraint is applied, it implies that additional lateral support restrain is applied to the backwall system, which is different from the site condition and will never be able to match the field test result.

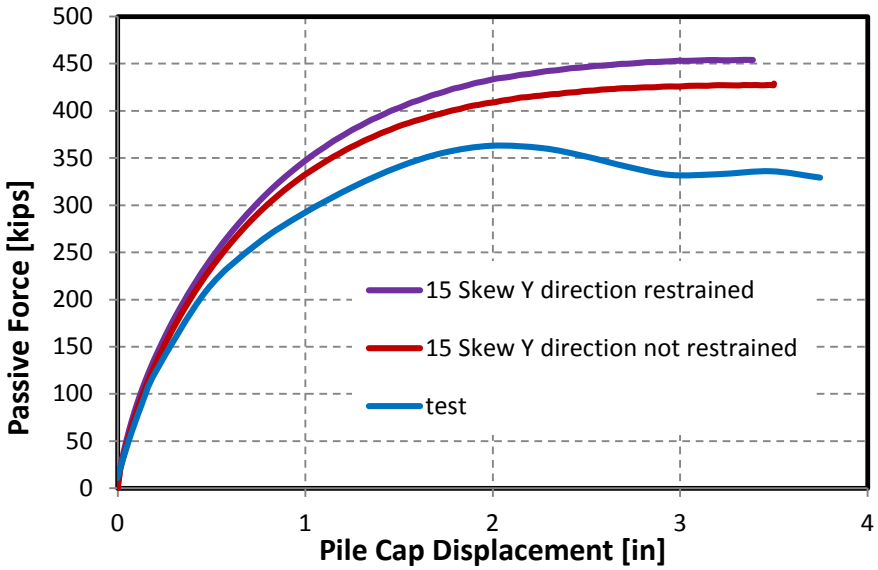

Figure 5-37: Passive Force - Deflection Curve for 15 Skew Sets to Show Y Directional Restrain Effect

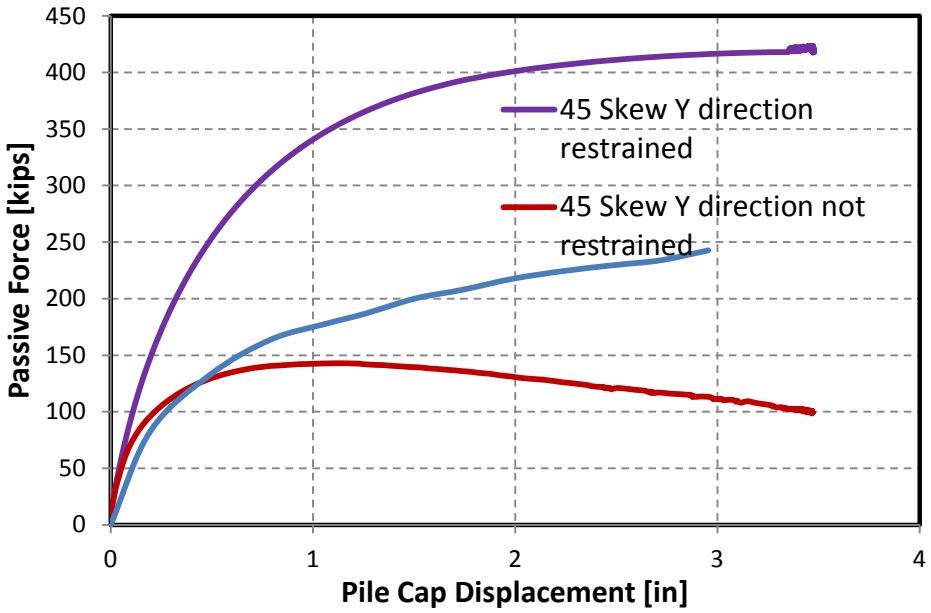

Figure 5-38: Passive Force - Deflection Curve for 45 Skew Sets to Show Y Directional Restrain Effect

5.2.6 Different Sets of Models

In addition to the basic parametric studies, a set of models of with different soil friction angles and wall friction angles were calibrated to match the measured passive force versus deflection curve from the 0° skew field test with a tolerance of 10 percent. Corresponding parameters are listed in Table 5-7. Generally, as the friction angle increased from 40° to 44°, the wall friction had to decrease from 28° to 16° as shown in Figure 5-40.

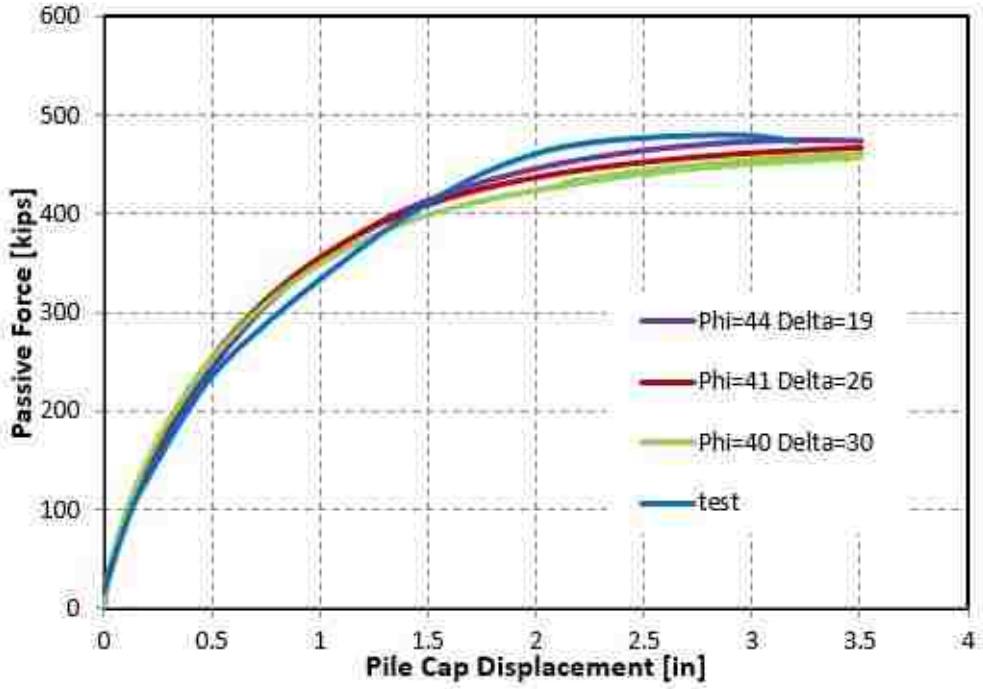

Figure 5-39: Different Set of Models Calibrated to Match Field Test Result Within 10% Error

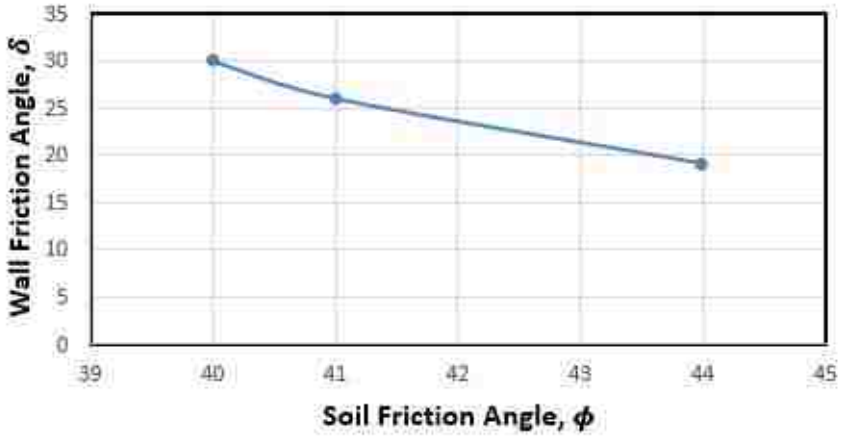

Figure 5-40: Soil Friction Angle versus Wall Friction Angle in Calibrated Sets

Table 5-7: Calibrated Model Sets with Parameters (Cont.)

Model set	*phi40*	*phi41*	*Phi44*
General Properties			
γunsat(lb/ft^3)	116.5	116.5	116.5
γsat(lb/ft^3)	120.0	120	120.0
Adavanced			
Void ratio			
Diatancy cut-off	**check**	**check**	**check**
einit	0.5450	0.545	0.5450
emin	0.4850	0.485	0.4850
emax	0.7820	0.782	0.7820
Damping			
Rayleigh α	0.000	0	0.000
Rayleigh β	0.000	0	0.000
Parameters			
Stiffness			
E50 ref (lb/ft^2)	1.920E+06	1.920E+06	1.920E+06
Eoed ref (lb/ft^2)	1.920E+06	1.920E+06	1.920E+06
Eur ref (lb/ft^2)	4.800E+06	4.900E+06	4.800E+06
power(m)	0.50	0.50	0.50
Alternatives			
Use alternatives	**uncheck**	**uncheck**	**uncheck**
Cc	3.865E-03	3.865E-03	3.865E-03
Cs	1.392E-03	1.392E-03	1.392E-03
einit	0.5450	0.5450	0.5450
Strength			
C'ref (lb/ft^2)	85.00	80.00	80.00
φ'(phi)	40.00	41.00	44.00
ψ(psi)	15.00	15.00	14.00
Adavanced			
Set to defualt values	**uncheck**	**check**	**uncheck**
Stiffness			
v'ur	0.2000	0.2000	0.2000
Pref (lb/ft^2)	2089	2089	2089
K0 nc	0.3610	0.3439	0.3340
Strength			
c' inc (lb/ft^2/ft)	0.000	0.000	0.000
z ref	0.000	0.000	0.000
Rf	0.9000	0.9000	0.9000

Model set	**phi40**	**phi41**	**Phi44**
Tension cut-off	**check**	**check**	**check**
Tensile strength (lb/ft^2)	0.000	0.000	0.000
Interface			
Strength	Manual	Manual	Manual
Rinter	0.6881	0.5611	0.3566
Delta	(delta=30)	(delta=26)	(delta=19)
δinter	0.000	0.000	0.000
Intial			
K0 settings			
K0 determination	Automatic	Automatic	Automatic
K0,x=K0,y	**check**	**check**	**check**
K0,x	0.3610	0.3439	0.3340
K0,y	0.3610	0.3439	0.3340
Overconsolidation			
OCR	1.000	1.000	1.000
POP(lb/ft^2)	0.000	0.000	0.000

6 CONCLUSIONS

This research used the finite element model Plaxis 3D to examine the response of skewed abutments to lateral loading. The typical geometry consisted of a pile cap with a backfill height of 5.5 feet (1.68 m) and with skew angles of 0°, 15°, 30° and 45° to model the behavior of full-scale tests conducted previously. The following conclusions are drawn and recommendations are made:

1. The Plaxis 3D finite element model studies conducted during this investigation confirms the concept that the ultimate passive force on a skewed bridge abutment decreases significantly as the skew angle increases.

   Therefore, a bridge structure constructed at a skew angle has a significant impact on ultimate passive force. Increasing skew angle will lead to decreasing peak passive force which will be important for seismic design and thermal expansion and contraction with integral abutments.
2. The reduction in passive force obtained with the Plaxis 3D model is generally consistent with the reduction factor proposed by Rollins and Jessee (2013) and the numerical model study conducted by Shamsabadi et al (2006)

3. The Plaxis 3D model was generally capable of producing a passive force-deflection curve that was within 10% of the measured field curves with reasonable input parameters for skew angles less than the wall friction angle.
4. When the skew angle exceeds the wall friction angle, Plaxis 3D predicts that the abutment will slide excessively and passive force will be limited to a value much less than the maximum predicted by the log-spiral approach. If this situation is encountered in practice, additional lateral restraint must be provided by abutment piles or wing walls to hold the abutment in position.
5. The Plaxis 3D model generally provided reasonable predictions of the heave zone shape and the failure plane geometry. However, it tended to overpredict the measured heave percentage and provided somewhat shorter failure plane lengths that were parabolic rather than liniear.
6. Parametric studies with Plaxis 3D indicate that the ultimate passive force is proportional to the soil friction angle (ϕ), the wall friction (δ), and the dilatancy angle (ψ) as expected. Typically, a one degree increase in ϕ increased the ultimate passive force by about 7%. A one degree increase in δ increased the ultimate passive force by 1% and a one degree increase in ψ resulted in a 1.8% increase in ultimate passive force. The sensitivity to wall friction from the finite element model is about one-third of the sensitivity observed in conventional models such as the log-spiral method.
7. Changing the divisor for E_{ur} from 3 to 2 to obtain the initial stiffness value increases in the ultimate passive for of approximately 6%.

REFERENCE

AASHTO. (2011). *LRFD Bridge Design Specifications*, 5th Ed.

Ashour, M., Norris, G., and Pilling, P. (1998). "Lateral loading of a pile in layered soil using the strain wedge model." *Journal of Geotechnical and Geoenvironmental Engineering*, 124(4), 303–315.

Borowicka, H. (1938). "Distribution of Pressure Under a Uniformly Loaded Elastic Strip Resisting on Elastic-Isotropic Ground." *Proc., 2nd Congress International Association Bridge Structures Engineering*, Vol. 8(3).

Brinkgreve, R. B. J. (2006). *Plaxis 3D Tunnel, Tutorial Manual, Version 2*.

Burke Jr., M. P. (1994). "Semi-Integral Bridges: Movements and Forces." 1-7 p.

Caltrans. (2006). *Standard Specifications,* Sacramento, California.

Caltrans. (2010). *Caltrans Seismic Design Criteria Version 1.6*, California Department of Transportation, Sacramento, California

Christensen, D. S. (2006). "Full Scale Static Lateral Load Test of a 9 Pile Group in Sand." Master of Science, Brigham Young University, Provo, Utah.

Coulomb, C. A. (1776). "Essai sur une application des règles de maximis & minimis à quelques problèmes de statique, relatifs à l'architecture." (microform, Microopaque), De l'Imprimerie Royale, Paris.

Cummins, C. R. (2009). "Behavior of a Full-Scale Pile Cap with Loosely and Densely Compacted CLean Sand Backfill Under Cyclic and Dynamic Loadings." *M.S. Thesis*, Department of Civil and Environmental Engineering, Brigham Young University, Provo, UT.

Duncan, J. M., and Chang, C. Y. (1970). "Nonlinear analysis of stress and strain in soil." *Journal of Soil Mechanics and Foundations Division*, ASCE 96, 1629-1653.

Elnashai, A. S., Gencturk, B., Kwon, O., Al-Qadi, I. L., Hashash, Y., Roesler, J. R., Kim, S. J., Jeong, S., Dukes, J., and Valdivia, A. (2010). "The Maule (Chile) Earthquake of February 27, 2010: Consequence Assessment and Case Studies." Department of Civil and Environmental Engineering, University of Illinois at Urbana-Champaign, 190.

Franke, B. (2013). "Passive Force on Skewed Abutments with Mechanically Stabilized Earth (MSE) Wingwalls Based on Large-Scalte Tests." *M.S. Thesis*, Department of Civil and Environmental Engineering, Brigham Young University, Provo, UT.

Gerber, T. M., Rollins, K. M., Cummins, C. R., and Pruett, J. M. (2010). "Dynamic Passive Pressure on Abutments and Pile Caps." *Report No. UT-10.18*, Research Division, Utah Department of Transportation, 223 p.

Johnson, S. R. (2003). "Static Lateral Load Testing of a Full-Scale Pile Group Spaced at 5.65 Pile Diameters." *M.S. Thesis*, Department of Civil and Environmental Engineering, Brigham Young University, Provo, UT.

Lemnitzer, A., Ahlberg, E., Nigbor, R., Shamsabadi, A., Wallace, J., and Stewart, J. (2009). "Lateral Performance of Full-Scale Bridge Abutment Wall with Granular Backfill." *Journal of Geotechnical and Geoenvironmental Engineering*, 135(4), 506-514.

Mokwa, R. L., and Duncan, J. M. (2001). "Experimental Evaluation of Lateral-Load Resistance of Pile Caps." *Journal of Geotechnical and Geoenvironmental Engineering, ASCE*, 127(2), 185-192.

Norris, G. M. (1977). "The drained shear strength of uniform quartz sand as related to particle size and natural variation in particle shape and surface roughness." Ph.D. thesis, University of California, Berkeley, California.

Potyondy, J. G. (1961). "Skin Friction Between Various Soils and Construction Materials." *Geotechnique, London*, 11(1), 339-353.

Rankine, W. J. M. (1857). "On the Stability of Loose Earth." *Philosophical Transactions of the Royal Society of London*, 147, 9-27.

Reference Manual: *PLAXIS 3D-2015; Edited by R.B.J. Brinkgreve; Delft University of Technology & PLAXIS b.v.; The Netherlands*

Rollins, K. M., and Cole, R. T. (2006). "Cyclic Lateral Load Behavior of a Pile Cap and Backfill." *Journal of Geotechnical and Geoenvironmental Engineering, ASCE*, 132(9), 1143-1153.

Rollins, K. M., Gerber, T. M., and Heiner, L. (2010). "Passive Force-Deflection Behavior for Abutments with MSE Confined Approach Fills." *Report No. UT-10.15*, Utah Department of Transportation, Salt Lake City, UT, 83 p.

Rollins, K. M., and Jessee, S. J. (2013). "Passive Force-Deflection Curves for Skewed Abutments." *Journal of Bridge Engineering*, *ASCE*, Vol. 18, No. 10, (Oct) p. 1086-1094

Rollins, K.M., King, R., Snyder, J.E., and Johnson, S.R. (2005b). "Full-scale lateral load tests of pile groups and drilled shafts in clay." *Procs. Intl. Conf. on Soil-Structure Interaction, Calculation Methods and Engineering Practice*, Vol. 1, Ulitsky, V.M., Ed., ASV Publishers, Moscow: 287-292.

Rollins, K. M., Nasr, M., and Gerber, T. M. (2010). "Numerical Analysis of Dense Narrow Backfills for Increased Passive Resistance." *Report No. UT-10.19*, Research Division, Utah Department of Transportation, 192 p.

Rollins, K.M., Snyder, J.L., and Broderick, R.D. (2005a). "Static and dynamic lateral response of a 15 pile group." *Procs. 16th Intl. Conf. on Soil Mechanics and Geotechnical Engineering*, Vol. 4, Millpress, Rotterdam, Netherlands: 2035-2040.

Rollins, K. M., and Marsh, A. (2013). "Evaluation of Passive Force on Skewed Bridge Abutments with Large-Scale Tests." Master of Science, Brigham Young University, Provo, Utah.

Rollins, K. M., and Smith, K. (2014). " Passive Force on Skewed Bridge Abutments with Reinforced Concrete Wingwalls - Based on Large-Scale Tests." Master of Science, Brigham Young University, Provo, Utah.

Rollins, K. M., and Sparks, A. E. (2002). "Lateral Load Capacity of a Full-Scale Fixed-Head Pile Group." *Journal of Geotechnical and Geoenvironmental Engineering, ASCE*, 128(9), 711-723.

Schanz, T., Vermeer, P.A., Bonnier, P.G., (1999). The Hardening-Soil Model: Formulation and verification. In: R.B.J. Brinkgreve Beyond 2000 in Computational Geotechnics. Balkema, Rotterdam: 281-290.

Shamsabadi, A., Ashour, M., and Norris, G. (2005). "Bridge Abutment Nonlinear Force-Displacement-Capacity Prediction for Seismic Design." *Journal of Geotechnical and Geoenvironmental Engineering, ASCE*, 131(2), 151-161.

Shamsabadi, A., Kapuskar, M., and Zand, A. (2006 Published). "Three-Dimensional Nonlinear Finite-Element Soil-Abutment Structure Interaction Model for Skewed Bridges." *Paper presented at 5th National Seismic Conference On Bridges and Highways*, 1-10.

Shamsabadi, A., Rollins, K. M., and Kapuskar, M. (2007). "Nonlinear soil-abutment-bridge structure interaction for seismic performance-based design." *Journal of Geotechnical and Geoenvironmental Engineering*, ASCE Vol. 133(6), 707-720.

Strassburg, A. N. (2010). "Influence of Relative Compaction on Passive Resistance of Abutments with Mechanically Stabilized Earth (MSE) Wingwalls." Master of Science, Brigham Young University, Provo, Utah.

Steinberg, E., Sargand, S., and Bettinger, C. (2010). "Forces in Wingwalls from Thermal Expansion of Skewed Semi-Integral Bridges." Ohio University Department of Civil Engineering, Athens, Ohio.

Taylor, A. J. (2006). "Full-Scale-Lateral-Load Test of a 1.2 m Diameter Drilled Shaft in Sand." *M.S. Thesis*, Department of Civil and Environmental Engineering, Brigham Young University, Provo, Utah.

Terzaghi, K. (1943). *Theoretical Soil Mechanics*, J. Wiley & Sons, New York.

Terzaghi, K., Peck, R., and Mesri, G. (1996). *Soil mechanics in engineering practice, 3rd edition*, John Wiley and Sons, Inc. New York, NY.

Wilson, P., and Elgamal, A. (2010). "Large-Scale Passive Earth Pressure Load-Displacement Tests and Numerical Simulation." *Journal of Geotechnical and Geoenvironmental Engineering*, ASCE, 136(12), 1634-1643.